ASSESSING THE POTENTIAL OF ASTER NIGHT-TIME SURFACE TEMPERATURE AND DERIVED APPARENT THERMAL INERTIA FOR GEOLOGICAL MAPPING WITHIN HAIB, NAMIBIA

KALEB GEBREYES LEMMA

[May 2019]

SUPERVISORS:
Dr. R.D. Hewson (Rob)
Prof. Dr. F.D. Van Der Meer (Freek)

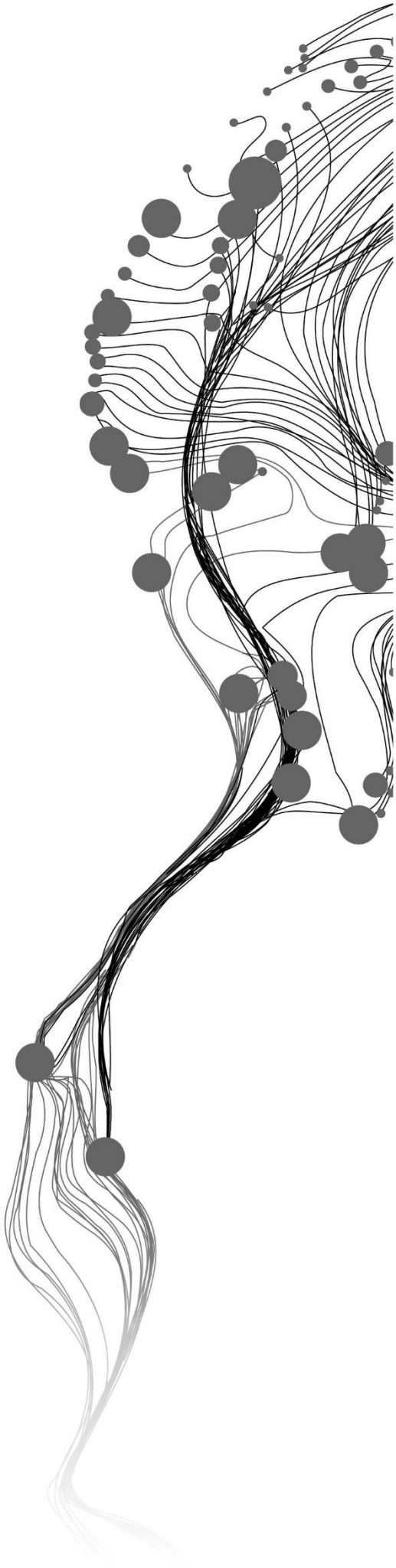

ASSESSING THE POTENTIAL OF ASTER NIGHT-TIME SURFACE TEMPERATURE AND DERIVED APPARENT THERMAL INERTIA FOR GEOLOGICAL MAPPING WITHIN HAIB, NAMIBIA

KALEB GEBREYES LEMMA
Enschede, The Netherlands, May 2019

Thesis submitted to the Faculty of Geo-Information Science and Earth Observation of the University of Twente in partial fulfilment of the requirements for the degree of Master of Science in Geo-information Science and Earth Observation.
Specialization: Applied Earth Sciences - Geological Remote Sensing

SUPERVISORS:
Dr. R.D. Hewson (Rob)
Prof. Dr. F.D. Van Der Meer (Freek)

THESIS ASSESSMENT BOARD:
Prof. Dr. M. van der Meijde (Chair)
Prof. Dr. Kim Hein (External Examiner, University of the Witwatersrand, South Africa)

ABSTRACT

This research was aimed to evaluate the ***potential*** of ASTER night-time surface temperature (NST) and the derived apparent thermal inertia (ATI) to discriminate outcrops from unconsolidated cover and interpret them quantitatively; and also the thermal sensing capability to ***identify*** geological structures in comparison with 1st vertical derivative (1VD) magnetics, which has limited published work. Analyzing the effect of green vegetation on discriminating outcrops from unconsolidated cover was also the aim of this research. Evaluating the potential of ASTER NST and ATI is relevant to determine their significance for mineral exploration activities such as sample site selection for geochemical analysis and structural detection. The ASTER NST imageries used in this study were corrected for the effect of topography using a published software. The discrimination of outcrops from unconsolidated cover has been ***initially tested*** using ASTER NST & ATI and other dataset products to understand the spatial ***relationship between*** the thermal and other dataset products. This procedure was followed by developing ***ranging methods*** to select ***ranges of values*** from the slope map, ASTER NST, and ATI products respectively to represent the outcrops and unconsolidated cover. These selected ranges of values (thresholds) were attempted to spatially ***discriminate*** the outcrops from unconsolidated cover using ASTER NST and ATI products for visual observation using an assumption of topographic controls on the geomorphology. Hence, ***overlay analysis*** was conducted between the ranges of values and the published lithological unit vectors in ArcGIS to ***quantitatively evaluate*** the potential of ASTER NST and ATI products to discriminate outcrops from unconsolidated cover. The results of the overlay analyses showed that the quality of the ranging methods and the selected ranges of values used for the discrimination were good. Regarding the geological structures, 57.41 km and 30.01 km were identified from 1VD and ATI products, respectively. However, when the results of the two methods were integrated using ArcGIS, a total of 74.41km could be identified. So that, 77.14% and 40.32% could be identified from the 1VD and ATI methods respectively; and 17.49% of the lineaments were identified in common from both methods. This result showed the ***lower*** potential of ATI to detect lineaments in comparison. However, it could be useful as a ***supplementary*** method to that of 1VD. So, ***integrating*** the results of the two methods has a benefit to delineate potentially more lineaments than using each technique individually. In this research, the effect of green vegetation on discriminating outcrops from unconsolidated cover has also been analyzed. For that purpose, statistical information was generated from ASTER NST and NDVI products of different seasons targeting regions of interest on outcrops and unconsolidated cover. So that, analyses were made using correlation matrix and boxplots, and the result showed ***reduction and regulation*** of the surface temperature due to the effect of green vegetation. This effect could be observed from the moderate correlation (-0.366) between the ASTER NST and NDVI of the year 2018 imageries and the less correlation (-0.295) in the year of 2015 imageries. As a result, discriminating outcrops from unconsolidated cover in areas with increased vegetation cover could be more difficult.

Keywords: ASTER NST, ATI, slope angle, ranges, discriminate, outcrops, unconsolidated cover, overlay, quantitative interpretation, lineament, integration, topographic effect, STcorr, vegetation, NDVI

ACKNOWLEDGMENTS

First, I would like to give the Almighty God all the glory for every blessings and grace.

Let me take this opportunity to extend my sincere gratitude to my supervisors: Dr. R.D. Hewson (Rob) and Prof. Dr. F.D. Van Der Meer (Freek) for their unreserved support, guidance, and commitment from the beginning to its end. This study could not be materialized without their significant inputs, scientific critics, and explanations without the limit of time and distance.

I am indebted to the Netherlands Fellowship Programme (NFP) and International Institute for Geo-information Science and Earth Observation (ITC) for providing me the chance to study at ITC. Am thankful to the Geological Survey of Namibia to provide us airborne magnetics and radiometrics data and the geological map; DigitalGlobe Foundation Inc. for providing WV-3 data; and NASA for providing ASTER data.

My deepest thanks go to Mr. Bart Krol, Course Director of AES, for his kind effort he did for me to get an extension to compensate the time missed due to sickness, and for his continuous advice and encouragement. I wouldn't leave the student affairs (Marie Chantal and Theresa) without my appreciation who facilitate medical treatment.

I am grateful to Prof. Dr. M. van der Meijde for his constructive comments and advice during the proposal writing. My appreciation extended to Dr. Chris Hecker, Dr. Thomas Groen, and Dr. Wim Timmermans, for sharing their ideas related to ATI.

I would like to thank my family: my mother, sisters, brothers, and friends for all kinds of moral and spiritual support.

My special thanks go to C.J (Jerrisha), the other part of myself, for her tremendous encouragement and moral. I can only say I love you and live longer.

TABLE OF CONTENTS

LIST OF FIGURES

LIST OF TABLES

1. INTRODUCTION

1.1. Research Background

The demand for various minerals is globally increasing due to their significance for industrialization and widespread applications. Reliable geological information has a major role in identifying an area for optimal mineral exploration, and access to the geoscience information in a well-organized manner can attract potential investors to participate in the mining industry which roles for the economic growth of countries. Geological information can be acquired using different remote sensors. One of them is the Advanced Spaceborne Thermal Emission and Reflection Radiometer (ASTER) which has VNIR, SWIR, and TIR bands with an advantage of acquiring imageries during the day and night-time. The day-time reflectance imageries of VNIR and SWIR could be influenced by the sun's position and surface topography, whereas the nighttime TIR imageries are not affected by illumination and so is useful for the detection of thermally anomalous bodies without the effect of solar radiation (Kuenzer & Dech, 2013). Assessing the ***ability*** of ASTER thermal imagery for mapping changes in the physical properties related to geology is useful for utilizing the data for discriminating the outcrops from unconsolidated cover and detecting geological structures. The ***unconsolidated cover*** units of the study area were defined as the quaternary alluvial and colluvial deposits, and the Permian sediments caused from the weathered sedimentary rocks including Karoo sedimentary unit. The competent solid rocks of the study area were also defined as ***outcrops***. The study focused on the assessment of the TIR bands particularly the night-time surface temperature (NST) of ASTER product and the derived apparent thermal inertia (ATI) for discriminating outcrops from unconsolidated cover; and evaluating the detection of structures. Surface temperature can be estimated from the TIR bands of ASTER with an accuracy of +-1.5K ("ASTER Surface Kinetic Temperature Product," n.d.) and used for ATI calculation. ATI is a volumetric physical property and a proxy of the actual thermal inertia and can be calculated using Albedo and the temperature difference between the day and night-time (Majumdar, 2003; Nasipuri et al., 2005; Mitra & Majumdar, 2010; Pratt & Ellyett, 1979; Beeson et al., 2011; Price, 1977; Kahle, 1987; Price et al., 2016). The surface temperature difference between the day and night-time is mainly dependent on the thermal physical characteristics (Ramakrishnan et al., 2013), and which is also distinct for different earth materials such as rocks, soil, and water as shown in figure 4. So that, geological materials with lower diurnal temperature difference can have higher thermal inertia whereas those with higher diurnal temperature difference can have lower thermal inertia (Kuenzer & Dech, 2013; Lillesand et al., 2015). Separating the outcrops from unconsolidated cover using ASTER thermal imageries can be useful for selecting target areas from the in situ solid rocks and overbank sediments for geochemical sampling in mineral exploration field activities and may also assist the relating of geochemical soil anomalies to either shallow outcropping or transported cover materials. For this reason, the governmental organizations and private companies who are involved in geological mapping and mineral exploration operations can be potential users of ASTER thermal imageries.

Several research studies have been conducted using various sensor's VNIR and SWIR spectral regions for geological applications; however, the TIR bands have been used relatively less for geological applications (Zadeh & Tangestani, 2013). However, the studies show the relevance of thermal infrared imageries acquired by various types of sensors for geological applications. For example, the advantage of thermal infrared imageries for differentiating various geological materials have been demonstrated using Nimbus satellite data (Watson, 1975). Kahle (1987) utilized the thermal imagery acquired by the Thermal Infrared Multispectral Scanner (TIMS) that its five bands out of the six are similar in wavelength and spectral

resolution with ASTER. Kahle (1987) has separated the temperature from emissivity using TIMS imageries and the separation method developed by Kahle et al. (1980). Hence, the day and nighttime surface temperature difference were calculated and used to derive the apparent thermal inertia using the formula developed by Price (1977) without correcting the topographic and atmospheric effects. The result was found useful to differentiate some of the bedrocks from the transported alluviums based on the difference in their physical properties (Kahle, 1987). In this study, the topographic effects (altitude, slope, and aspect) have been corrected using ***STcorr2015*** program which is an IDL based code used for the topographic correction using image-based polynomial regression analysis (Ulusoy et al., 2012). Mapping the geology by calculating ATI using the National Oceanic and Atmospheric Administration-Advanced Very High Resolution Radiometer (NOAA-AVHRR) satellite thermal data was conducted elsewhere. So, the result was found useful to map the gross lithology and lineaments; however, due to the poor spectral and spatial resolutions the result was not good, and the higher resolution ASTER TIR imagery was recommended (Mitra & Majumdar, 2010). Hewson et al. (2017) have tested the ASTER night-time surface temperature, and ATI, and the result appeared useful to detect the outcrops and cover; however, the lack of pair of day and night-time thermal imageries was the handicap of ASTER to determine its potential. In addition to that, detection of sub-surface alluvial features such as palaeochannels using ATI and airborne magnetic data has been attempted elsewhere. However, as the area covered with ASTER was limited to determine the result, and further study over a wider area was recommended. In addition to that, a study into the capability of ASTER thermal products for detecting geological structures, and the benefit of its integration with airborne magnetics was recommended as it would be useful (Hewson et al,. 2017). Different geological materials could have different density, thermal conductivity, and specific heat; however, igneous rocks have nearly similar thermal inertia values (see table 4) than sedimentary rocks and discriminating igneous rocks is a bit difficult (Gupta, 2003). The range of density values of some rock types that are equivalent to the Haib rocks show that igneous rocks have relatively similar density values to each other, and that affects discriminating those rocks (see appendix 14). The denser geologic materials can have higher thermal inertia than the lighter unconsolidated cover; as a result, the unconsolidated materials heat up and cool down quickly (Watson, 1975). This variation in a thermal physical property between different geologic materials helps to discriminate them using thermal products (Ramakrishnan et al., 2013). The negative correlation between surface temperature and vegetation has been established using the normalized difference vegetation index (NDVI) which ranges from -1 to +1 (Fatemi & Narangifard, 2019; Mathew., 2018; Song et al., 2018). However, further studies of the effect of vegetation on discriminating outcrops from unconsolidated cover would be useful.

1.2. Problem statement

Many of the researchers have focused on the imageries with VNIR-SWIR wavelength region of the electromagnetic spectrum acquired from various sensors for surface geological mapping applications, but the surface temperature imageries have been used less in comparison even though it is useful (Zadeh & Tangestani, 2013). The role of geochemical mapping to identify potentially anomalous mineralization zone was established several years ago (Zuo et al., 2019). For that purpose, software generated overbank sediment or transported regolith sample site selection was commonly applied. However, in case of lack of access or inconvenient topography of the terrain, selecting the sampling sites manually other than the automatic approach could be necessary, and information of the surficial materials and competent rock exposures for the sampling is required (Lech et al., 2007). Hence, a method to discriminate the outcrops from unconsolidated cover could be an option to select sites for geochemical sampling as it has not been published widely. Evaluating the potential of ASTER NST and ATI to discriminate outcrops from unconsolidated cover with qualitative interpretation was attempted somewhere else by Hewson et al. (2017) and the result appeared useful, but a pair of data was limited to confirm the potential. The ***quantitative interpretation*** that was attempted in this study to evaluate the potential of ASTER NST

and ATI quantitatively for discriminating outcrops from unconsolidated cover involved calculating the area of intersection between the lithological units (Blignault 1972) and the ranges of values in ArcMap using Overlay Analysis Tool.

The total land of Namibia had been surveyed by airborne magnetics, and a general overview of the magnetic anomalies and linear features of various geological units have been mapped (Eberle et al., 1995). The geological map of Haib, which was produced in 1972 with 1:100,000 scale, could also show the occurrence of sediments and solid rocks; and geological structures which indicated how the area was tectonically affected and that was revealed by the surface linear structures. So, this study area could be relevant for evaluating the capability of ASTER thermal imageries to discriminate outcrops from cover and detecting structures (e.g., lineaments, sand dunes & palaeochannels). ASTER data has been well applied for lithological and mineralogical mapping; however, its application for structural mapping has not been well studied (Papadaki et al., 2011). Comparing the thermal products ASTER with airborne magnetics to determine its capability to detect lineaments and the benefit of its integration would be relevant (Hewson et al., 2017) as it has not been widely done. The negative relation (cooling effect) of green vegetations on the day-time ASTER surface temperature and the positive relation with ATI have been observed with a limited pair of day and night-time imageries; however, further work was recommended to analyze the effect of green vegetation on the thermal products (Hewson et al., 2017).

1.3. General objective

The major objective of this research is to assess the potential of ASTER night-time surface temperature (ASTER NST) and derived apparent thermal inertia (ATI) for discriminating outcrops from unconsolidated cover and interpreting them quantitatively; and the thermal capability of structural mapping within the Haib prospect, Namibia.

1.4. Specific objectives

1) To develop a method to discriminate outcrops from unconsolidated cover using ASTER NST, ATI & DEM, and conduct quantitative interpretation to evaluate the potential of ASTER NST & ATI for discrimination.
2) To evaluate the capability of ASTER NST and ATI products for mapping geological structures (e.g., lineaments & palaeochannels) by comparing with airborne magnetics data within the study area.
3) To analyze the effect of green vegetation on discriminating outcrops from unconsolidated cover by using NDVI and ASTER NST imageries acquired from different seasons within the study area.

1.5. Research questions

1) Can the ASTER NST and ATI products be used to discriminate outcrops from unconsolidated cover within the study area potentially? And is it possible to determine the potential of ASTER NST & ATI quantitatively by developing a method?
2) How comparable is the capability of ASTER NST and ATI to detect structures (e.g. lineaments & palaeochannels) as compared to airborne magnetics? And what is the benefit of integrating the results of ASTER NST/ATI with airborne magnetics related to delineating lineaments?
3) What effect does the green vegetation cover can have on the ability of ASTER NST imageries, acquired from different seasons, to discriminate outcrops from unconsolidated cover?

1.6. Hypothesis

1) Topography and geology are related to each other.

2) The difference in thermal physical properties between the outcrops and unconsolidated cover can be used to discriminate them using ASTER NST and ATI products.
3) ASTER thermal imagery can discriminate below the surface, including potentially subsurface alluvial structures (e.g., palaeochannels) and geological structures.
4) Vegetation can have an observed effect on ASTER NST to discriminate the outcrops from unconsolidated cover, and there might be a variation of the effect with seasons.

2. STUDY AREA

2.1. Geographic Location

The research area was located in the extreme southern part of Namibia, Karas region, within the locality called Haib, which is bordered with the Orange River and the Northern part of South Africa. Geographically the study area is bounded by 28^0 33' 50"S/ 17^0 50' 0.00"E, 28^0 33' 50"S/ 18^0 0.00' 0.00"E, 28^0 45' 42"S/ 18^0 0.00' 0.00"E, 28^0 45' 42"S/ 17^0 45' 18"E and 28^0 38' 20"S/ 17^0 45' 18"E. The total areal coverage is about 413 km^2.

Haib is characterized by rugged topography and arid climatic area. The temperature during the summer season reaches 40^0C, which is the hottest period while in winter it becomes very cold in contrary. The Haib climate is unusual and is located within both summer and winter rainfall areas. The rainfall in the winter season is mostly very light with occasional hard fall whereas in the summer season it is very high in its intensity but falls for a shorter period. All of the Rivers within Haib prospect area are ephemeral, and generally, the average annual rainfall is about 25-50mm (Walker, 2018). The vegetation is xerophytic with very sparse semi-desert bushes/shrubs and grasses with few short trees along the river courses (Walker, 2018).

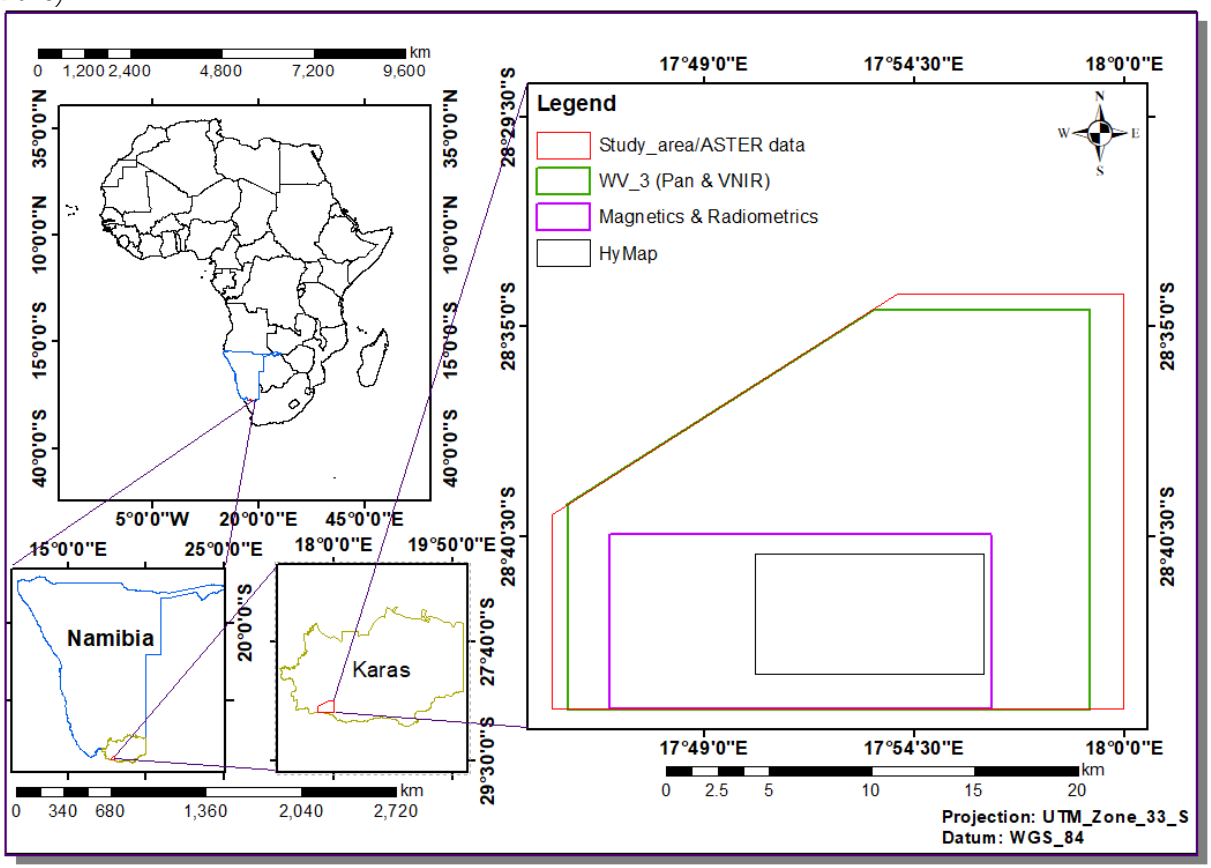

Figure 1 Location map of the study area with the data coverage used in this research.

2.2. Geology of Haib

The study area is located within the Richtersveld sub-province which is part of the Namaqua-Natal Province with NW-SE trending Proterozoic metamorphic belt that extends beneath the phanerozoic Karoo Supergroup (Cornell et al., 2006; Thomas et al., 1994). According to Macey et al. (2017), the

Proterozoic rocks of this province undergone regional metamorphism during the Namaqua Orogeny between (~1.2 – 1.0 Ga). The Namaqua-Natal province is separated into the Namaqua sector and Natal sector by Karoo sediments (Cornell et al., 2006; Eglington & Armstrong, 2003; Thomas et al., 1994). The outcrops of Karoo unit, which consists of mudstones, siltstones, and sandstones are exposed near to the Northern and North-western part of the study area (Walker, 2018). However, this unit occurred within the study area as surficial material and illustrated on the published map (Blignault 1972) as Karoo sediments. So that, in this study, this unit is assumed as the cause of the unconsolidated surficial materials in addition to the weathered intrusive rocks. The Richtersveld sub-province is further subdivided into Orange River Group (ORG) and Vioolsdrift Intrusive Suite (VIS). Vioolsdrift Intrusive Suite (VIS) is mainly comprised of basic to ultrabasic complexes including diorite, tonalite, granodiorite, adamellite, quartz-feldspar porphyry and leucogranite intrusive rocks intruded during the two main intrusive activities (Reid, 1977). On the other hand, the Orange River Group (ORG) is the oldest rock and composed of volcanic rocks, deformed amphibolites, meta-sediments and reworked volcaniclastic sediments that have undergone displacement as a result of deformation in the shear zones (Swart, 2008; Walker, 2018). The ORG subdivided into four main units: (1) the De Hoop Subgroup; (2) the Haib Subgroup; (3) the Hom Subgroup; and (4) the Rosyntjieberg Formation. Amongst these subgroups, the Haib Subgroup is divided into Nous and Tsams Formations based on their compositional variation. Hence, the Nous Formation is made up of mafic rocks such as basaltic-andesite and andesite lavas, minor leucocratic intercalations and minor volcanic breccia and tuffs, while the Tsams Formation is dominated by felsic rocks such as upper feldspar porphyry, lower feldspar porphyry, dacite and rhyolite with minor andesite (Reid, 1977). Generally, most of the rocks around Haib area are competent except the karoo weathered and porous sedimentary unit; and the study area is also characterized by well jointed flat to steeply dipping set of joints which are parallelly oriented with the dominant N60^{0}W trending regional structures (Walker, 2018).

2.3. Landform of Haib

The study area is mainly undulated in topography (Connelly, Walker, & Richards, 2018) but the northern sub area is flat to gentle slope as it falls within the Orange-Fish River Basin. This Basin is characterized by flat landform and formed by the Nama or Karoo unit (Swart, 2008). Orange-Fish River Basin is classified into four main geomorphological zones based on the geology that underlying the Basin, the general landscape and slope of the terrain. These are Nama-Karoo Plains, Karasburg Mountains, Gamchab Basin, and the Orange River Canyon. The study area is fully covered under the Gamchab Basin which is characterized by wide, large and moderately sloping gorges and drainages directed into the Orange River (Goudie et al., 2015). The Gamchab Basin is accumulated with mainly of the Karoo Group sediments and with some intrusions of dolerites. Linearly oriented sand dunes that were formed by the aeolian activity is commonly formed in the arid climatic regions of Namibia including the study area with northwest to southeast regional trend (Goudie et al., 2015). Paleochannels, which are ancient watercourses covered with the recent clay and gravel materials have also been revealed by the mining activity within the southern part of Namibia (Kirkpatrick et al., 2018). The exposition of unconsolidated transported cover and competent solid rocks, tectonic related lineaments and shear zones, aeolian sands and alluvial features within Haib makes the area relevant to assess ASTER thermal products.

2.4. Prospectivity of Haib

The Orange River Group (ORG), which is the oldest rock and intruded by the highly deformed and younger Vioolsdrif Intrusive Suite (VIS), is known for copper deposits (Swart, 2008). One of the known and oldest deposit of ORG is the Haib porphyry copper deposit, which is associated with magmatic bodies and characterized by high tonnage with lower grade copper associated with other precious metals such as silver and gold (Swart, 2008). Haib is known for a copper mineral deposit since 1990s and became a prospective mineral zone for exploration; however, the mining activity that had been taken place within

Haib was not significant except some open pit mining operations (Walker, 2018). Various companies have been exploring for copper and associated base metals on the area for several years, and economic deposit is discovered (Connelly et al., 2018).

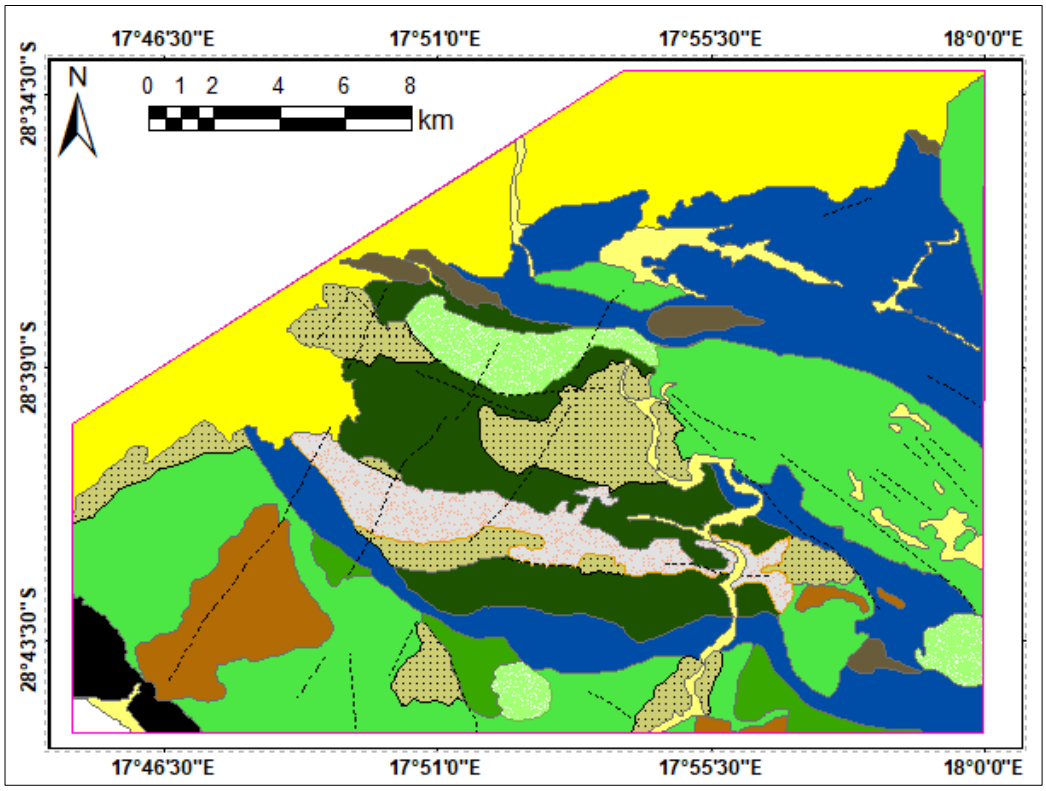

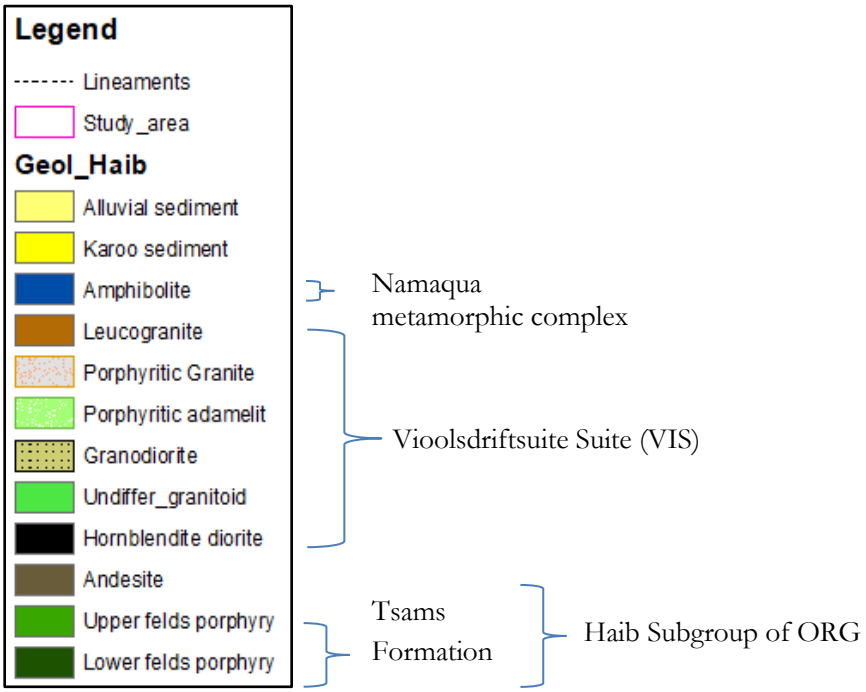

Figure 2 Geological map of Haib (after Blignault, 1972)

3. DATASETS

3.1. Datasets used for the research

This research has involved eight datasets to address the research objectives. The ASTER level 2 radiometrically and geometrically corrected imageries were downloaded from the NASA website (https://search.earthdata.nasa.gov/search) and a 30 m ground resolution Shuttle Radar Topography Mission (SRTM) Digital Elevation Model (DEM) from the USGS website (https://earthexplorer.usgs.gov). The airborne geophysics datasets were provided by the Geological Survey of Namibia. The airborne magnetics and radiometrics datasets were already pre-processed and gridded into 50m ground resolution. The HyMap sensor has 128 channels from 0.55 – 2.5 µm, and is utilized for geological applications mainly the spectral region between 2.0 – 2.5 µm (Cocks et al., 1998). The multispectral WV-3 sensor has Panchromatic (450-800nm), VNIR (400-1040nm) and SWIR (1195 – 2365 nm) bands ("WorldView-3 Satellite Sensor," n.d.). The wavelength ranges and resolutions of HyMap and WV-3 that were available and used for this research are mentioned in table 2. The rainfall data were downloaded from the South African station in Vioolsdrif, which is close to the study area by 15km, using the website: https://data.nodc.noaa.gov/cgi-bin/iso?id=gov.noaa.ncdc:C00516. This rainfall data were used to estimate the rainy season that favors the growth of green vegetation within the study area. So that, the ASTER NST acquired in 2018 where vegetation was moderate compared to the 2015 ASTER NST as estimated from the rainfall data (see appendix 12).

Table 1 ASTER Level 2 surface kinetic temperature, reflectance and emissivity data acquisition dates

	ASTER Level-2 surface kinetic temperature Daytime	**ASTER Level-2 surface kinetic temperature Night-time**	**ASTER Level-2 surface reflectance**	**ASTER Level-2 surface emissivity**	**Remark**
Acquisition date	12-May-18	15-May-18	12-May-18	-	Reflectance is only VNIR
	21-Sept-15	19-July-15	04-Oct-15	-	Reflectance is only VNIR
			09-Mar-03	09-Mar-03	Reflectance is VNIR & SWIR
Resolution	90 m	90 m	15/30 m	90 m	

Table 2 Other datasets used for the research

No.	Data	Resolution/scale	Remark
1	SRTM DEM	30m	
2	HyMap	5m	• 2.0836-2.4225 μm (Band 102-band 122) • 54km² of the study area *21 bands
3	WV-3 (Panchromatic)	0.3m	• 450-800nm
4	WV-3 (VNIR)	1.2m	• 400-1040nm (MUL1-MUL8)
5	Airborne magnetic	50m	143 km² of the study area, it was acquired in 1994.
6	Airborne radiometric	50m	143 km² of the study area
7	Geological map	1:100,000	Produced by Blignault (1972)

3.2. Softwares used for the research

For this research, six software have been utilized for processing the datasets and presenting the results of the study as shown below in table 3.

Table 3 List of software used for the study

No.	Software	Description
1	ENVI	Used for processing ASTER, WV_3 (Pan & VNIR), HyMap and DEM datasets
2	ERDAS IMAGINE/ER MAPPER	Used for processing ASTER and airborne geophysical datasets
3	ArcMap	Used for producing final maps
4	Oasis Montaj	Used for processing airborne geophysical datasets
5	SPSS	Used for statistical analysis
6	STcorr2015	Used for topographic correction
7	Rockworks15	Used for producing rose diagrams

4. METHODOLOGY

This research involved three phases of processing: the first one was processing the ASTER images including topographic correction using DEM products and STcorr2015 software, deriving apparent thermal inertia, and calculating Normalized Difference Vegetation Index (NDVI) from ASTER VNIR bands. The second phase involved testing the discrimination of outcrops from cover using other dataset products to check the spatial relationship between the thermal and other dataset products, developing methods for discrimination & quantitative interpretation using DEM, ASTER NST & ATI products, and structural investigation. The third phase involved statistical analysis of ASTER NST, ATI & NDVI by using the lithological boundaries, ranges of values from ASTER NST, ATI & slope products as ROIs.

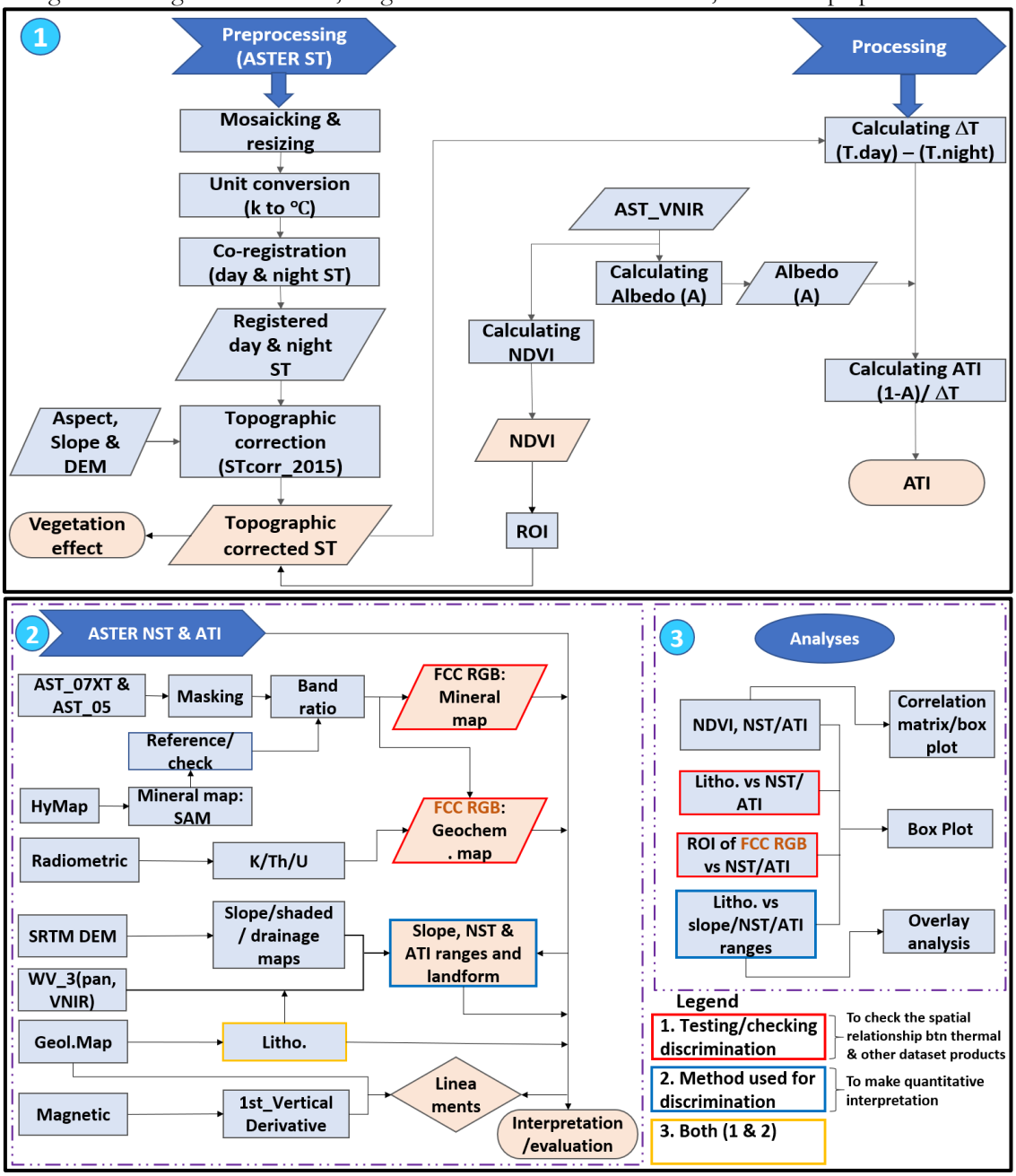

Figure 3 Methodological flow chart. ST stands for surface temperature; ATI is apparent thermal inertia; ΔT is a temperature difference between day & night; Litho is lithology, and SAM is Spectral Angle Mapping. The HyMap was used as a reference (check) for the surface minerals.

4.1. Processing ASTER imageries

4.1.1. Generating topographically corrected ASTER NST and deriving ATI

Geometric and radiometric corrected ASTER level-2 day and night-time surface kinetic temperature imageries were downloaded from the NASA website. Both the day and night-time surface temperature imageries have been mosaicked, registered using ground control points, and the unit was converted from Kelvin to degree Celsius as the input surface temperature was in Kelvin with the scale factor of 0.1. In the relief affected terrain like the study area, the lapse rate, the rate of change of temperature with elevation, and heating and shadowing effects could be high and need to be corrected using DEM products (Ulusoy et al., 2012). So that, two accessed images of SRTM DEM with 30m ground resolution were mosaicked, re-projected to UTM zone 33_South projection and WGS_84 datum, resampled to 90m and resized to the study area size. Slope and aspect were generated using ENVI software from the DEM and used as an input for the topographic correction of the ASTER ST imagery. The topographic effects were corrected by using a stacked layer combination of surface temperature, slope, aspect and SRTM DEM with 90m spatial resolution. This correction was conducted using the software STcorr2015 which is an IDL based program (Ulusoy et al., 2012). The algorithm of the software calculates the lapse rate, aspect gradient and slope gradient based on the selected degree of polynomial to correct the topographic issues (Ulusoy et al., 2012), as the flow of this procedure is shown in appendix 15. The result was useful as it has enhanced some thermal anomalies and reduced the false thermal anomalies (Ulusoy et al., 2012). The output image after the correction showed the temperature differences relative to the mean temperature of the image scene subset (Ulusoy, 2016).

The potential of topographically corrected night-time surface temperature imagery for discriminating the outcrops from unconsolidated cover has been evaluated in this study. The maximum day time temperature is usually in the afternoon between 14:00 -15:00 whereas the minimum temperature is before sunrise between 04:00 – 05:00 local time (Beeson et al., 2011). However, one of the limitations with this ASTER ST imagery was that it's not acquired at the optimal times. The day and night-time imageries were used to calculate the change in temperature (ΔT) observed and processed for the ASTER acquisitions provided. This temperature change could be different for different materials (see figure 4) and was later used for calculating apparent thermal inertia. ATI can be used as an estimation of the actual thermal inertia, and it could be calculated using the equation: ATI=(1-A)/(ΔT) (Beeson et al., 2011; Kahle, 1987; Mitra & Majumdar, 2004; Price, 1977). Albedo image, which is the ratio of reflected to incident radiant, could provide important information about the absorbed energy by the material (Ramakrishnan et al., 2013), and it was constructed from the ASTER VNIR band 1 (b1) and band 3 (b3) using the formula developed by Mokhtari et al. (2013) shown in Equation 2.

$$ATI=(1-A)/(\Delta T) \quad \ldots\ldots (1)$$

$$A=0.697*b1 + 0.298*b3+0.008 \quad \ldots\ldots (2)$$

Where: A is albedo, ΔT is temperature difference, b1 is band1 & b3 is band3
ATI is apparent thermal inertia

The thermal inertia values of some geological materials illustrated in table 4 were used to cross-check with the derived ATI values in this research. Thermal inertia is the resistance of a material to the change in temperature, and is determined by the density (ρ), thermal conductivity (k) and specific heat (c) of the material and has a unit of measurement: **cal cm^{-2} s$^{-1/2}$ °C^{-1}** as (Xue & Cracknell, 1995).

$$P=(\rho k c)^{1/2} \quad \ldots\ldots (3)$$

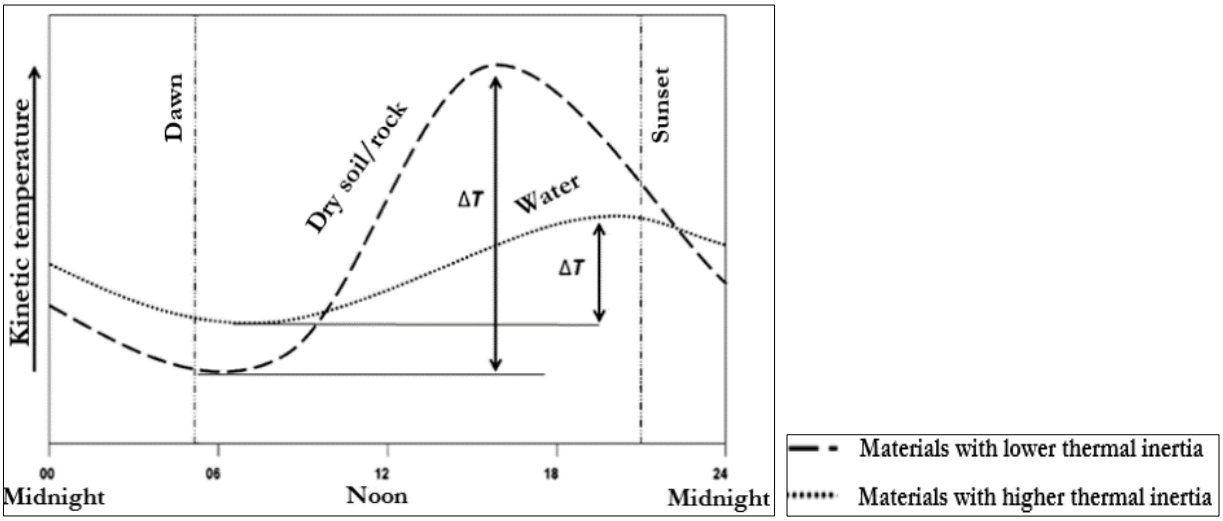

Figure 4 Diurnal temperature variation of rock/soil and water (after Lillesand et al., 2015)

Table 4 Thermal properties of some geological materials (after Gupta, 2003)

Geological materials	K Thermal conduc-tivity [cal cm^{-1} s^{-1} $°C^{-1}$]	ρ Density [g m^{-1}]	c Specific heat cal [g^{-1} $°C^{-1}$]	k Thermal diffusivity [cm^{-2} s^{-1}]	P Thermal inertia cal [cm^{-2} $s^{-1/2}$ $°C^{-1}$]
Igneous rocks					
Basalt	0.0050	2.8	0.20	0.009	0.053
Gabbro	0.0060	3.0	0.17	0.012	0.055
Peridotite	0.0110	3.2	0.20	0.017	0.084
Granite	0.0075	2.6	0.16	0.016	0.052
Rhyolite	0.0055	2.5	0.16	0.014	0.047
Syenite	0.007	2.2	0.23	0.009	0.047
Pumice, loose	0.0006	1.0	0.16	0.004	0.009
Sedimentary rocks					
Sandy soil	0.0014	1.8	0.24	0.003	0.024
Sandstone, quartz	0.0120	2.5	0.19	0.013	0.054
Clay soil	0.0030	1.7	0.35	0.005	0.042
Shale	0.0042	2.3	0.17	0.008	0.034
Dolomite	0.0120	2.6	0.18	0.026	0.075
Limestone	0.0048	2.5	0.17	0.010	0.045
Metamorphic rocks					
Marble	0.0055	2.7	0.21	0.010	0.056
Quartzite	0.0120	2.7	0.17	0.026	0.074
Slate	0.0050	2.8	0.17	0.011	0.049
Other materials					
Water	0.0013	1.0	1.01	0.001	0.037

4.1.2. Calculating NDVI using ASTER VNIR bands for analyzing the vegetation effect

The NDVI was calculated using both the 2015 and 2018 ASTER VNIR imageries in ENVI 5.5 band math tool and a formula: ASTER band function: (Band3-Band2)/(Band3+Band2). The NDVI values could range from -1 to +1 based on the density of green vegetation (Rani et al., 2018). Regions of interest (ROI) have been manually selected on the study's inferred outcrops and unconsolidated cover from the less vegetated and moderately vegetated seasons of the 2015 and 2018 years respectively. The statistical values obtained from ASTER NST and the calculated NDVI using the chosen ROIs from the respective years have been used for correlation and box plotting statistical analysis. The analysis results were used to determine the effect of vegetation on discrimination of outcrops from unconsolidated cover.

4.2. Testing the discrimination of outcrops from unconsolidated cover using other dataset products

Testing of the topographically corrected ASTER NST and the derived ATI for discriminating outcrops from unconsolidated cover was conducted by using other datasets such as the geological map of Haib, ASTER mineral map, and FCC RGB geochemical map generated from the combination of ASTER mineral map products and radioelement from radiometric data (see figure 3 red colour outlines). The test discrimination ***aimed*** to understand the spatial ***relationship*** between the thermal and other dataset products. Based on the results of the observed relationship from the test discrimination, methods were developed for discrimination and quantitative interpretation of outcrops and unconsolidated cover. The procedures followed in this research for generating products from other datasets for ***testing*** the discrimination is briefly explained in the following subsections.

4.2.1. Testing the discrimination using the geological map of Haib

The geological map of Haib at a scale of 1:100,000 comprised of twelve various lithological units and structures produced by Blignault (1972) has been used for the test discrimination. The geological map has been georeferenced with UTM zone 33_South projection and WGS_84 datum. The map was digitized using ArcMap software and draped over the ASTER NST & ATI products for testing the discrimination of solid outcrops from unconsolidated cover by observing the spatial relationship between them. The lithological unit boundaries were used as ROIs to generate statistical information from ASTER NST and ATI products. The relationship and the possible discrimination potential of the different lithological units were statistically tested. Linear stretching was applied to enhance and observe optimum variation in the ASTER NST and ATI values between the lithological units

4.2.2. Testing the discrimination using ASTER mineral map

Test discrimination was also conducted using ASTER mineral map product. So, the VNIR, SWIR, and TIR ASTER level 2 surface reflectance and emissivity data were used for mapping the surface minerals within the Haib prospect area. The SWIR data was already corrected for cross talk effect due to the leak of photons from band 4 to other SWIR bands (Kalinowski et al., 2004). The VNIR and TIR (emissivity) bands were resampled to 30m spatial resolution with nearest neighbour resampling, and all bands were combined using ENVI's Layer Stacking procedure. Masks have been built from NDVI imagery and applied to exclude the effect of green vegetations. Since the narrow bandwidth of the ASTER SWIR sensor and the additional TIR sensor allows mapping of mineral indices (van der Meer et al., 2012), the mineral mapping was conducted using the band ratio algorithms and linear histogram stretches suggested by Cudahy (2012) (see table 5). However, the index values of Ferric oxide and silica (quartz) were not appropriate with the suggested stretch thresholds. So that, their stretch values were determined by taking the spectra from the original image and compare it with USGS library resampled to ASTER for the particular mineral (group) being examined. The band ratio algorisms of (band 4/band 3), (band 5+band 7)/ (band 6), and (band 6/band5) were used to generate the FCC RGB combination of ***ferric oxide, aluminum hydroxide*** and ***kaolin mineral map***. This mineral map was used to interpret the weathered or regolith materials together with DEM products (shaded relied) since the existence and distribution of surface minerals such as kaolin and iron oxide can be related to ***regolith materials*** (Agustin, 2017). So that, the mineral map was used to ***test/check*** the spatial relationship between the surface mineral groups (Kaolin and iron) and thermal products by overlaying one to the other.

Table 5 ASTER band ratio and linear stretch (adapted from Cudahy, 2012)

No.	Mineral	Algorithm	Linear stretch
1	Ferric oxide (Fe_2O_3)	Band4/Band3	1.097-1.419
2	Aluminum hydroxide (AlOH)	(B5+B7)/B6	2.01-2.256
3	Kaolin group index	Band6/Band5	1.0-1.125
4	Ferrous hydroxide (FeOH)	(B6+B8)/B7	2.02-2.245
5	Magnesium hydroxide/carbonate (MgOH)	(B6+B9)/(B7+B8)	1.050-1.21
6	Silica index	B13/B10	0.992-1.119

4.2.3. HyMap data

The airborne hyperspectral HyMap data was available for a certain portion of the study area and used for mapping surface minerals. The HyMap data was registered, mosaicked and resized using Envi software (Visual Information Solutions, 2009). This step was followed by wavelength mapping using hyperspectral python (HypPy) software which calculates the wavelength position of the deepest absorption feature and helps to obtain information about the minerals (Van Ruitenbeek et al., 2014). Spatial-spectral endmember extraction (SSEE) method was used to extract endmembers since the algorithm is effective in reducing the noise, and make spectrally low contrast endmembers detectable (Pargal et al., 2011). Endmembers library has been built using the spectral signatures extracted from SSEE, and this step was followed by Spectral Angle Mapping (SAM) (Kruse et al., 1993) to generate the mineral map. The minerals identified from HyMap was used to cross-check/reference the mineral groups identified by ASTER band ratio mineral products (see appendix 16).

4.2.4. Testing the discrimination using the combined product of radiometric and ASTER group minerals

The airborne radiometric grids of potassium (K), thorium (Th) and uranium (U) were already pre-processed and corrected for errors by the data provider. The gamma rays that are emitted from the rocks and unconsolidated materials from a depth of about 30-50 cm and could be detected by the airborne radiometric sensor ("Geoscience Australia," 2014). A ternary map was produced from the K, Th and U grids, and enhanced using 99% histogram equalization. It was used to inspect the relative distribution of the radioelements (Dentith & Mudge, 2014) (see appendix 13). When the ternary map was generated using ER Mapper software, the relative distribution of the radioelements was controlled by using the geological unit boundaries and the statistical values of the radioelements. The statistical values of the radioelements were created by calculating zonal statistics using the radioelement grids and lithological unit boundaries in ArcGIS (see appendices 9-11). Hence, the FCC RGB combination ***geochemical map*** was produced using ferric oxide (***Fe_2O_3***) and magnesium hydroxide (***MgOH***) of the interpreted surface mineral products from ASTER; and Thorium (***Th***) from radiometric grids (see figure 12 e). This geochemical map was used to ***test*** the discrimination of outcrops from unconsolidated cover since ferric oxide and thorium-rich could be associated with unconsolidated materials, and ferric oxide rich and thorium poor could be associated with outcropping solid rocks (Hewson et al., 2006). The association of minerals (ferric oxide & Kaolin) with the unconsolidated cover could be possible due to the occurrence of ***lateritic*** regolith in the Namaqua Natal province (Thomas et al., 1994). ROIs were selected using the geochemical map targeting to ferric oxide and thorium-rich, and ferric oxide rich and thorium poor regions respectively. Later, these ROIs were used to generate statistical information from ASTER NST and ATI products. The information generated from both ASTER NST and ATI were plotted using SPSS statistical software, which is powerful for statistical analysis (Landau et al., 2004) to ***test*** and ***analyze*** the discrimination of unconsolidated cover materials from outcropping rocks.

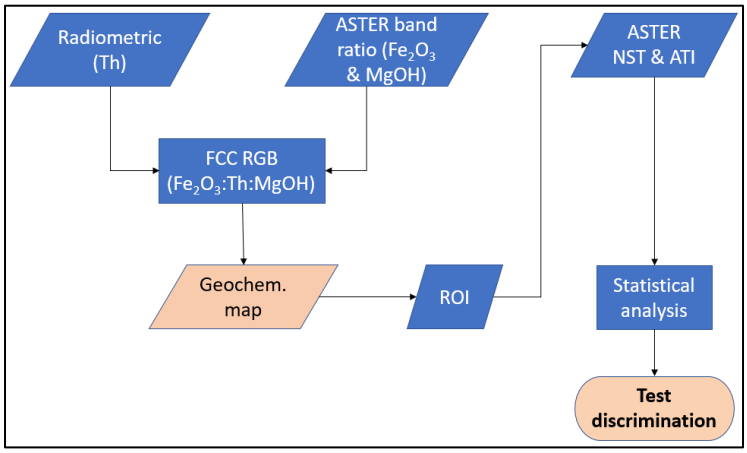

Figure 5 A method used to combine Fe_2O_3, Th and MgOH to test the ASTER NST & ATI for discriminating outcrops from unconsolidated cover.

4.3. Methods developed to discriminate outcrops from unconsolidated cover, and quantitative interpretation using ASTER NST and ATI

A method which enables to discriminate the outcropping units from unconsolidated cover for quantitative interpretation was required. So that, slope angle ranges and ASTER NST & ATI ranges of values have been developed in this study and used for the intended discrimination and quantitative interpretation purposes (see figure 3 blue color outlines), and the procedure is briefly explained below.

4.3.1. Slope angle range method

The slope angle ranging technique was developed using the slope map derived from DEM. The generated slope map was classified to select ***slope angle ranges*** that can represent the outcrops and unconsolidated cover. These slope angle ranges by themselves were evaluated, for how well they can fit with the landform, by draping other dataset products on the classified slope map. For example, the ***flat/gentle slope angle ranges*** were selected by overlaying the digitized ***sediment*** (Karoo sediments & alluvial sediments) unit boundaries of the Blignault (1972)'s geological map on the classified slope map and checking their spatial fitness/colocation (see appendices 1 and 2). These slope angle ranges were converted from raster to vector file format and evaluated also by overlaying them with WV_3 (panchromatic) and google earth respectively for a subset of the study area (see appendices 5 and 6). The same procedure was followed to select the ***steeper slope angle range*** that represents the outcrops. The slope angle ranges were also statistically analyzed to determine their usefulness/quality to discriminate the outcrops from unconsolidated cover. Hence, the selected slope angle ranges were used as a ***threshold*** to spatially ***discriminate*** the outcrops from unconsolidated cover using ASTER NST and ATI products for visual observation. Finally, the slope angle ranges were used to evaluate the potential of ASTER NST and ATI to discriminate the outcrops from unconsolidated cover units and interpret quantitatively using an ***overlay*** analysis based on the area of ***intersection*** between the slope angle ranges and lithological unit vectors. The lithological units were classified into the assumed unconsolidated units (alluvial, colluvial and Karoo sediments) and outcropping units for the overlay analysis purpose.

4.3.2. ASTER NST and ATI range method

Another method to discriminate solid outcrops from unconsolidated cover for quantitative interpretation was also developed using ASTER NST and ATI products with the control of other datasets such as the geological map of Haib. So that, the surface temperature and apparent thermal inertia ranges of values from the ASTER NST and ATI products where the clear demarcation of change in surface temperature and apparent thermal inertia values were observed and best fitted with the lithological units were selected respectively (see appendices 3 & 4). The low and high surface temperature ranges (ASTER NST range_1

and ASTER NST range_2) respectively from ASTER NST; and the low and high apparent thermal inertia ranges (ATI range_1) and (ATI range_2) respectively from ATI have been selected which represented the outcrops and unconsolidated cover. The selected ASTER NST and ATI ranges were evaluated statistically for their quality and how well they can be used for the discrimination. Hence, the selected ranges of values were used as a ***threshold*** to spatially ***discriminate*** the outcrops from unconsolidated cover using ASTER NST and ATI products for visual observation. Finally, an ***overlay*** analysis was applied using the selected ASTER NST and ATI ranges of values and the lithological unit boundaries in ArcMap for quantitative interpretation to assess the capability of ASTER NST and ATI to discriminate outcrops from unconsolidated cover.

4.4. Structural interpretation, evaluation, and integration

4.4.1. Structure detection using ATI

The altitude, aspect and slope effect corrected ASTER NST and the derived ATI have been evaluated for their capability to identify geological structures. Lineaments were interpreted from the derived ATI product based on the visual interpretation techniques. The past geological map of Haib (Blignault, 1972) was also used for interpreting and checking the lineaments inferred from ATI, how they were corresponding to each other. Lineaments with apparent thermal inertia value of above 0.027°C^{-1} and length of above 250 m were drawn from ATI using ArcMap. In addition to lineaments, palaeochannels and sand dunes were also identified from ATI. Sand dunes which were identified from ATI were interpreted using WV_3 (panchromatic) image and compared with the emissivity spectra of quartz from Johns Hopkins University (JHU). A drainage map, assuming 6 order streams, were generated from the SRTM DEM using the Arc Hydro extension tool in ArcMap. Hence, the generated drainage map was overlain with ASTER NST and ATI images and checked for their possible co-location or otherwise with the current active drainages to interpret possible palaeochannels. This follows example investigations for palaeochannels elsewhere (Mackey et al., 2000; Thakur et al., 2016; Hewson et al., 2015).

4.4.2. Lineament detection using airborne magnetics

The airborne magnetic data used for this research was a pre-processed total magnetic intensity (TMI) with a spatial resolution of 50m. A reduced to magnetic pole (RTP), which positions the magnetic anomalies directly over the magnetic body (Dentith & Mudge, 2014), was calculated using from the total magnetic intensity in Oasis Montaj software. The magnetic inclination and declination of the study area were -66.201 and -19.9 respectively as this information was obtained from ("British Geological Survey," 2019). High frequency filtered TMI such as tilt angle, 1VD, 2VD and 1HD derivatives in grey scale could enhance linear features, that could be related to geologic structures, were calculated using Oasis Montaj MAGMAP GX extension tool (Oha et al., 2016). Such derivatives were useful to generate the near-surface structural information (Hewson & Robson, 2014). The first vertical derivative (1VD) which is a vertical gradient that measures the rate of change of magnetic field strength per a unit change in elevation; and it is an edge detector that accentuates the shallow depth features (Dentith & Mudge, 2014; Oha et al., 2016). The first vertical derivative (1VD) was chosen as it has identified the structures better and clear with less noise than other derivatives. Lineaments that were clearly visible on the 1VD image with magnetic field intensity of above 0.008 nT/m and lateral length of above 250 m were drawn manually in ArcMap. These lineaments identified from 1VD was used to ***evaluate*** the potential of ATI by comparison, and to study the benefit of the ***integration*** of the results of the two methods using ArcMap.

4.4.3. Evaluation and integration of the lineaments of ATI with airborne magnetics (1VD)

The potential of ATI to detect lineaments were evaluated using the calculated 1VD magnetics product and integrated using ***integrate*** tool in ArcMap to evaluate the benefit of integrating the results of ATI with 1VD magnetics. For integrating the lineaments that were identified from the two methods, tolerance of 50

m was chosen, and the lineaments located within this tolerance would be snapped automatically to the 1VD lineaments.

4.5. Statistical analyses

4.5.1. Correlation matrix analysis

The effect of green vegetation from different seasons on the ASTER NST was statistically analyzed by estimating the correlation between the variables using a correlation matrix. For this purpose, the NDVI of the respective year's imageries, the one acquired during non-vegetation and the other during moderate vegetation seasons, were calculated using the VNIR bands of the ASTER imageries. Region of interests (ROIs) were chosen from the ASTER NST, ATI, and NDVI products by targeting the assumed outcrops and unconsolidated cover using the geological map as a reference. Subsequently, a correlation matrix was created to examine the relationship between the variables and to analyze the effect of vegetation from different seasons on outcrops and cover discrimination.

4.5.2. Box plot analysis

Box plots, unlike the bar charts, are easy to compare different groups at a time (Nuzzo, 2016). The box plot comprises five population frequency components such as lower extreme (minimum), upper extreme (maximum), quartile first (25%), median (50%) and quartile third (75%) (Adam et al., 2018; Nuzzo, 2016) as shown below in figure 6. The lower and upper extreme values could be determined from interquartile range (IQR), quartile first (Q1) and quartile third (Q3) by subtraction and addition of 1.5*IQR from Q1 and Q3 respectively; and values beyond these ranges are considered as outliers (Adam et al., 2018; Babura et al., 2018). In addition to the correlation matrix analysis, the effect of vegetation was also analyzed using boxplots by generating statistical information from ASTER NST imagery using the ROI's. Box plotting was also used for statistical analyses of the discrimination of outcrops from unconsolidated cover.

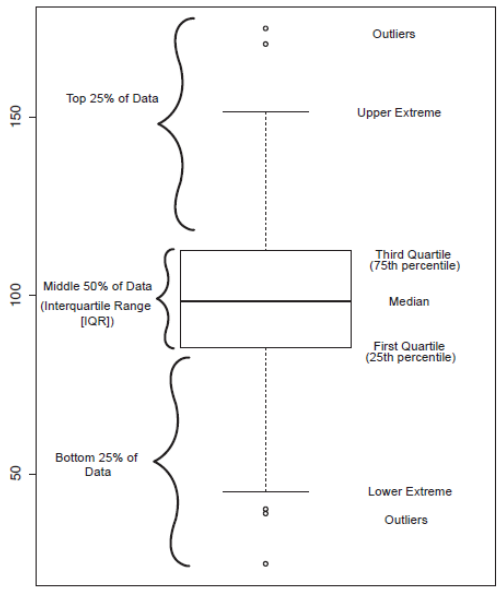

Figure 6 Annotated box plot after Adam et al. (2018)

Lower extreme=Q1-1.5*IQR……...……(4)

Upper extreme= Q3+1.5*IQR……(5)

5. RESULTS

5.1. Introduction

In this chapter, the results are presented corresponding to the methodology chapter. These results were the outcomes when the methodologies described in the previous chapter four were applied by using the datasets (see table 1 and 2) and various software listed in table 3. The results presented include the ASTER NST and ATI products before and after topographic effect corrections, other dataset products that were used for testing the discrimination, the discrimination results using ranges of values, overlay analysis and quantitative interpretation, structural analyses, and analyses of the effect of green vegetation. In this study, two pairs of imageries were used to analyze the effect of green vegetation; however, all the rest analyses were conducted using only the 2015-year pair of imagery acquired at the less vegetation period.

5.2. ASTER processing results

5.2.1. ASTER night-time surface temperature and apparent thermal inertia products

The two pairs of day and night-time surface kinetic temperature imageries acquired in 2015 and 2018 were pre-processed and corrected for altitude, slope and aspect topographical effects using the method mentioned in chapter four (see chapter 4, 4.1). These surface kinetic temperature imageries, which are shown as rainbow color which ranges from the lowest temperature (dark blue) to the highest (red) color represented the surface temperature value of various lithological units. Before the topographic effect correction of the pairs of imageries, the rocks that were in topographically lower elevations have been shown with high surface temperature and those in the higher elevations have been shown as low surface temperature. These effects of topography have been eliminated after the correction, and the landforms remain with the characteristic surface temperature values (see figure 7 a to d). The day and night-time surface temperature together with the albedo products were also further processed to derive apparent thermal inertia for the respective years (see figure 7 e & f). The corrected night-time surface temperature and the derived apparent thermal inertia products were assessed for discriminating the outcrops from unconsolidated cover and the potential for detecting structures.

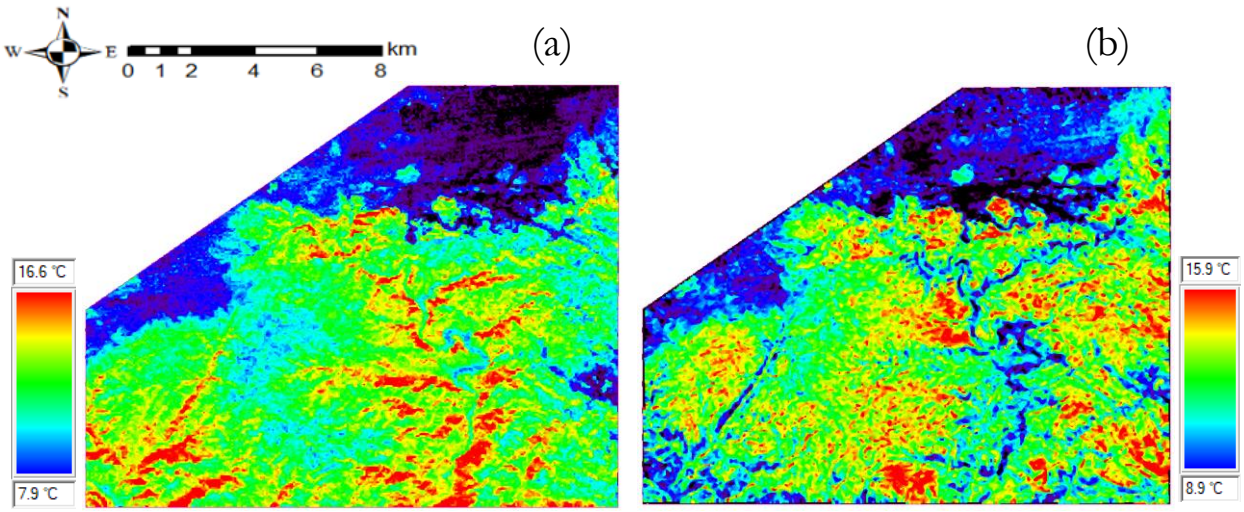

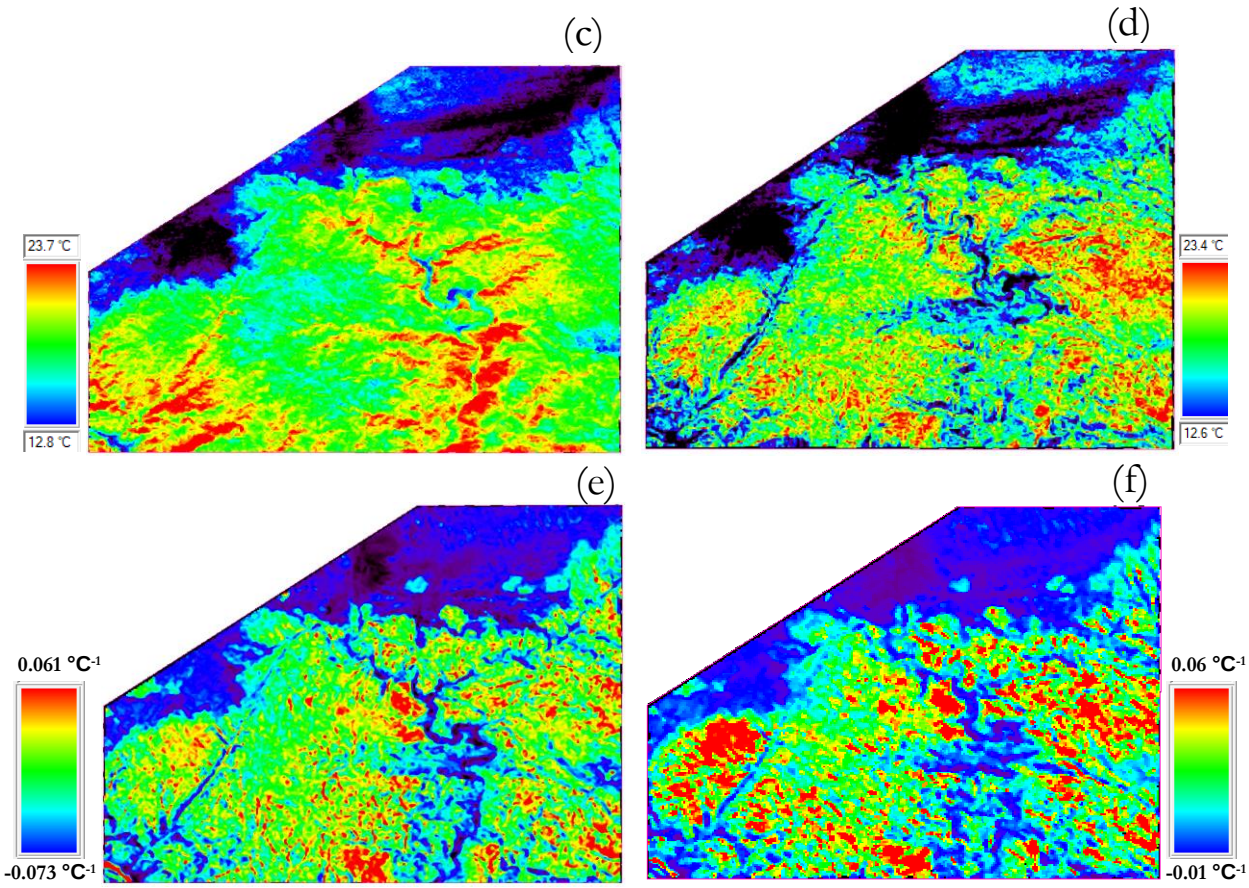

Figure 7 ASTER NST acquired on July-2015 & May-2018 before topographic correction (a and c), after topographic correction (b and d), and the derived ATI (e and f)respectively.

5.3. Results of the testing discrimination of outcrops from unconsolidated cover using the other dataset products

The datasets including the lithological unit vectors, ASTER mineral map, DEM products and geochemical map of the FCC RGB combination of Radiometric and ASTER mineral products were used to ***test*** the capability of the topographically corrected ASTER NST and the derived ATI products for discriminating the outcrops from unconsolidated cover. The testing results enabled to understand the relationship between the thermal and the other dataset products, and that helped to establish a method to discriminate the outcrops from unconsolidated cover for a quantitative interpretation. In this section, only the test discrimination results are presented.

5.3.1. Testing the discrimination using lithological unit vectors

The lithological unit vectors, that were digitized from the geological map of Haib (Blignault, 1972), were overlain with ASTER NST and ATI products to ***test the discrimination*** of the outcrops from unconsolidated cover. Linear stretching from 10.245 to 15.219 °C and from 0.015 to 0.039 °C^{-1} to the ASTER NST and ATI images were applied respectively in order to enhance and obtain optimum variation in surface temperature and apparent thermal inertia values among the different lithological units. The ***low surface temperature and ATI*** values which are shown as blue color were corresponding with Karoo sediments and alluvial sediments (***unconsolidated cover***) whereas the ***high*** values ranging from cyan to red colors were corresponding with the competent solid rocks (***outcrops***) as it was observed from the overlay of the lithological units and thermal products as shown in the figures 12 a and b. The difference in surface temperature and apparent thermal inertia between the solid rocks and the unconsolidated cover was ***significant***. On the other hand, the difference in surface temperature and apparent thermal inertia between different outcropping rocks appeared very low and did not show distinct boundary that

corresponds with the lithological unit vectors except hornblendite diorite and porphyritic adamellite (see figure 12 a and b). The statistical analysis between ASTER NST and lithological units show clearly the separability of unconsolidated cover from outcrops; however, the solid rocks could not be separated from each other except hornblendite diorite and porphyritic adamellite (see figure 8).

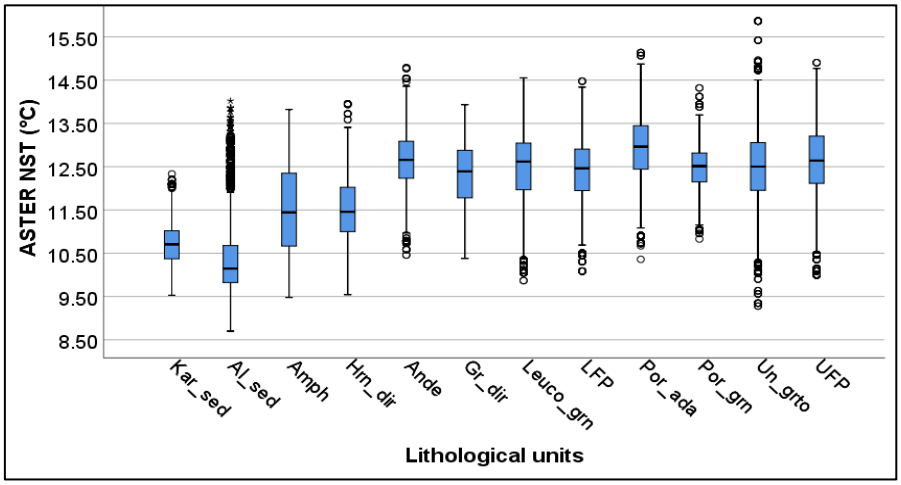

Figure 8 ASTER NST distribution plot between lithological units of Haib (Blignault, 1972) (see figure 6 for the meaning of symbols)

The analysis between ATI and lithological units have also shown the separability of unconsolidated cover from outcrops. Nevertheless, the various solid rocks could not be separated from each other except hornblendite diorite and porphyritic adamellite similar to the above ASTER NST result (see figure 9).

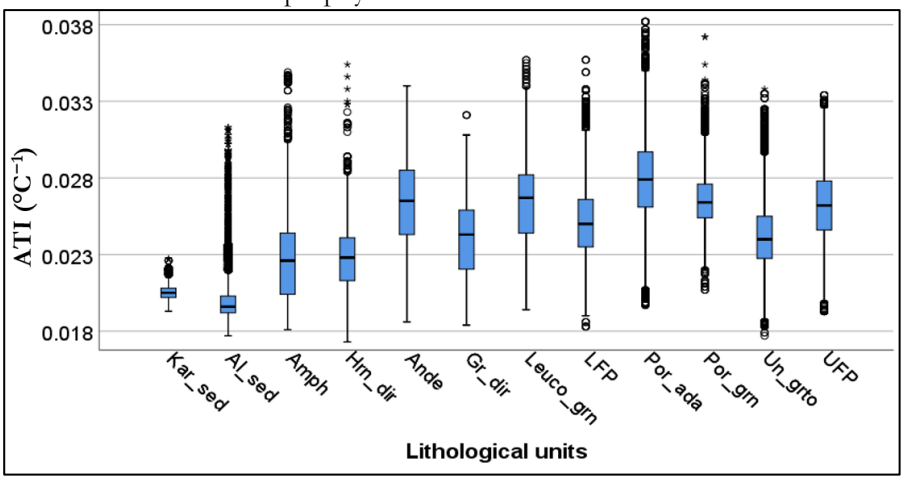

Figure 9 ATI distribution plot between lithological units of Haib (Blignault, 1972)

Table 6 Abbreviations used for the lithological units

Abbreviation	Lithological units	Abbreviation	Lithological units	Abbreviation	Lithological units
Kar_sed	Karoo sediment	Ande	Andesite	Por_ada	Porphyritic adamellite
Al_sed	Alluvial sediment	Gr_dir	Granodiorite	Por_grn	Porphyritic granite
Amph	Amphibolite	Leuco_grn	Leucogranite	Un_grto	Undifferentiated granitoid
Hrn_dir	Hornblendite diorite	LFP	Lower feldspar porphyry	UFP	Upper feldspar porphyry

5.3.2. Testing the discrimination using ASTER mineral map

The distribution of surface minerals was mapped using the band ratio algorithms with the corresponding stretches listed in table 5. The FCC RGB of ferric oxide, aluminum hydroxide and kaolin mineral map was produced from the band ratio products and used to interpret the composition of surficial materials. In order to avoid the confusion of the minerals taken in the FCC RGB with the other minerals such as magnesium hydroxide, iron hydroxide and quartz, masking was applied to these other mineral groups. The red color shows the geological materials rich in ferric oxide; green color shows the abundance of aluminum hydroxide and the blue one is the lithological units rich in kaolin (see figure 12 c). The yellow and magenta colors show the lithological units rich in ferric oxide and aluminum hydroxide, and ferric oxide and kaolin respectively as illustrated in the ASTER mineral map. The mineral ***Kaolin*** which is represented as blue color in the mineral map could infer the ***unconsolidated cover*** materials that could be formed due to the weathering of ***feldspar-rich granitic*** rocks which is abundant in the study area, and the ferric oxide represented as reddish tint color could also be related to iron-rich ***regolith*** materials. Interpretation was supported by DEM products such as shaded relief (see figure 12 d) as topography could be related to geology. For example, the blue color in the mineral map inferred as Kaolin is topographically ***flat/gentle*** slope where surficial materials could be deposited, and it also appeared corresponding with the low surface temperature and ATI values (see figure 12 a, b & c). However, there could be possible confusion in the interpretation of surficial materials with alteration of the host rocks. So that, the ASTER mineral map products were also used in combination with radiometrics to confirm the separation of outcrops from unconsolidated cover as explained in the subsection 5.3.3.

5.3.3. Testing the discrimination using the combined product of interpreted radiometric and ASTER group minerals

The surface minerals using ASTER band ratio, and the radioelements from radiometrics were combined to generate the FCC RGB geochemical map in order to test the capability of ASTER NST and ATI to discriminate outcrops from the unconsolidated cover. The ASTER mineral products were resized and equalized with the airborne radiometrics data. The relative distribution of the radioelements in different lithological units was inspected using zonal statistics between the radioelements and lithological units (see appendices 9-11), and that helped to determine the stretch value for generating a ternary map. The ternary map (see appendix 13) was created as RGB combination of potassium, thorium, and uranium and used to visualize the relative distribution of radioelements. Hence, The FCC RGB ***geochemical map*** of ferric oxide, thorium, and magnesium hydroxide was generated using the method explained in chapter four (see subsection 4.2.4) and enhanced by applying 99% linear histogram stretching. The red color shows lithological units with a higher content of ferric oxide; green shows a high content of thorium and blue shows high content of magnesium hydroxide. The lithologies rich in ferric oxide and thorium are shown as yellow, and those rich in ferric oxide and magnesium hydroxide are displayed as magenta as shown below in figure 12 e. The statistical analysis for ***testing*** the discrimination was conducted using ROIs from the FCC RGB geochemical map based on ferric oxide and thorium content, and the corresponding result is illustrated in the subsequent section.

5.3.3.1. Statistical analysis for testing the discrimination using ROIs from the combined product of interpreted radiometric and ASTER group mineral

The capability of ASTER NST and ATI for discriminating the unconsolidated cover materials from outcropping rocks were statistically ***tested*** using ROIs from the geochemical map. ROIs were selected where ***ferric oxide*** and ***thorium*** were both ***rich***; and ***ferric oxide rich*** whereas ***thorium poor*** regions using the FCC RGB combination of ferric oxide, thorium and magnesium hydroxide ***geochemical map***. The statistical information was generated from ASTER NST and ATI using the selected ROIs and analyzed to test the discrimination. The results show that the ferric oxide and thorium-rich regions corresponded with the ***low*** surface temperature and apparent thermal inertia that represents the

unconsolidated cover materials; whereas the ferric oxide rich and thorium poor regions corresponded with the ***high*** surface temperature and apparent thermal inertia that represents the ***outcropping rocks*** respectively (see figures 10 and 11). The results obtained from the ASTER NST and ATI were consistent.

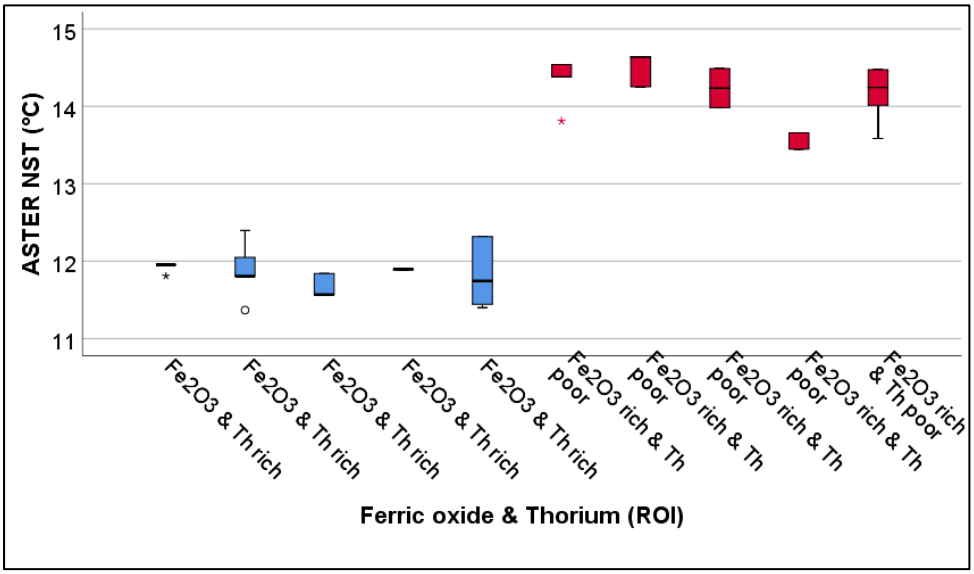

Figure 10 Ferric oxide and thorium-rich (**blue plots**) represent unconsolidated cover, and ferric oxide rich and thorium poor (**red plots**) represent outcrop plotted using ROI targeted on Fe_2O_3 & Th. The ROI's were selected from the geochemical map (see figure 12 e).

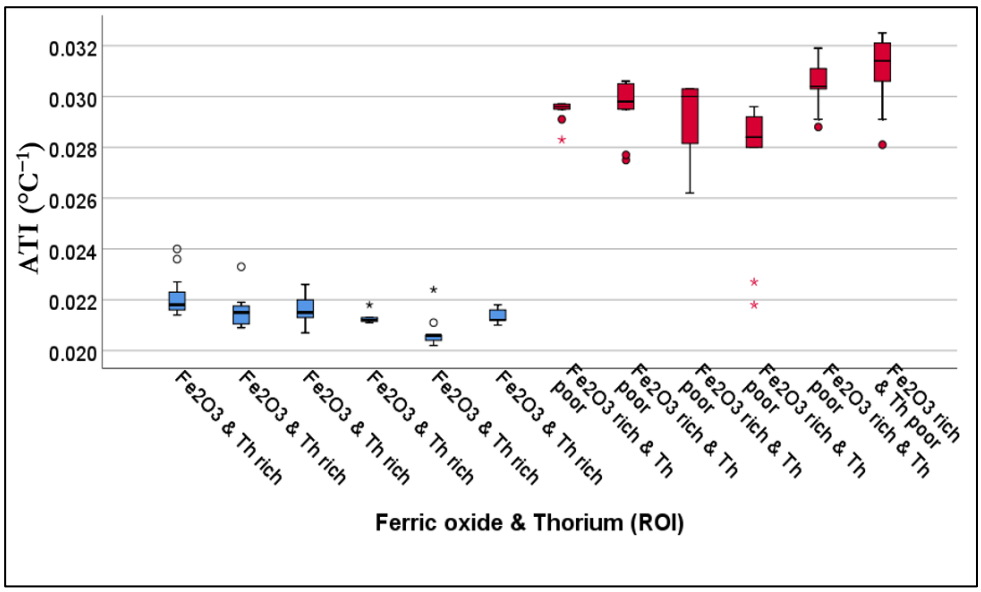

Figure 11 Ferric oxide and thorium-rich (**blue plots**) represent unconsolidated cover, and ferric oxide rich and thorium poor (**red plots**) represents outcrop plotted using ROI targeted on Fe_2O_3 & Th. The ROI's were selected from the geochemical map (see figure 12 e)

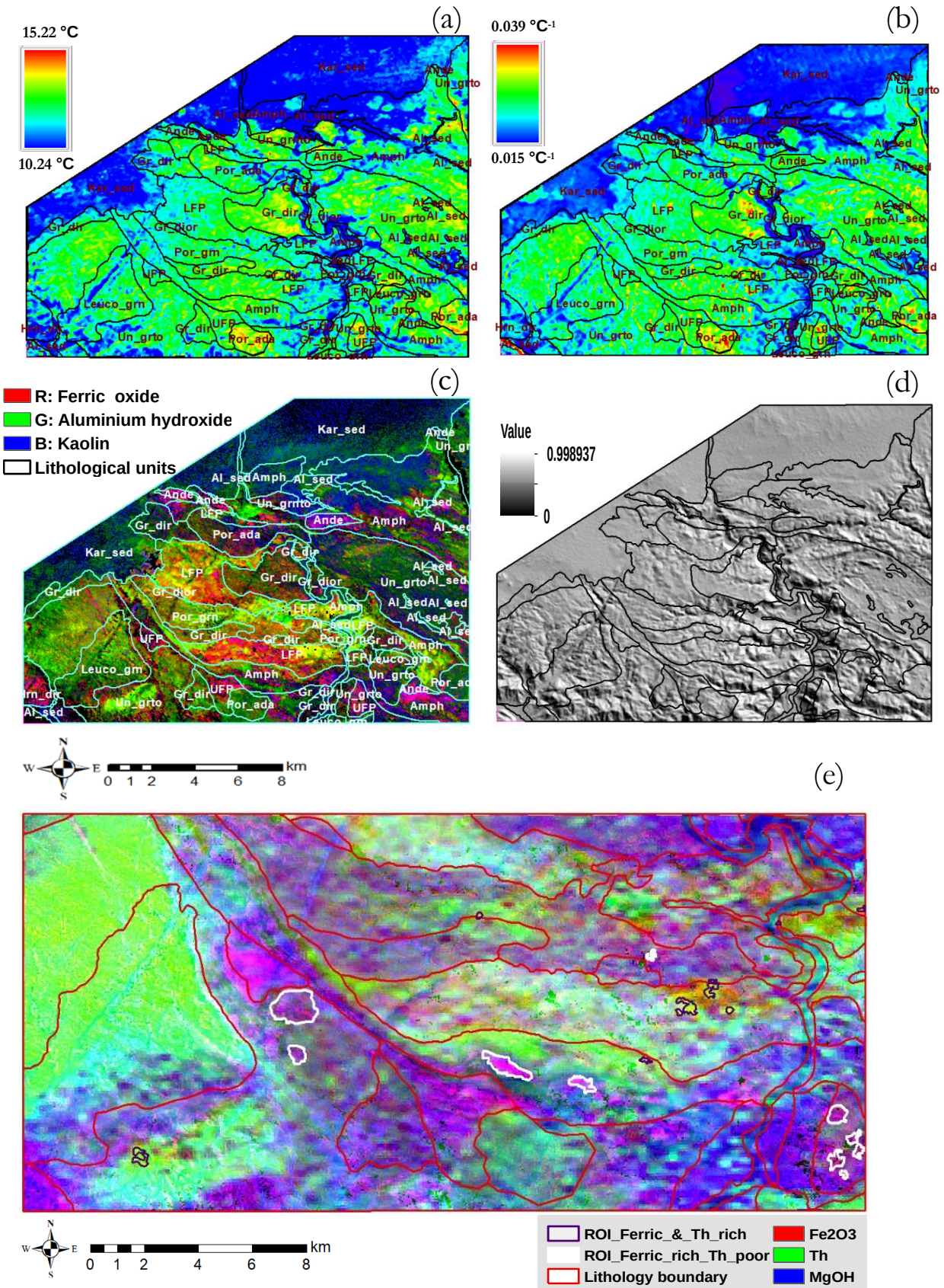

Figure 12 Other dataset products used for testing the discrimination of outcrops from unconsolidated cover. The stretched ASTER NST & ATI products overlain with lithological units (a and b); ASTER FCC RGB mineral map of ferric oxide, aluminum hydroxide and Kaolin (c); shaded relief (d); and FCC RGB of ferric oxide, thorium and magnesium hydroxide geochemical map (e). See figure 1 as a reference for the subset area map (figure 12 e).

5.4. Results of discrimination using slope angle range, ASTER NST and ATI methods and quantitative interpretations

5.4.1. Slope angle ranging method result

Slope angle ranges were developed from the classified slope map generated from SRTM DEM with the help of other datasets as explained in chapter four subsection 4.3.1. The selected slope angle ranges were **0-4^0, 4-6^0 and >6^0** and assumed to represent the ***low***, ***medium*** and ***high*** surface temperature and apparent thermal inertia of the different lithological units respectively. The 0-4^0 & 4-6^0 slope angles ranges inferred the unconsolidated cover whereas the slope angle ranges >6^0 inferred outcrops. These slope angle ranges are presented with the corresponding lithological units which were classified as outcrops (the solid rocks) and unconsolidated cover (karoo sediment and alluvial units) for comparison (see figure 13).

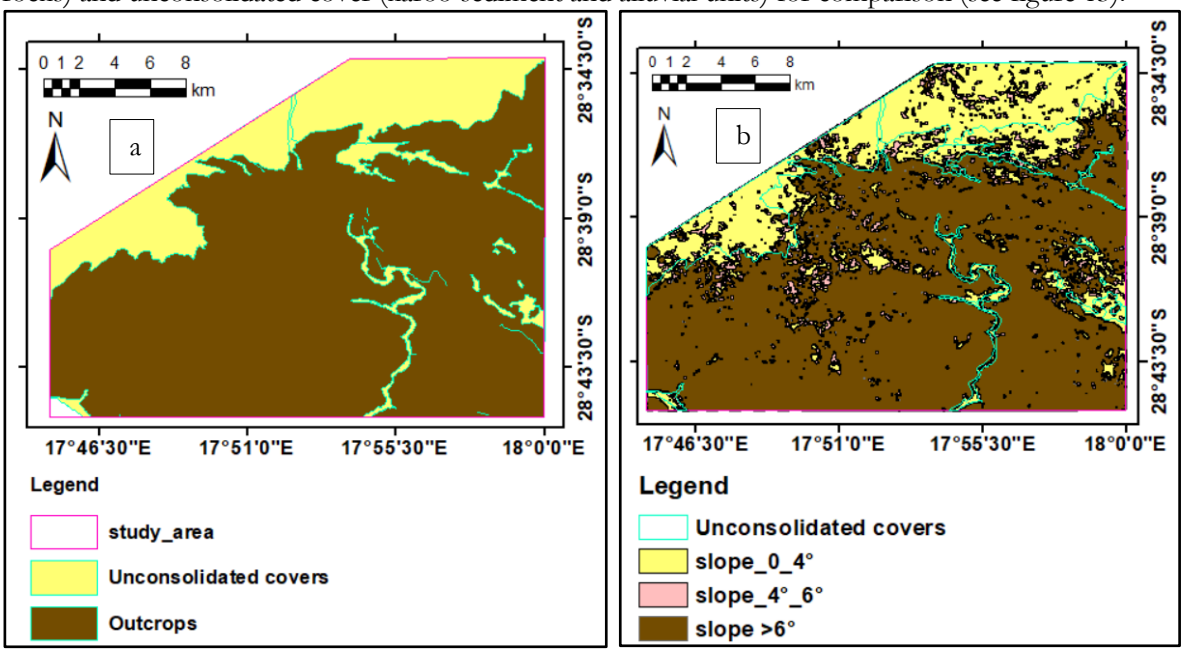

Figure 13 Lithological map classified in to outcrops and unconsolidated cover to compare with the slope angle ranges (a); the slope angle ranges vector files (b).

The vector files of the selected slope angle ranges were used to ***discriminate*** the outcrops from the unconsolidated cover for visual observation using the ASTER NST and ATI products respectively (see figure 14 a & b).

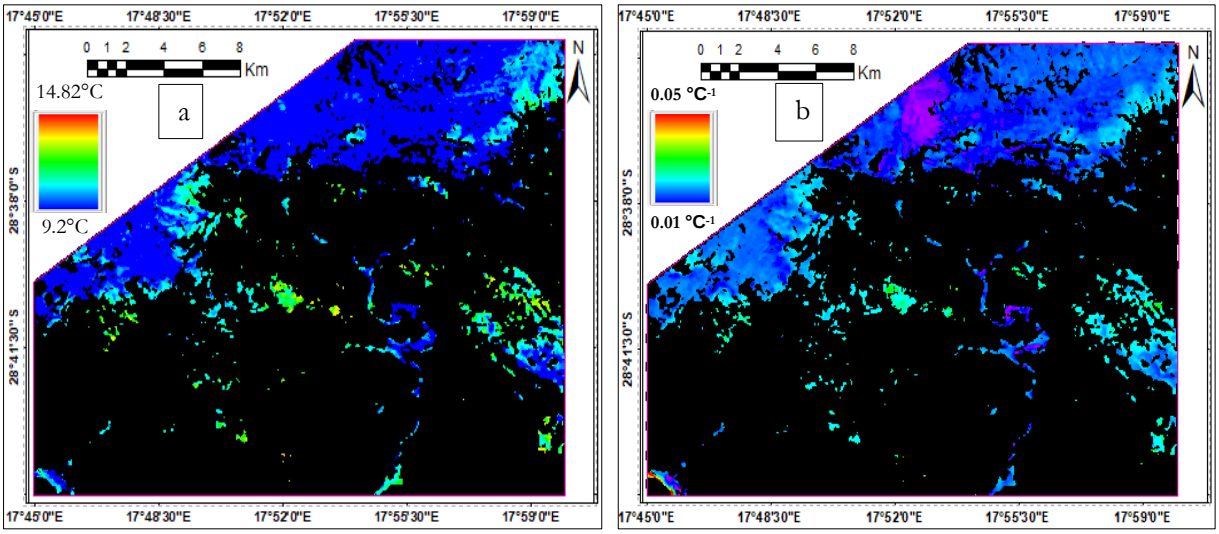

Figure 14 a) ASTER NST discriminated by using 0-4^0 slope angle range & linear stretching applied (9.2 - 14.82°C) and; b) ATI product discriminated by using 0-4^0 slope angle range & linear stretching applied (0.01 – 0.05°C^{-1})

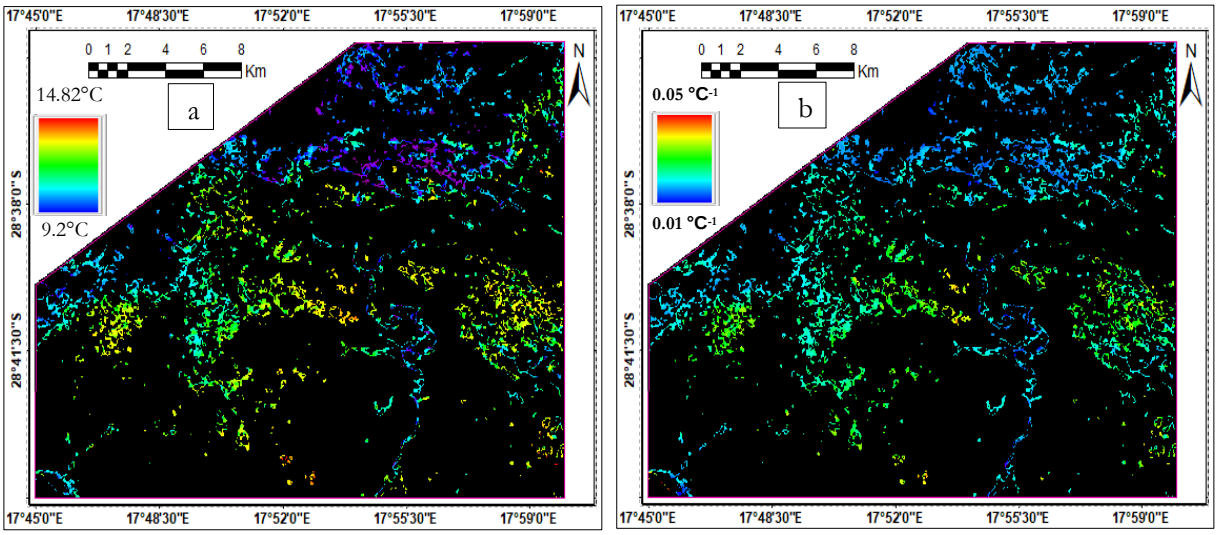

Figure 15 a) ASTER NST discriminated by using 4 - 6^0 slope angle range & linear stretching applied (9.2 - 14.82°C); b) ATI discriminated by using 4 - 6^0 slope angle range and linear stretching applied (0.01 – 0.05°C^{-1})

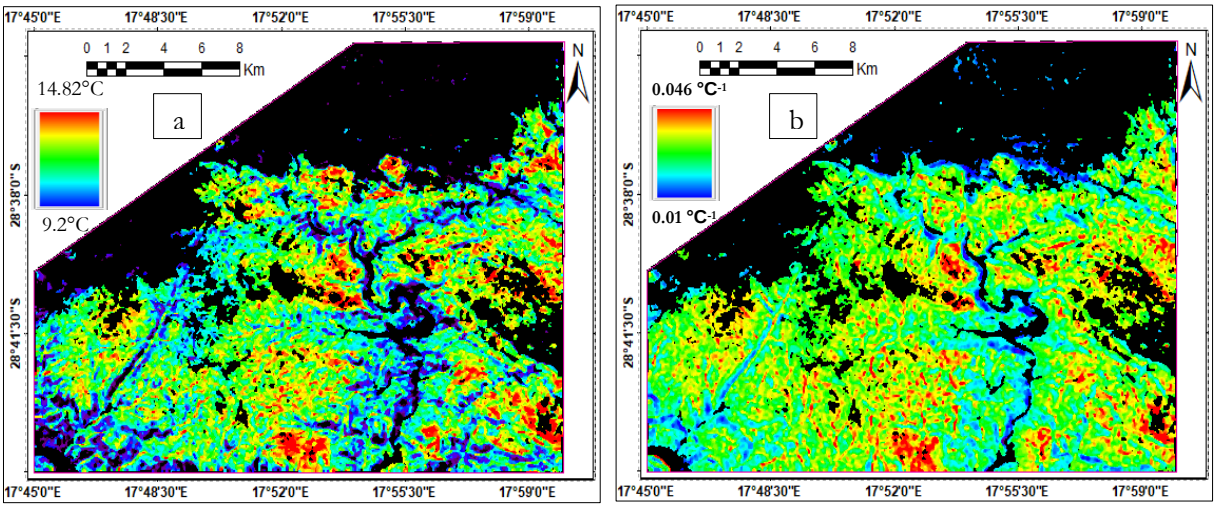

Figure 16 a) ASTER NST discriminated by using >6^0 slope angle range & linear stretching applied (9.2 - 14.82°C); b) ATI discriminated by using > 6^0 slope angle range & linear stretching applied (0.01 – 0.046°C^{-1})

5.4.1.1. Statistical analysis results of slope angle ranges versus ASTER NST and ATI

The discrimination of outcrops from unconsolidated cover was analyzed using the slope angle ranges as ROIs and statistical information from ASTER NST and ATI as shown below (see figure 17 a & b). The result appeared good for discriminating the outcrops from the unconsolidated cover. Specially slope angle range 0-4^0 was well separated from others. On the other hand, the mean values of 4-6^0 differ from the slope angle >6^0, but the discrimination was not significant due to overlapping. These results obtained were consistent both for ASTER NST and ATI.

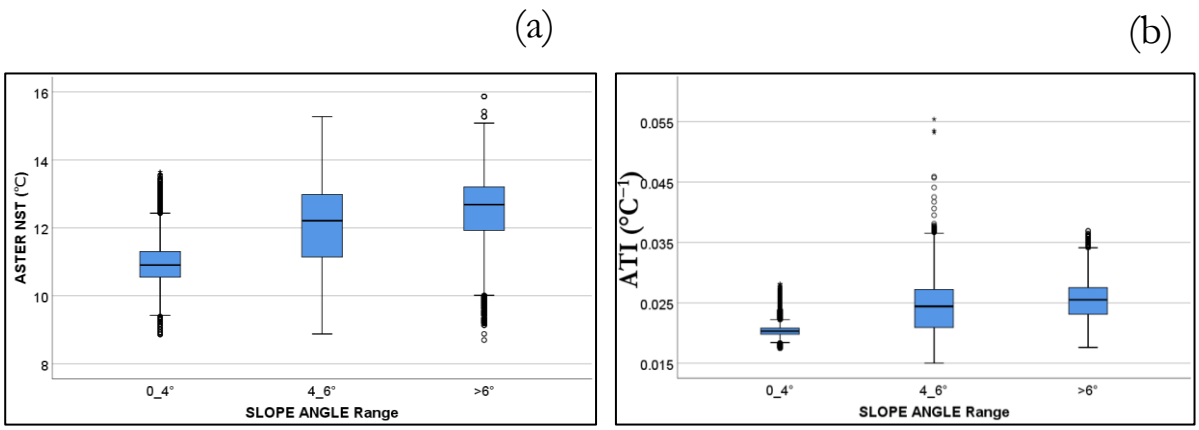

Figure 17 Slope angle ranges versus ASTER NST (a), and Slope angle ranges versus ATI (b) analytical result shows the distribution of ASTER NST & ATI between the ranges of slope angles.

5.4.2. ASTER NST and ATI ranging method results

Two ranges of values have been selected from the ASTER NST and ATI products respectively based on the method explained in chapter four subsection 4.3.2. The selected ranges were **ASTER NST range_1** (8.9 to 11.6 °C) and **ASTER NST range_2** (11.6 to 15.9 °C); and **ATI_range_1** (-0.073 to 0.022°C^{-1}) and **ATI_range_2** (0.022 to 0.061°C^{-1}). The ASTER NST range_1 and ATI_range_1 correspond with ***low*** surface temperature and apparent thermal inertia respectively (see figure 18 a and 19 a). On the other hand, ASTER NST range_2 and ATI_range_2 correspond with ***high*** surface temperature and apparent thermal inertia respectively (see figure 18 b and 19 b). The vector files of these ranges have been used to discriminate the outcrops from unconsolidated cover spatially for visual observation, and statistically evaluated to determine the level of difference in surface temperature and apparent thermal inertia between the ranges.

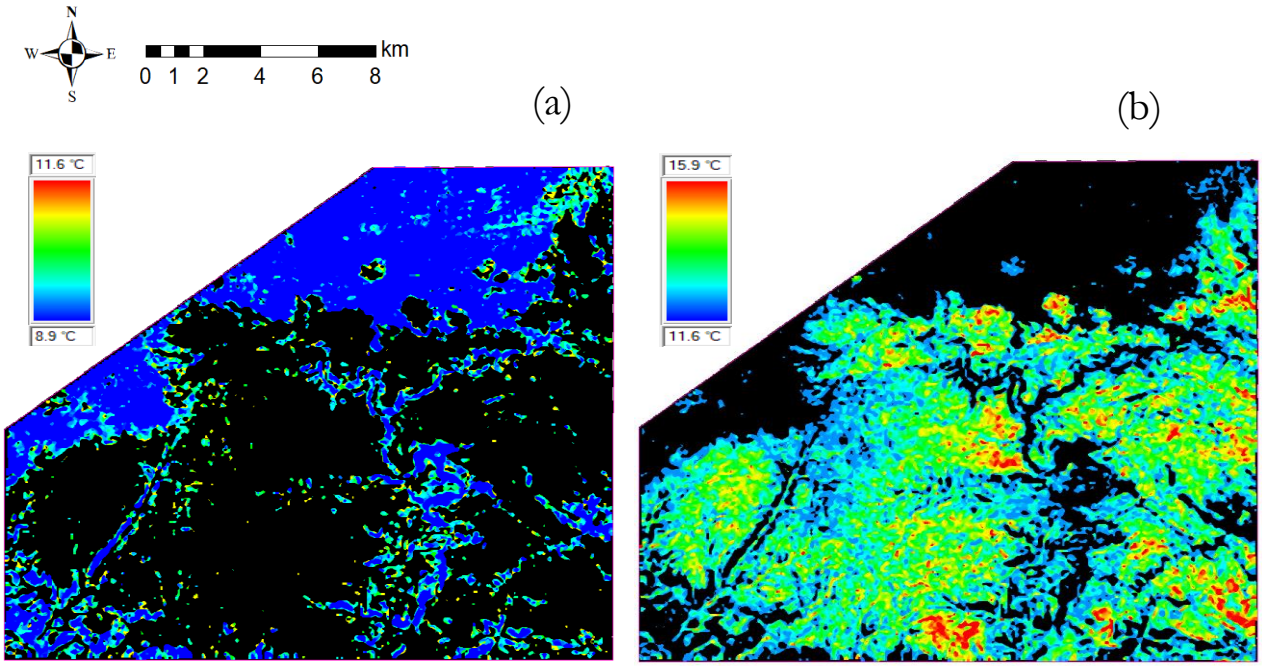

Figure 18 ASTER NST discriminated by ASTER NST range_1 (8.86 to 11.55 °C) (a); ASTER NST discriminated by ASTER NST range_2 (11.55 to 15.86 °C) (b).

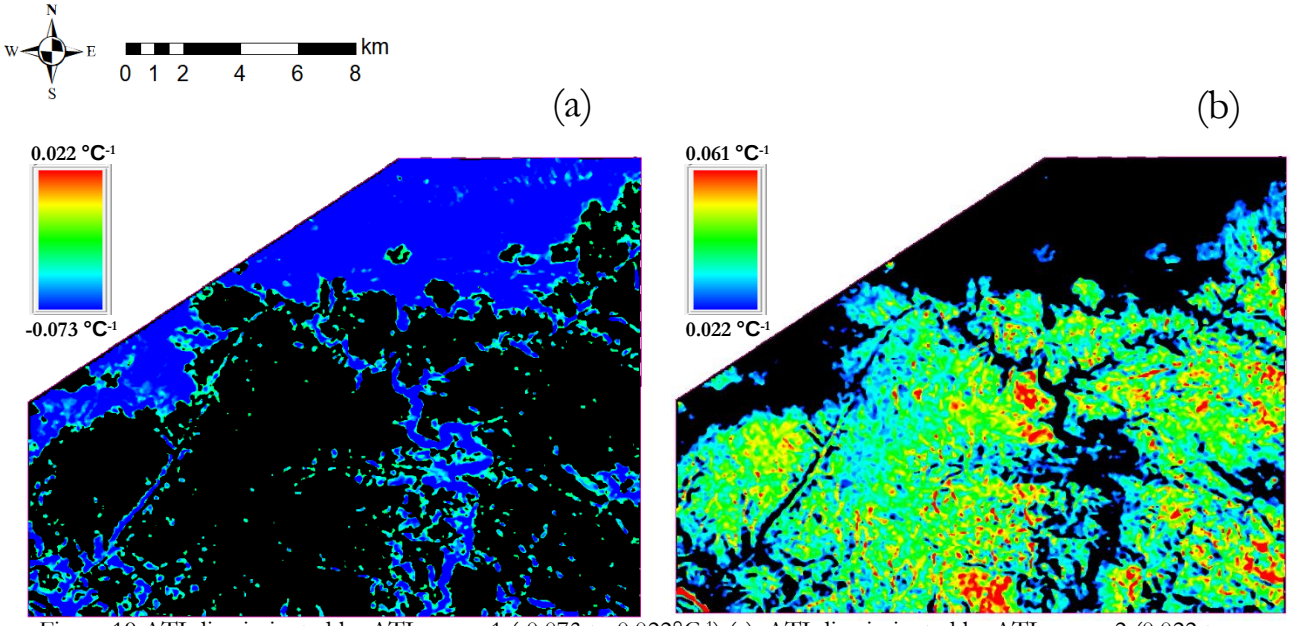

Figure 19 ATI discriminated by ATI range_1 (-0.073 to 0.022°C^{-1}) (a); ATI discriminated by ATI range_2 (0.022 to 0.061°C^{-1}) (b).

5.4.2.1 Statistical analysis results of ASTER NST and ATI ranges

The selected ASTER NST and ATI products have been analyzed statistically using box plots, and the results appeared good as their mean values are significantly separated as shown in figure 20 a and b. These clear differences between the mean surface temperature and ATI values inferred that the range of values (thresholds) could discriminate the outcrops from the unconsolidated cover.

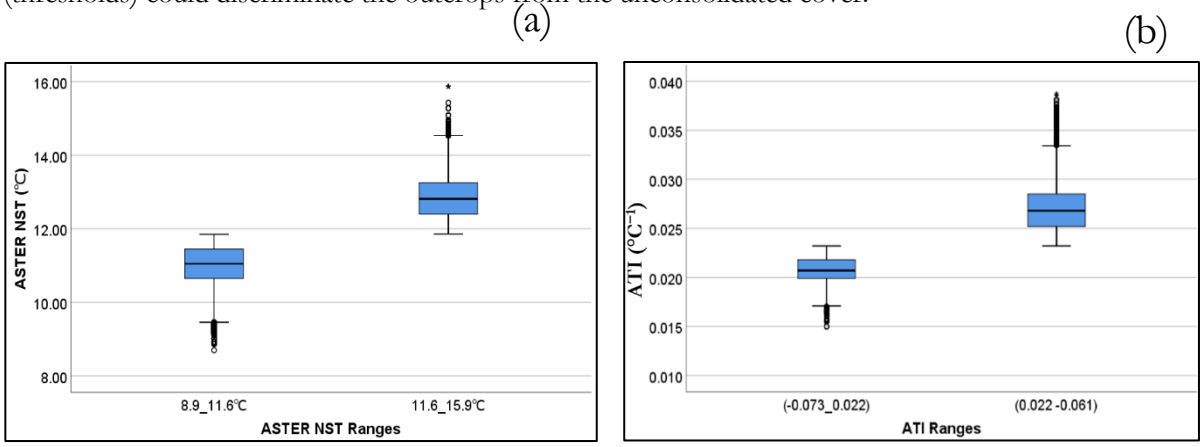

Figure 20 ASTER NST range_1 (8.9-11.6 °C) & ASTER NST range_2 (11.6-15.9 °C) (a); ATI range_1 (-0.073_0.022°C^{-1} & ATI range_2 (0.022 - 0.061°C^{-1}) (b) analytical results.

5.4.3. Quantitative interpretation

The discrimination of solid outcropping rocks from the unconsolidated cover materials was analyzed quantitatively using an ***overlay statistical analysis***. The overlay analysis was based on the ***intersection*** between the ***range of values*** developed for this purpose and the ***lithological unit vectors***. For the statistical analysis purpose, the geological map of Blignault (1972) was classified into outcrops and unconsolidated cover. The unconsolidated cover represented by the flat and gentle slope angles, ASTER NST range_1 and ATI range_1 could be discriminated from the outcrops that were represented by the steeper slope angle, ASTER NST range_2 and ATI range_2 respectively (see figure 21, 22 & 23). The overlay analysis results show that the slope angle ranges (0_4° & 4_6°) and slope angle range (>6°) have been ***intersected*** by ***91.43%*** and ***81.58%*** (see table 7), the ASTER NST range_1 and ASTER NST

range_2 have been intersected by ***83.58%*** and ***85.49%*** (see table 8), and the ATI range_1 and ATI range_2 have also been intersected by ***86.72 %*** and ***86.75 %*** (see table 9) with the classified ***unconsolidated cover*** and ***outcrops*** of the Blignault 1972 's lithological unit vectors respectively.

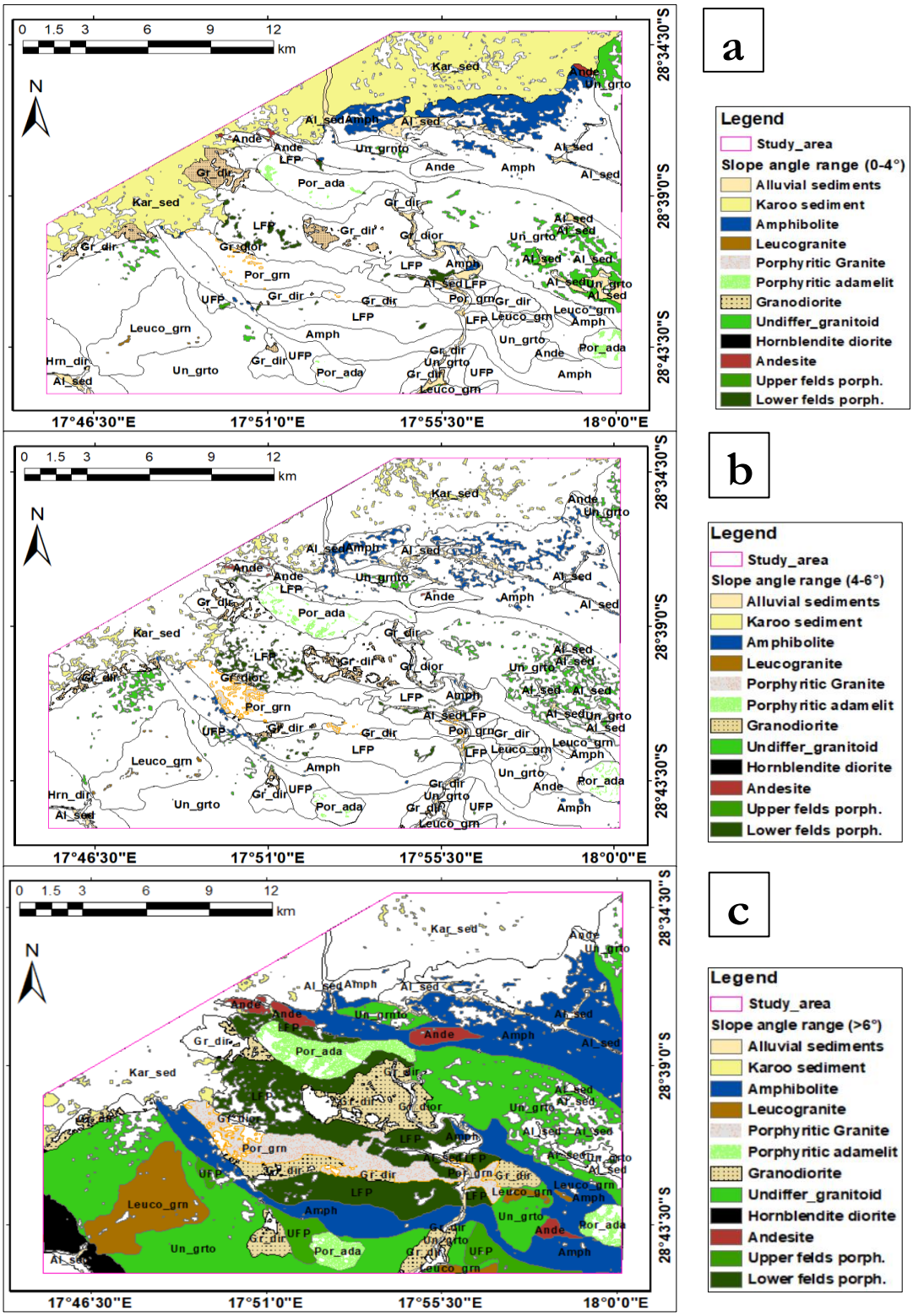

Figure 21 Overlay analysis results showing the intersection between lithological units & slope angle ranges **0_4°** (a), **4_6°** (b) & **>6°** (c) respectively.

Table 7 Summary of quantitative interpretation of the overlay analysis based on the intersection between the slope angle ranges and the classified outcrops & unconsolidated cover units of Blignault (1972)'s geological map.

	Unconsolidated cover	Outcrops	Total
Area of the classified lithological units in m²	85,402,925.00	326,490,523.00	411,893,448.00
Intersection of slope angle ranges (0_4° & 4_6°) in m²	78,086,738.49	58,115,951.66	136,202,690.14
percent of intersection of slope angle ranges (0_4° & 4_6°) & **unconsolidated cover**	**91.43%**		
Intersection of slope angle range (>6°) in m²	5,926,454.59	266,353,338.75	272,279,793.34
percent of intersect …….0ion of slope angle range >6° & **outcrops**		**81.58%**	

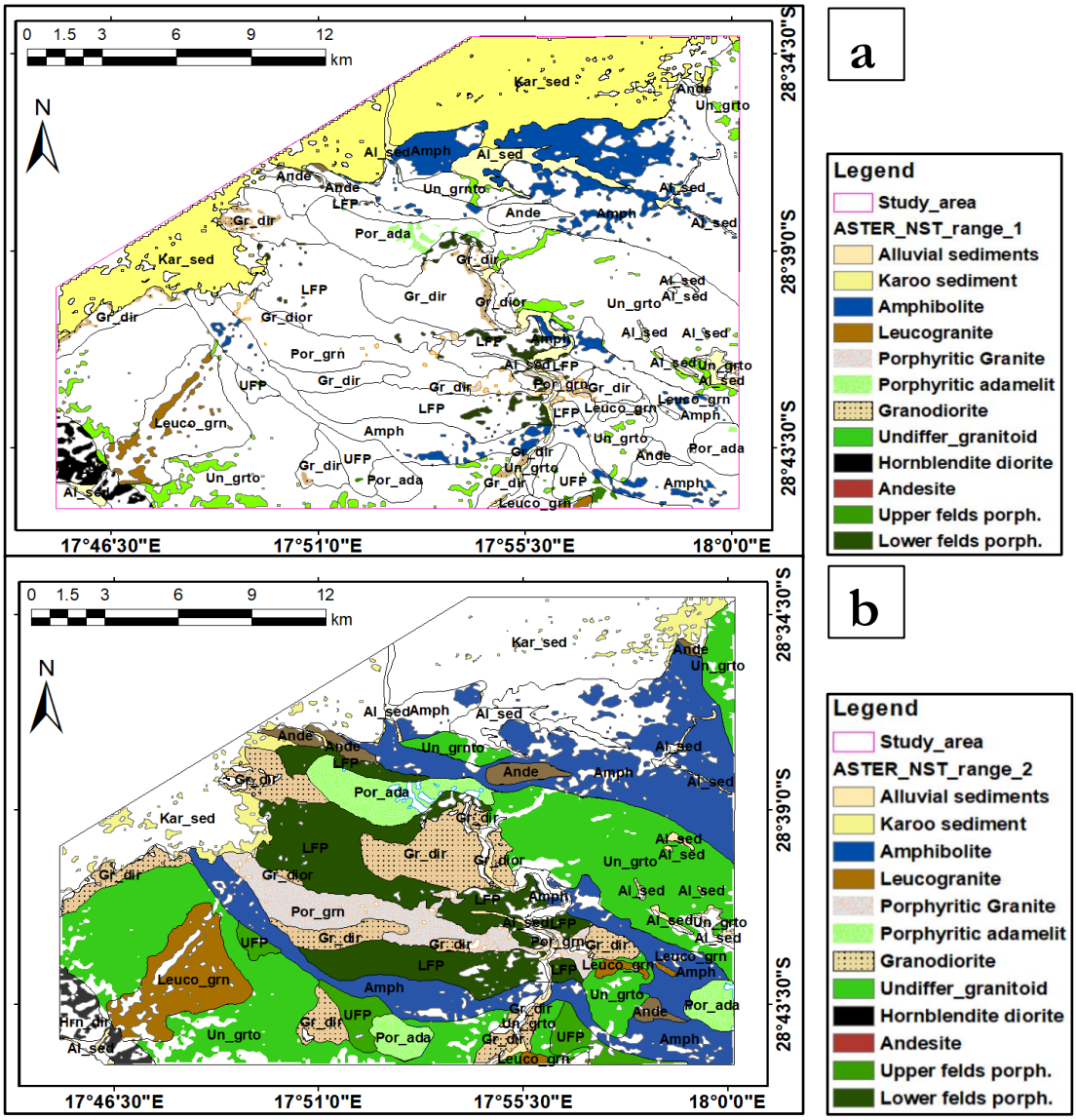

Figure 22 Overlay analysis result showing the intersection between lithological units & **ASTER NST range_1** (a) & **ASTER NST range_2** (b)

Table 8 Summary of quantitative interpretation of the overlay analysis based on the intersection between the ASTER NST ranges and the classified outcrops & unconsolidated cover units of Blignault (1972)'s geological map.

	Unconsolidated cover	Outcrops	Total
Area of the classified lithological units in m²	85,402,925.00	326,490,523.00	411,893,448.00
Intersection of ASTER NST_range_1 **(8.9°C_11.6°C)** in m²	71,381,459.90	47,557,116.92	118,938,576.82
Percent of intersection of ASTER NST_range_1 **(8.9°C_11.6°C)** & **unconsolidated cover**	**83.58%**		
Intersection of ASTER NST_range_2 **(11.6°C_15.9°C)** in m²	13,828,041.13	279,126,830.05	292,954,871.18
Percent of intersection of ASTER NST_range_2 **(11.6°C_15.9°C)** & **outcrops**		**85.49%**	

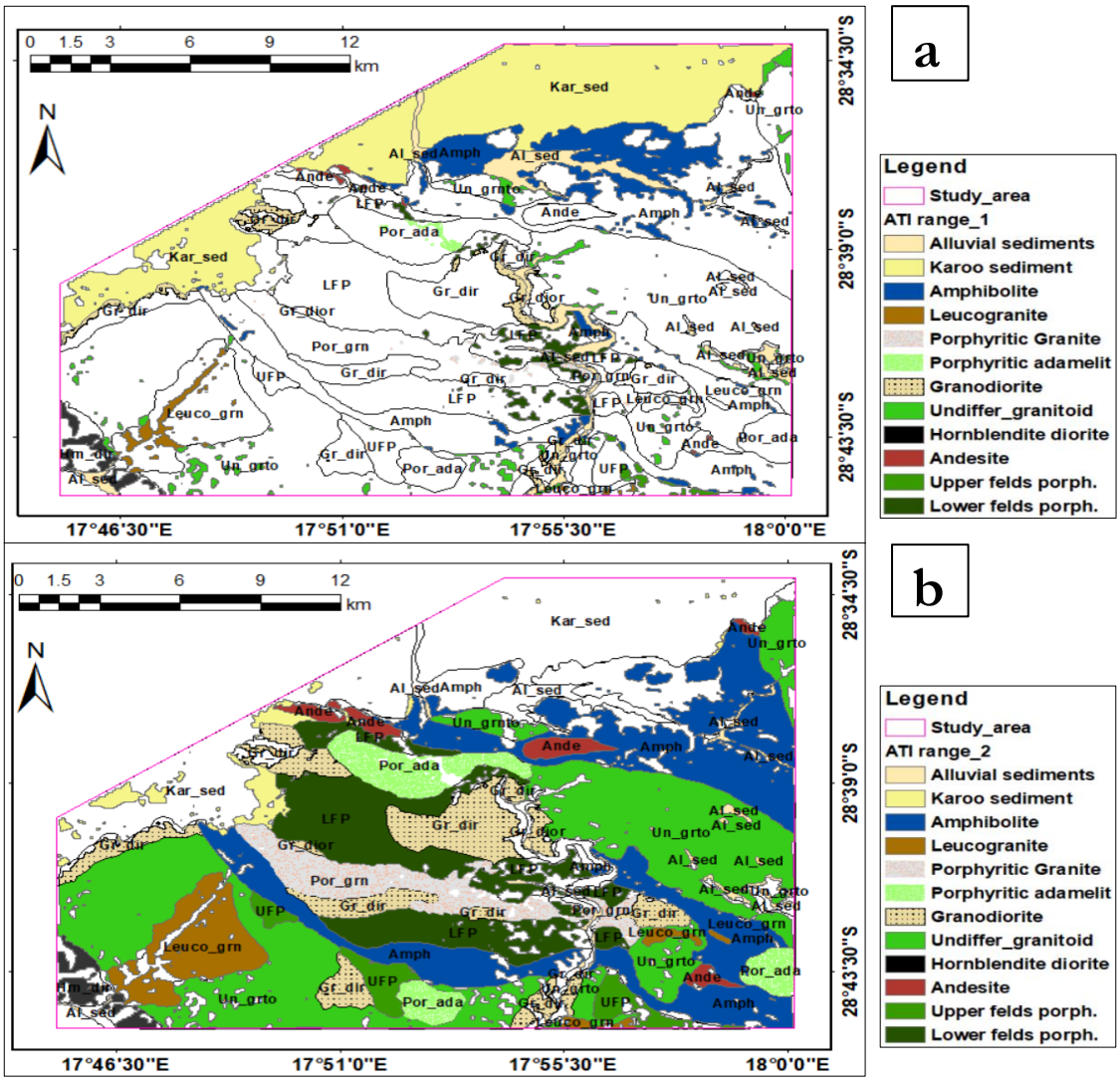

Figure 23 Overlay analysis result showing the intersection between lithological units & **ATI range_1** (a) & **ATI range_2** (b)

Table 9 Summary of quantitative interpretation of the overlay analysis based on the intersection between the ATI ranges and the classified outcrops & unconsolidated cover units of Blignault (1972)'s geological map.

	Unconsolidated cover	**Outcrops**	**Total**
Area of the classified lithological units in m^2	85,402,925.00	326,490,523.00	411,893,448.00
Intersection of ATI_range_1 **(-0.073_0.022**°C^{-1}**)** in m^2	74,063,953.50	44,016,994.08	118,080,947.58
Percent of intersection of ATI_range_1 **(-0.073_0.022**°C^{-1}**)** & **unconsolidated cover**	**86.72 %**		
Intersection of ATI_range_2 **(0.022_0.061**°C^{-1}**)** in m^2	10,594,488.36	283,218,012.05	293,812,500.42
Percent of intersection of ATI_range_2 **(0.022_0.061**°C^{-1}**)** & **outcrops**		**86.75 %**	

5.5. Results of geological structures detected by ATI, its potential evaluation, & integration with 1VD

5.5.1. Geological structures detection results of ATI

Lineaments were interpreted from the derived ATI based on their tone, texture, pattern and the past geological map of Haib (Blignault, 1972). The night-time surface temperature imageries were not useful for detecting structures. However, the apparent thermal inertia product has shown potential to identify structures. The distribution of lineaments detected by ATI image was less in the central and northern part, but more structures were detected in the eastern and western part of the study area (see figure 24). The shear zones appeared as deformed regions with darker stripes while the lineaments appeared as brighter and linear feature (see figure 24). The shear zones which were not mapped by the conventional method could be identified from the ATI.

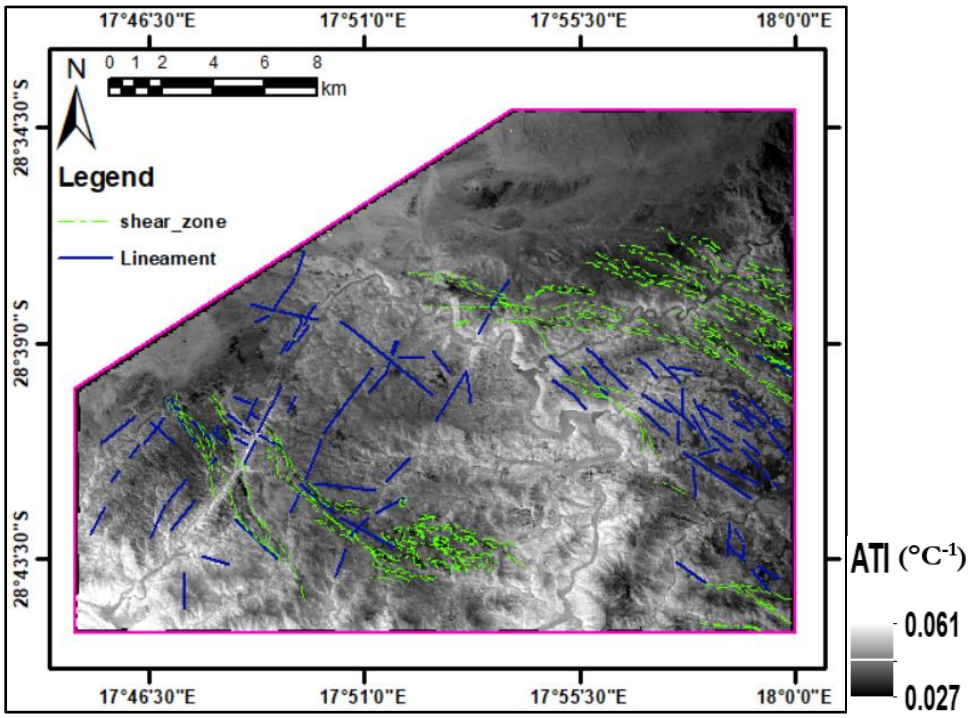

Figure 24 Lineaments and shear zones interpreted from ATI product.

In addition to lineaments, the derived ATI could be used to identify palaeochannels and sand dunes as illustrated below in figures 25 and 26 respectively. These were detected in the extreme northern part of the study area where the transported sediments are deposited. Interpretation of palaeochannels was supported with the drainage system of the study area that was derived from the 30m ground resolution DEM. These ancient channels buried in the recent sediments appeared in the ATI image as relatively brighter tone and doesn't coincide with the current drainages. Sand dunes which are shown as brighter linear features of NW-SE regional trend were best interpreted using WV-3 (panchromatic) data by zooming in to subpart of the study area (see appendix 7) and emissivity spectra of quartz (see appendix 8) from the inferred sand dunes also helps for confirmation.

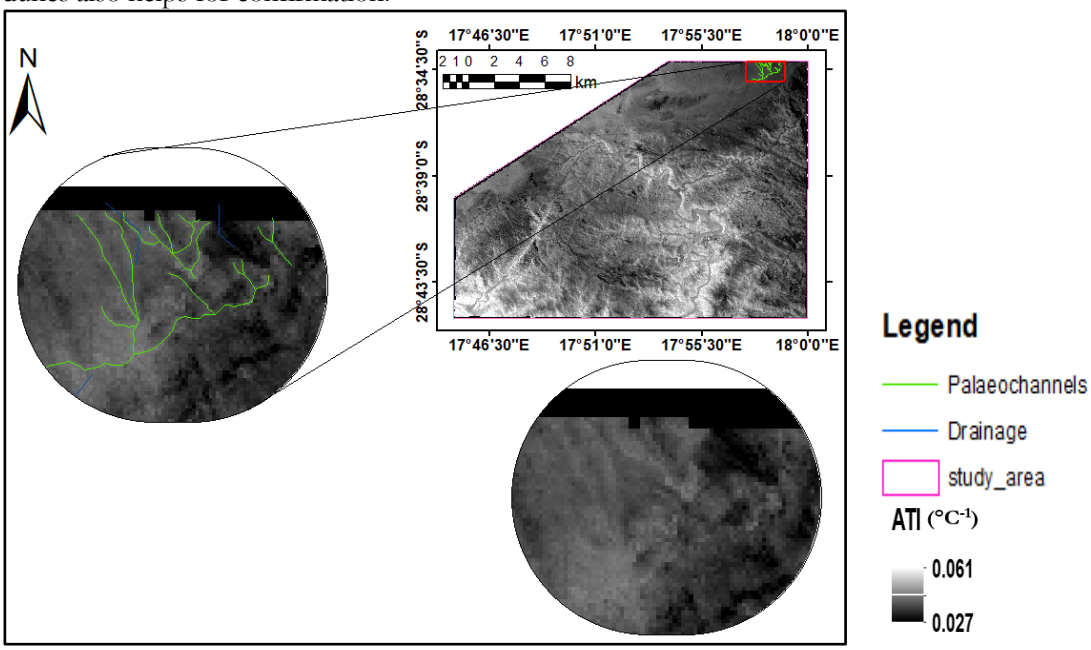

Figure 25 Palaeochannels inferred from ATI product.

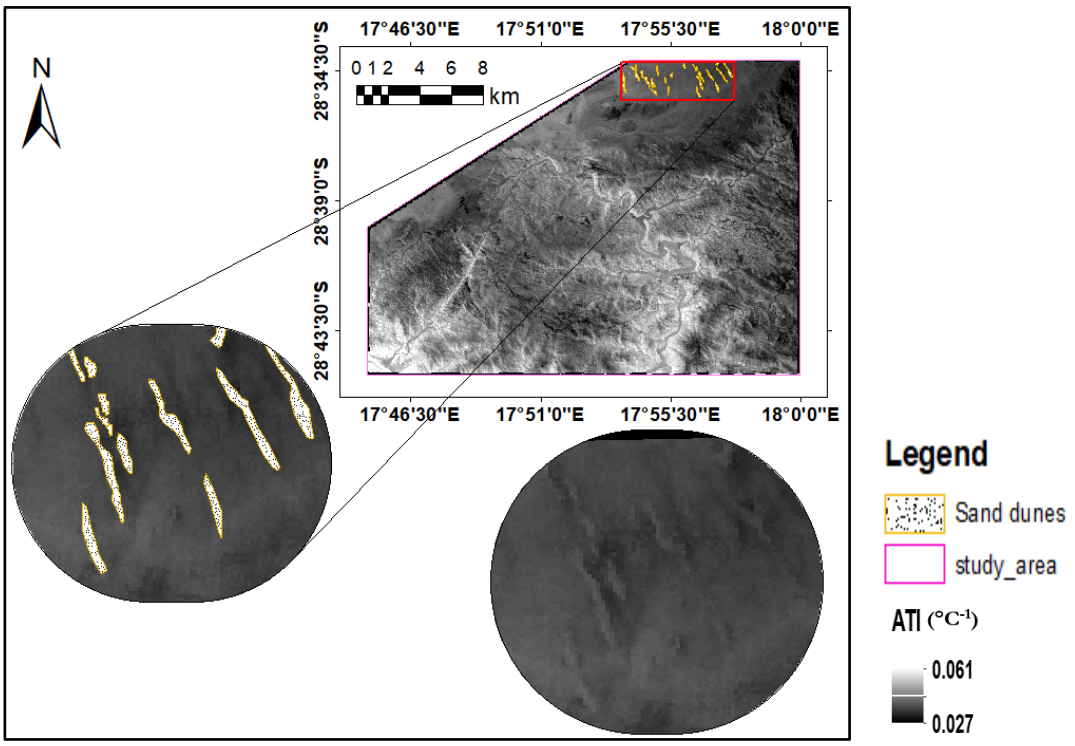

Figure 26 Sand dunes inferred from ATI product.

5.5.2. Evaluation of the potential of ATI to detect lineaments and the benefit of its integration with 1VD

Lineaments detected from the derived ATI were evaluated by comparing with the lineaments detected by the calculated 1VD of the airborne magnetic data to determine its potential to identify lineaments since magnetics is more reliable method for geological structures. The geological map of Haib was also used to interpret the lineaments and to check its correspondence with ATI related to structures. The lineaments identified from both ATI and 1VD have been integrated using the GIS integrate tool in order to evaluate the benefit of ***integration*** of the results of the two methods. The results of each of the methods and the integration are presented in the following subsections.

5.5.2.1. Result of lineaments interpreted from 1VD of airborne magnetic data for evaluation

The areal coverage of the total magnetic intensity (TMI) of the airborne magnetic data was smaller than that of the ATI; however, it was used to calculate 1VD to interpret lineaments as presented below as grey scale. The detected lineaments were overlain with it as illustrated in figure 27. The lineaments identified from the 1VD of the airborne magnetic data was used to evaluate the potential of ATI using ArcMap. The area of ATI was resized to that of magnetic area size for comparison.

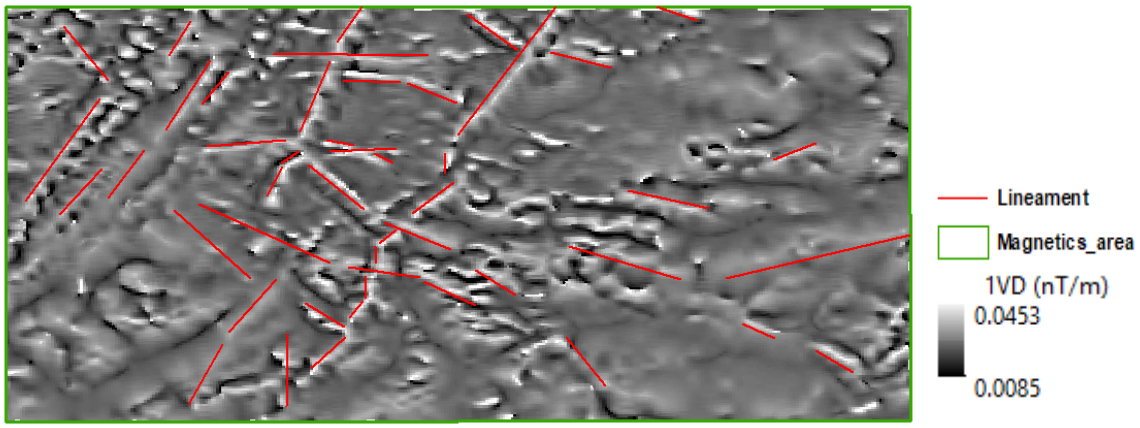

Figure 27 The 1VD calculated from the reduced to pole (RTP) airborne magnetic data and the interpreted lineaments overlain with it. See figure 1 to relate this subset area map with the total study area

5.5.2.2. Evaluation and integration of the lineaments detected by ATI with 1VD

Lineaments were interpreted from ATI based on the visual image interpretation techniques and using the existing geological map of Haib (Blignault, 1972). Some of the lineaments have been coincident with the geological map, but in general, ATI could detect more lineaments when it was compared with the published map (see figure 28 a). The potential of ATI was evaluated by comparing with the lineaments identified from the 1VD by overlaying in ArcMap. Some of the lineaments were coinciding and aligned in the fewer gap with 1VD; the rest were far apart. The lineaments detected from each method were integrated using ArcMap integrate tool. The lineaments which were close to each other within the range of the chosen tolerance were automatically snapped to the 1VD lineaments while the rest apart more than the tolerance remained apart in the integrated lineament map (see figure 28 d).

The total length of Lineaments calculated from the ***integrated*** ATI and 1VD was ***74.42 km***. On the other hand, the total length of the lineaments identified using 1VD and ATI was 57.41 km and 30.01km respectively (see figure 28 b & c). However, 13.02 km lineaments could be identified commonly from both. Hence, the lineaments were calculated and 77.14% and 40.32% were identified from 1VD and ATI respectively, and 17.49% were identified from both in common. This result showed that the magnetic data identified more lineaments as compared to ATI. The lineaments identified from each method, and the integration result is illustrated in figure 28.

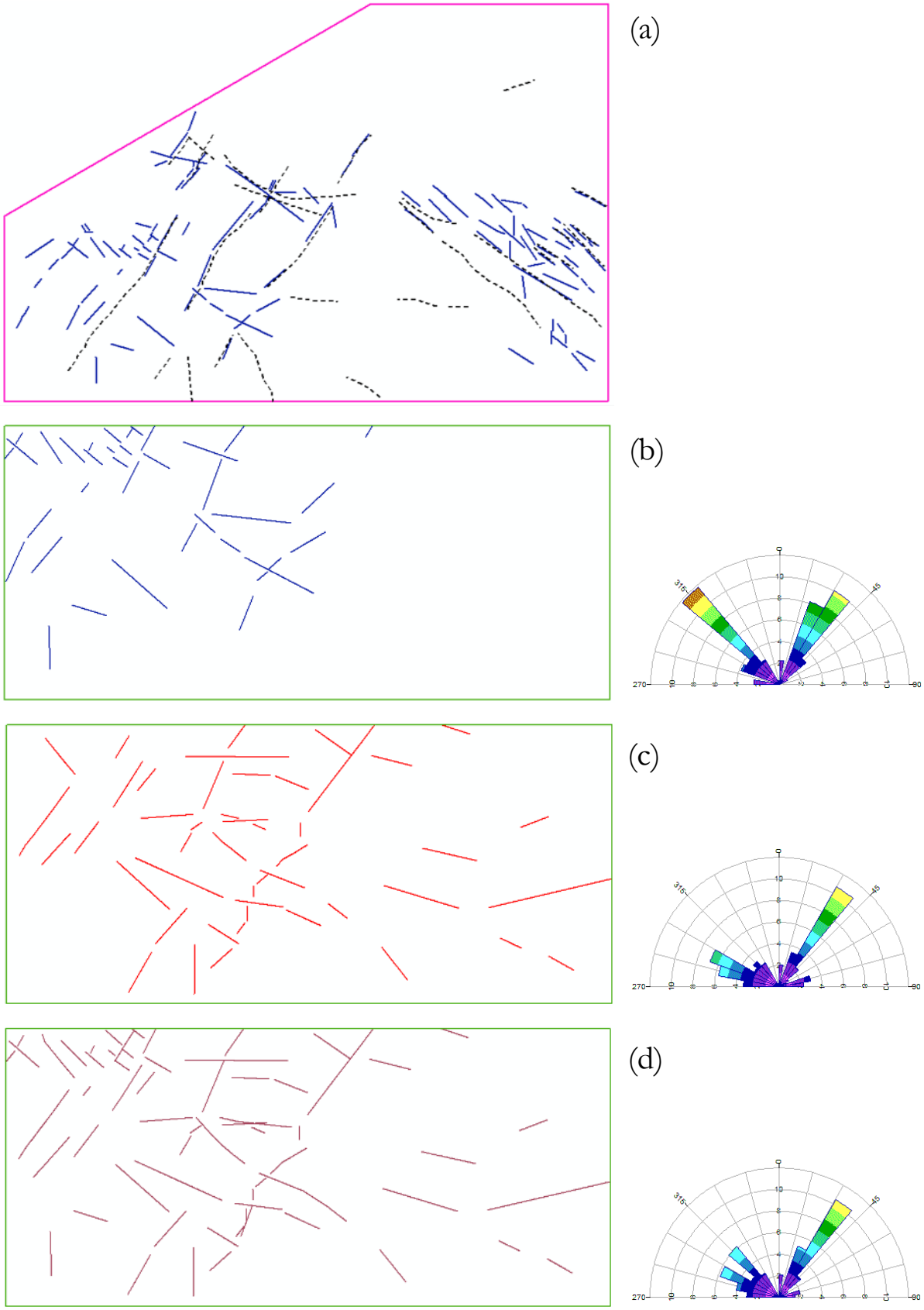

Figure 28 Evaluation and integration results of lineaments. (a) the lineaments of the geological map of Haib (broken lines) & ATI (solid lines) for checking; (b) lineaments interpreted from ATI; (c) lineaments interpreted from 1VD; and (d) integration of lineaments of ATI & 1VD. The rose diagrams showing the NE-SW and NW-SE trending geological structures. See figure 1 to relate these subset area maps with the total study area

5.6. Results of the effect of vegetation on discriminating the outcrops from unconsolidated cover

The effect of green vegetation on the discrimination of outcrops from unconsolidated cover has been analyzed by using the calculated NDVI and the ASTER NST products acquired from different seasons. The difference in the vegetation density between the two seasons has been observed (see figure 29 a & b). This difference was also clearly observed from the statistical analysis using the ROI's that were selected from the inferred outcropping and unconsolidated cover of the imageries of the respective seasons.

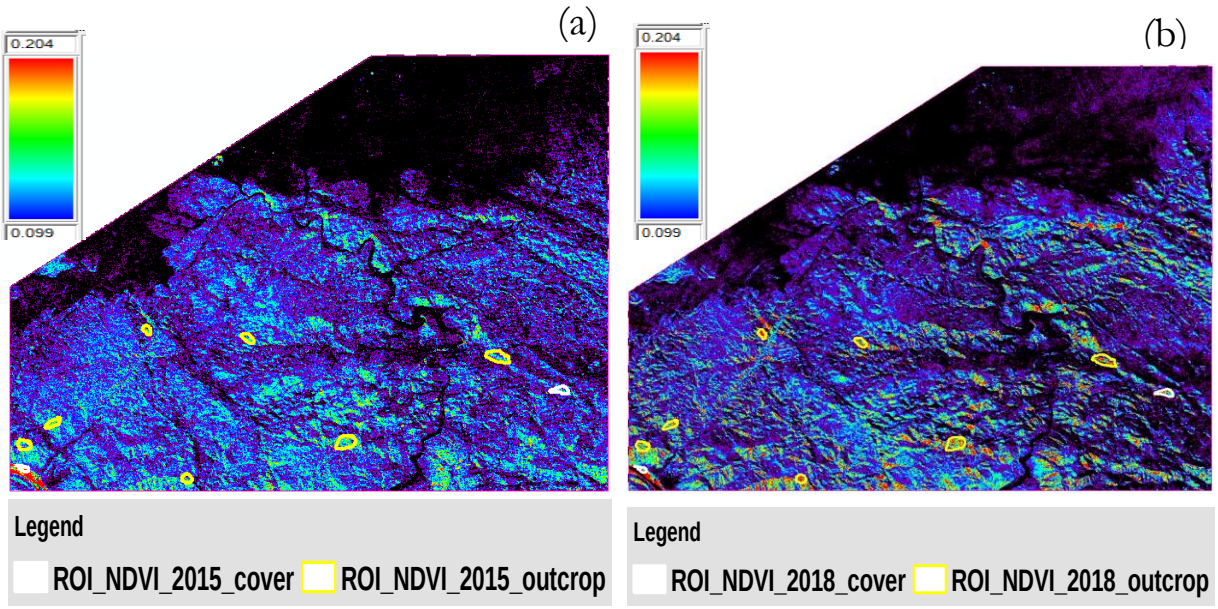

Figure 29 The calculated NDVI from the 2015-less vegetated (a); and the calculated NDVI from the 2018 - moderately vegetated seasons acquired imageries.

The effect of green vegetation on the discrimination of outcrops from unconsolidated cover have been analyzed using the method described in chapter four, section 4.1.2. The NDVI value of the moderate vegetated season (2018) was relatively higher than the less vegetation season (2015) as shown below. These values were consistent both on the inferred outcrops and unconsolidated cover (see figure 30 a and b).

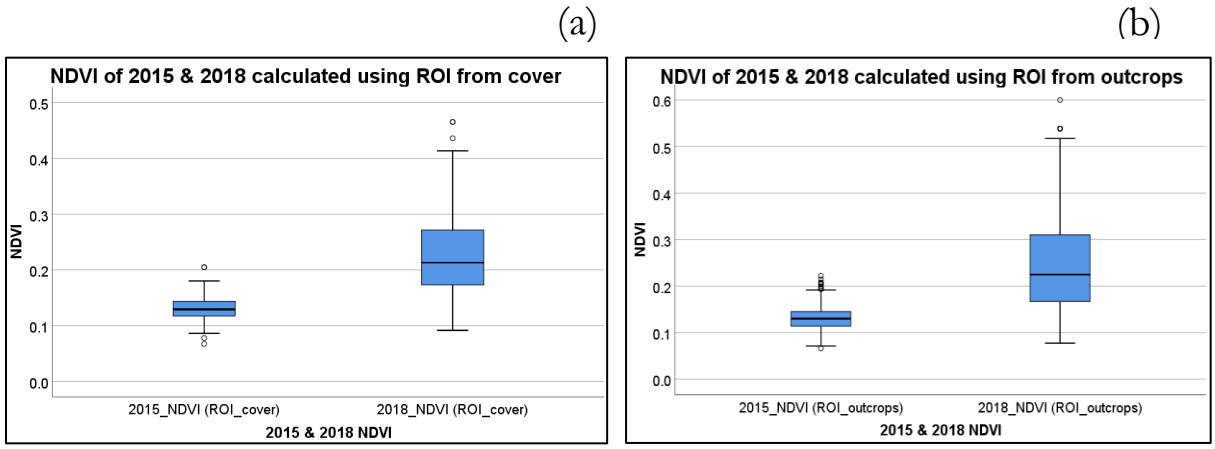

Figure 30 The boxplot showing the difference in NDVI between the 2015 and 2018 less vegetated and moderately vegetated seasons respectively. Analysis result using ROI that were selected from the inferred outcropping area (a); and ROI were selected from the inferred unconsolidated area (b) respectively.

The relationship between surface temperature, apparent thermal inertia and NDVI have been established using ***correlation analysis***. And the results show that surface temperature was negatively correlated

whereas, apparent thermal inertia was positively correlated with NDVI respectively as it is illustrated on table 10; however, the correlation is not that strong.

Table 10 Correlation matrix between ASTER NST, ATI and NDVI of the less vegetated and moderately vegetated seasons

Correlations						
	2015_nST	**2015_ATI**	**2015_NDVI**	**2018_nST**	**2018_ATI**	**2018_NDVI**
2015_nST	1	.233**	-.295**	.735**	.288**	-.333**
2015_ATI	.233**	1	.372**	.176**	.371**	.142**
2015_NDVI	-.295**	.372**	1	-.295**	.110**	.366**
2018_nST	.735**	.176**	-.295**	1	.344**	-.366**
2018_ATI	.288**	.371**	.110**	.344**	1	.200**
2018_NDVI	-.333**	.142**	.366**	-.366**	.200**	1

**. Correlation is significant at the 0.01 level (2-tailed).

The effect on the discrimination of the outcrops from unconsolidated cover due to the green vegetation cover in 2018 has been observed. As it is shown in figure 31 a and b, the **mean** values of the surface temperature between the ROI's from the inferred outcrops and unconsolidated cover of the less vegetated period ***have been separated significantly*** and discrimination in this case was possible (see figure 31 a). On the other hand, the **mean surface temperature** values between the ROI's from the inferred outcrops and unconsolidated cover of the moderately vegetated period ***has been separated slightly*** and showed much overlap that indicated the difficulty of discrimination (see figure 31 b).

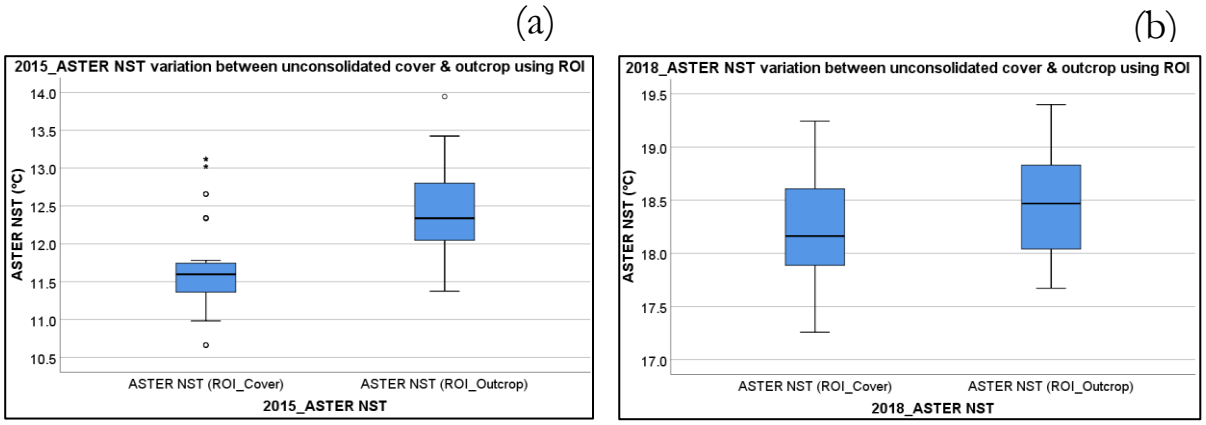

Figure 31 The boxplot showing a clear difference in the mean ASTER NST values between the inferred unconsolidated cover and outcrops in 2015 of the less vegetated season (a); and the less difference in the mean of ASTER NST values between the inferred unconsolidated cover and outcrops in 2018 of the moderately vegetated season (b).

6. DISCUSSION

The capability of ASTER NST and ATI to discriminate the outcrops from unconsolidated cover has not yet been quantitatively determined previously, though determining its potential is relevant for geological applications. A method to discriminate the outcrops from unconsolidated cover was required to be developed for quantitative interpretation. So that, ***the range of values*** such as slope angle ranges, ASTER NST ranges and ATI ranges from the slope map, ASTER NST, and ATI respectively were established in this study in order to represent the outcrops and unconsolidated cover units (see chapter 5, section 5.4). Hence, these ranges of values could be considered as ***threshold*s** and used to spatially discriminate the outcrops from unconsolidated cover for visual observation. Hence, an overlay analysis was conducted between the ranges of values and the lithological unit vectors.

Following the establishment of the range of values that were used to represent the outcropping and unconsolidated landforms in this study, an overlay (intersection) analysis was conducted for the ***quantitative*** interpretation using these range of values and the lithological unit vectors (see chapter 5, section 5.4.3). The geological map of the study area, that was produced by Blignault (1972) was assumed to be the ***reference*** control for the overlay analysis. Therefore, the intersection result showed, the ***unconsolidated cover*** vectors of the lithological map were intersected by ***91.43%***, ***83.58%*** & ***86.72%*** with the representative ranges of values respectively. On the other hand, the ***outcropping unit vectors*** of the same lithological map were also intersected by ***81.58%***, ***95.28%*** & ***96.39%*** respectively with the representative ranges of values. These results show the usefulness of the method applied and the potential of ASTER NST and ATI to discriminate the outcrops from unconsolidated cover. The methods used in this study could discriminate with almost comparable potential as compared to each other. But the ATI ranging method was slightly better than the others in comparison since it is more related to physical properties, and less noise that makes the selection of ranges clearer when overlain with other datasets.

In the case of slope angle range method, the slope angle (0-4^0) represents the ***plain*** covered with ***alluvial and colluvial materials***. The slope angle (4-6^0) represents the ***gentle slope*** where colluvial materials can lay at the base of steeper cliffs and those above 6^0 stands for the ***steeper solid outcrops*** as topography in particular slope is related to landform ("Geomorphology of slopes," n.d.). On the other hand, in the case of ASTER NST and ATI range methods, the selection of the ranges was based on the drastic change in the observed ASTER NST/ATI values between the boundaries of lithological units due to the difference in their physical properties such as thermal conductivity, density, and specific heat (Ramakrishnan., 2013; Xue & Cracknell, 1995). Discrimination between different rocks could be possible if their physical properties differ significantly, for example, the denser rocks and lighter cover materials have significant different heating and cooling capacity (Watson, 1975), and this was observed between the alluvial sediments and the other solid rocks in this study. In particular, differences in thermal response were observed between the alluvial/colluvial sediments and the solid/denser intrusive igneous rocks. The discrimination of outcrops from cover was qualitatively tested by Hewson et al. (2017) using night-time ASTER surface temperature, and it agrees with this study; however, the discrimination in this study is interpreted quantitatively.

The thermal physical properties of igneous and metamorphic rocks are nearly similar to each other and discrimination is difficult (Gupta, 2003) (see table 4). So, the discrimination between the outcrops in the study area was difficult as they are dominantly igneous rocks. on the other hand, the thermal inertia values of the unconsolidated cover of the study area were lower as compared with any of the outcropping solid rocks due to the significant difference in thermal physical properties (e.g. density, thermal conductivity &

specific heat) between them, and this allows discrimination to be possible. The trend of the ATI values of the lithological units in this study was similar to the actual thermal inertia as compared with other studies. For example, the mean of ATI values of alluvial cover and granite rocks in this study were 0.020°C^{-1} and 0.038°C^{-1} respectively; and the thermal inertia values from literature by Nasipuri et al., (2005) and Gupta (2003) were 0.042–0.024 cal cm^{-2} $s^{-½}$ °C^{-1} and 0.052 cal cm^{-2} $s^{-½}$ °C^{-1} respectively for those lithological units. Water has higher ATI than dry soils and rocks because of the low diurnal temperature difference (Kuenzer & Dech, 2013), this was observed at a pixel location of ***769606.88 E/ 6816764.52 S*** at the Orange River in this study. The high ATI value of water was also stated by Ramakrishnan et al. (2013) based on the result conducted somewhere else. In this study, some thermally anomalous spots within the inferred unconsolidated cover have been observed from ASTER NST and ATI products, and the cause of these anomalies is estimated to be either shallow depth buried/subsurface bedrocks or underground water source; however, it needs further research for confirmation (see appendix 17).

The methods developed in this study for the discrimination were specifically for Haib, but they can be used at least in similar terrains using the same ranges of values; however, the possibility of making erroneous interpretation should be considered. For example, the slope angle range (0-4^0) values may not necessarily represent the actual unconsolidated alluvial cover specifically in the case of sedimentary flat terrains where alluvial cover might not be there, but they could be interpreted as cover due to their flat topography and lower density/higher porosity. So that, some of the sedimentary rocks that are not actually unconsolidated cover might lead to wrong interpretation. In addition to that, the gentle slope angle (4-6^0) may not sometimes refer to colluvial materials, which could be normally deposited at the base of the cliffs by gravity. But due to intensive erosion/flooding that is common in the desert areas and that can be the driving force for transportation of these colluvial materials to the flat flood plains. The ASTER NST and ATI range methods can also be interpreted wrongly. For example, hornblendite diorite (as interpreted by Blignault (1972)) appeared with low surface temperature and ATI values like unconsolidated cover materials. As a result, it was interpreted erroneously as unconsolidated cover (see figure 12 a & b), but the low thermal value of hornblendite diorite could be due to intensive weathering on its surface, and targeted field validation ("ground truthing") would assist.

ASTER data has been well studied for lithological and mineralogical mapping applications; however, the papers on the structural mapping using ASTER are few (Papadaki et al., 2011). A study into the capability of ASTER thermal products for detection of geological structures and the benefit of their integration with airborne magnetics would be useful (Hewson et al,. 2017). So that, the capability of ATI to detect lineaments has been evaluated in this study using 1VD because magnetic data is reliable for subsurface structural mapping since it is not affected by atmospheric issues and surface distortions (Saada, 2016). The lineaments interpreted manually from the suitable thresholds and minimum length defined ATI and 1VD products were overlain in ArcMap and the total length of the lineaments from each of them was calculated for comparison. As a result, the length of lineaments interpreted from ATI and 1VD were ***30.01 km*** and **57.41 km** respectively. However, ***13.02 km*** lineaments could be identified in common both from ATI and 1VD. The lineaments that are identified from each method were integrated using an Integrate Tool in ArcGIS with a defined ***tolerance*** value to snap the nearby lineaments automatically to the 1VD which was chosen as a reference. So that, the total integrated lineaments that were interpreted from both methods were ***74.42 km***. Therefore, the 1VD could identify 77.14%, the ATI product could identify 40.32 % and 17.49 % could be identified by both methods in common from the total integrated lineaments.

In this study, ASTER derived ATI has been used and various structures such as lineaments, shear zones, palaeochannels and sand dunes could be interpreted (see figure 24 to 26). The tectonic setup of the study area is characterized by the regional NW-SE and NE-SW trending Orange River Orogeny and Namaqua

Orogeny compressional forces respectively, which were responsible for the formation of geological structures of Haib (Macey et al., 2017). The Namaqua Orogeny is the younger episode tectonic force which is characterized by cross-cutting of the older structures (Macey et al., 2017), and such cross-cutting relationships are observed in this study. Lineaments (which could be faults, dikes, shear zones, etc.,) were interpreted from the derived ATI image based on their tone, texture and pattern of linear features. The linear features only larger than 250m in length and ATI value above 0.027°C^{-1} anomalous values have been considered as lineaments in order to avoid confusion with the 1st order streams and to consider only the clear ones. The ASTER NST could not detect structures clearly as compared to ATI. This could be that ATI considers albedo and the temperature differences in the calculation to be more related to physical properties (density, thermal conductivity) than ASTER NST; and the effect of image acquisition time, which the ASTER NST used for this study was acquired at 21:00 local time. This acquisition time could be closer to the thermal crossover where the difference in radiant temperature between various geological materials is less and discrimination could be difficult (Gupta, 2003). For consistency and clarity of interpretation, anomalous linear features above 0.008 nT/m gradient were considered as lineaments from 1VD. The detection of structures by thermal imageries could be due to the difference in thermal physical properties and the moisture contents between the boundaries of the bedrocks and sediments filled/weathering within the fractures or dikes. The structures along the fault plane can be appeared clearly as darker features in the day and night-time thermal imageries when spring or groundwater is moisturizing the boundary plane (Papadaki et al., 2011). In this study, structures appeared as a brighter tone in the ATI image due to either the moisture content along the fracture zone or the possible denser intrusions such as dikes.

Moreover, features of darker with few brighter stripes and deformed appearance have also been detected from ATI and interpreted as shear zones (see figure 24). On the other hand, detection of lineaments from airborne magnetic (1VD) could be due to the difference in the vertical gradient magnetic field strength at the ***edge*** of the bedrocks and sediments (Oha et al., 2016). The variations in the physical properties (density, thermal conductivity, specific heat, porosity, etc.,), moisture content, magnetic susceptibility, spatial resolution and depth of structures could be the reason for the difference in the capability of structural detection between the two methods. The detection of lineaments using ATI derived from NOAA thermal data was tested, and the result shows that some structures were identified but not so clear due to the low resolution (Mitra & Majumdar, 2010). These results show the improved spatial resolution of ASTER TIR imagery at 90 meters shows improvements. In addition to that, several authors have studied the possibility of lineament identification using the multispectral images of ASTER and Landsat bands with image enhancement techniques such as Principal Component Analysis (PCA) (El-Magd et al., 2015; Hung et al., 2005; Papadaki et al., 2011). The thermal imageries which can generate the subsurface information nearly from the depth of 1m (Gupta, 2003) and further processing to ATI could be also supplementary to the daytime image structural interpretation.

Palaeochannels, which are ancient channels covered with recent sediments, can be detected using magnetics due to the accumulation of magnetic minerals such as maghemite and magnetite (Mackey et al., 2000b). Hewson et al. (2017) attempted the application of ASTER NST and ATI in conjunction with aeromagnetics, to identify palaeochannels and found some preliminary positive results; however, it could not be widely applied due to lack of ASTER day and night data pairs. The magnetic data of this study doesn't overlie where palaeochannels were suggested from ATI products. So that, interpretation was only based on the current drainage map generated from SRTM DEM. In general, the capability of ATI was less successful for sub surface mapping than 1VD, that could be due to the difference in spatial resolution and the capability of the magnetic data to identify deep-seated structures. However, ATI appears to be useful

as supplementary data, and the integration of the results of the two methods has a benefit to delineate additional more structures than individually.

The negative correlation between the NDVI and the surface temperature due to evapotranspiration process has been established by other researchers using NDVI; however; the effect of the green vegetation on discriminating outcrops from unconsolidated cover has not been published. So that, in this study the effect has been analyzed using ROIs from the inferred outcrops and unconsolidated cover using imageries acquired in the less vegetated and moderately vegetated seasons. The analyses result show that the ***mean*** night-time surface temperature difference between the outcrops and unconsolidated cover is ***higher*** in the less vegetated season whereas, this difference is ***lower*** during the relatively vegetated period as clearly shown on the analyses results (see figure 31 a and b). The correlation between ASTER NST, ATI and NDVI were carried out, and the negative relationship of vegetation with surface temperature was observed, and this result is agreed with the previously conducted researches elsewhere by Ayanlade (2016); Hewson et al. (2017) and Kawashima (1994) (see table 10).

The cooling effect of green vegetation on the land surface temperature is due to direct shading and indirect evapotranspiration process (Alavipanah et al., 2015). The plant canopy acts as a shade and prevents the heating of the land surface (Zou et al., 2019) and that ***reduces*** the heat that could be absorbed during the daytime by the outcrops and unconsolidated cover. Evapotranspiration process also reduces the surface temperature since plants absorb the heat from the atmosphere and transmit that into air in the form of vapor supported by wind (Liu et al., 2019; Zou et al., 2019). Hence, the green vegetation ***reduces and regulates*** the surface temperature (see table 10; & figure 31 a & b), and that causes difficulty of the discrimination of outcrops from unconsolidated cover. The reduction of the surface temperature was manifested with ***-0.366*** correlation between the ASTER NST and NDVI imageries acquired at the more vegetative season of the year 2018; and this correlation was ***-0.295*** for the imagery acquired at the less vegetated season of the year 2015. Further studies with greater night-time TIR acquisitions from different seasons would be useful to confirm these results. This effect of vegetation could be even more if the vegetation coverage of the study area at the time of image acquisition were higher. The cooling extent of vegetation on the land surface temperature is dependent on the type and density of vegetation, however; 2 to 8 °C reduction of surface temperature was reported elsewhere by Taha et al. (1989). The availability of ASTER night-time surface temperature was limited within the study area and that limits the analysis to be done only for two seasons.

7. CONCLUSION AND RECOMMENDATION

7.1. Conclusion

Based on the results of the analyses made to achieve the objectives of this research, the following conclusions are drawn and presented together with the research question:

1. **Can the ASTER NST and ATI products be used to discriminate outcrops from unconsolidated cover within the study area potentially? And is it possible to determine the potential of ASTER NST & ATI quantitatively by developing a method?**

The overlay analyses result inferred the potential of the slope angle, ASTER NST and ATI ***ranging methods***, which were developed in this study to conduct quantitative interpretation. So that, ASTER NST and ATI products can be used to discriminate outcrops from unconsolidated cover potentially; and their ***potential*** have been ***quantitatively*** determined which in the previous studies interpretation was only possible qualitatively. The methods applied to discriminate the outcrops from unconsolidated cover can be used at least for similar terrains, and it can have a relevant geological application such as pre-field sample site selection for geochemical analysis in mineral exploration activities. Such knowledge may also assist the relating of geochemical soil anomalies to either shallow outcropping or transported cover materials.

2. **How comparable is the capability of ASTER NST and ATI to detect structures (e.g. lineaments & palaeochannels) as compared to airborne magnetics? And what is the benefit of integrating the results of ASTER NST/ATI with airborne magnetics related to delineating lineaments?**

This research was also aimed to determine the potential of ASTER NST and ATI to detect near-surface structures, and the benefit of their integration with airborne magnetics (1VD) to delineate structures. In particular, the 1VD and ATI methods could identify 77.14% and 40.32% respectively, and 17.49% was identified from both methods in common from the total integrated lineaments. This result shows the capability of ATI to detect lineaments is ***less*** as compared with airborne magnetics (1VD). However; the result inferred that ATI could be used as ***supplementary*** to magnetics (1VD), and ***integration*** of the results of the two methods has a benefit to delineate more structures than each of them does individually, and that shows its relevance to mineral exploration activities. In this research, other subsurface structures such as palaeochannels were inferred from ATI but could not be confirmed with airborne magnetics due to the limitation of magnetic data coverage and also possible lack of anomalous maghemite/magnetite alluvium. The ASTER NST could not detect structures as clear as ATI. This could be that ATI considers albedo and the temperature differences in the calculation which is more related to physical properties (density, thermal conductivity) than ASTER NST, and the effect of image acquisition time since the night-time imageries used in this study were not acquired at the optimum time.

3. **What effect does the green vegetation cover can have on the ability of ASTER NST imageries, acquired from different seasons, to discriminate outcrops from unconsolidated cover?**

The effect of green vegetation on discriminating outcrops from unconsolidated cover has not been published in detail previously and required to be done to determine the potential effect on ASTER NST. In particular, the analyses conducted by using ROI's from outcrops and unconsolidated cover showed that the green vegetation ***reduces and regulates*** the land surface temperature of the inferred outcrops and unconsolidated cover due to shading and evapotranspiration effects. These effects cause the heat that could be absorbed during the daytime both by the outcrops and unconsolidated cover to be ***lower***. This,

in the end, could result in ***reducing*** the emission in the night-time. As a result, the ***night-time surface temperature*** difference between the outcrops and unconsolidated cover becomes ***reduced and regulated***, and that causes discrimination to be difficult. This effect of green vegetation could be even higher if the vegetation of the study area at the time of image acquisition would be higher in an otherwise arid terrain.

7.2. Recommendations

1. Fieldwork to ***validate*** the results by collecting GPS coordinate data from outcrops and unconsolidated cover is recommended because that enables to understand the ***relationship*** between the thermal products and the physical nature of the surface materials and/or lithological units.

2. In this study, slope angle, ASTER NST and ATI ranges have been used to evaluate the potential of ASTER NST and ATI in discriminating outcrops from unconsolidated cover. However, the result could be improved if a ***regolith map*** would be produced from the combination of ***field and optical data*** (satellite VNIR-SWIR). Evaluating ASTER NST and ATI by using the resulting interpreted regolith map, as well as slope analysis, could improve the threshold for the extent of unconsolidated cover.

3. The night-time surface temperature imageries used in this study to analyze the ***effect of vegetation*** were limited because of the lack of thermal data availability. Further studies with greater night-time TIR acquisitions from different seasons would be useful to confirm the consistency of these results.

LIST OF REFERENCES

Adam, M. B., Babura, B. I., & Gopal, K. (2018). Range-Box Plotting Relating to Discrete Distribution. *MATEMATIKA*, *34*(2), 187–204. https://doi.org/10.11113/matematika.v34.n2.935

Agustin, F. (2017). ASTER Mineral Classification for Regolith Mapping in Tick Hill Mount Isa, Northwest Queensland. *Indonesian Journal on Geoscience*, *4*(2), 97–109. https://doi.org/10.17014/ijog.4.2.97-109

Alavipanah, S., Wegmann, M., Qureshi, S., Weng, Q., & Koellner, T. (2015). The Role of Vegetation in Mitigating Urban Land Surface Temperatures: A Case Study of Munich, Germany during the Warm Season. *Sustainability*, *7*(4), 4689–4706. https://doi.org/10.3390/su7044689

ASTER Surface Kinetic Temperature Product. (n.d.). Retrieved May 15, 2019, from https://asterweb.jpl.nasa.gov/content/03_data/01_Data_Products/release_surface_kinetic_temperatur.htm

Ayanlade, A. (2016). Seasonality in the daytime and night-time intensity of land surface temperature in a tropical city area. *Science of The Total Environment*, *557–558*, 415–424. https://doi.org/10.1016/J.SCITOTENV.2016.03.027

Babura, B. I., Adam, M. B., Rahim, A., Samad, A., Fitrianto, A., & Yusif, B. (2018). Analysis and Assessment of Boxplot Characters for Extreme Data. In *3rd International Conference on Mathematical Sciences and Statistics* (p. 12078). IOP Publishing. https://doi.org/10.1088/1742-6596/1132/1/012078

Beeson, P. C., Miller, D. A., & Duffy, C. J. (2011). Identifying ephemeral and perennial stream reaches using apparent thermal inertia of an ungauged basin in central New Mexico. *Geocarto International*, *26*(3), 183–194. https://doi.org/10.1080/10106049.2011.553290

British Geological Survey. (2019). Retrieved January 19, 2019, from http://www.geomag.bgs.ac.uk/data_service/models_compass/wmm_calc.html

Connelly, D., Walker, P. W. ., & Richards, D. S. (2018). *Haib Copper Project 2018 Preliminary Economic Assessment*. Vancouver. Retrieved from https://www.deepsouthresources.com/wp-content/uploads/Haib_Copper_Project_2018_Preliminary_Economic_Assessment.pdf

Cornell, D. H., Thomas, R. J., Moen, H. F. G., Reid, D. L., Moore, J. M., & Gibson, R. L. (2006). The Namaqua-Natal Province. *Geological Society of South Africa*, 235–379. Retrieved from https://www.researchgate.net/publication/260184837

Cudahy, T. (2012). *Satellite ASTER Geoscience Product Notes for Australia*. Retrieved from http://c3dmm.csiro.au/Australia_ASTER/Australian ASTER Geoscience Product Notes FINALx.pdf

Dentith, M., & Mudge, S. (2014). *Geophysics for the mineral exploration geoscientist. AusIMM Bulletin* (1st ed.). New York: Cambridge University Press. https://doi.org/10.1007/s00126-014-0557-9

Eberle D, Andritzky G, & Wackerle R. (1995). *The new magnetic data set of Namibia: Its contributions to the understanding of crustal evolution and regional distribution of mineralization*. Windhoek. Retrieved from http://www.mme.gov.na/files/publications/4e9_Eberle Andritzky and Wackerle_new magnetic data set.pdf

Eglington, B. M., & Armstrong, R. A. (2003). Geochronological and isotopic constraints on the Mesoproterozoic Namaqua–Natal Belt: evidence from deep borehole intersections in South Africa. *Precambrian Research*, *125*(3–4), 179–189. https://doi.org/10.1016/S0301-9268(02)00199-7

El-Magd, I. A., Mohy, H., & Basta, F. (2015). Application of remote sensing for gold exploration in the Fawakhir area, Central Eastern Desert of Egypt. *Arabian Journal of Geosciences*, *8*(6), 3523–3536. https://doi.org/10.1007/s12517-014-1429-4

Fatemi, M., & Narangifard, M. (2019). Monitoring LULC changes and its impact on the LST and NDVI in District 1 of Shiraz City. *Arabian Journal of Geosciences*, *12*(4), 1–12. https://doi.org/10.1007/s12517-019-4259-6

Geomorphology of slopes. (n.d.). Retrieved April 14, 2019, from http://w3.salemstate.edu/~lhanson/gls210/gls210_slopes.htm

Geoscience Australia. (2014). Retrieved January 20, 2019, from http://www.ga.gov.au/scientific-topics/disciplines/geophysics/radiometrics

Goudie, A., & Viles, H. A. (2015). *Landscapes and landforms of Namibia* (1st ed.). New York London: Springer Dordrecht Heidelberg. https://doi.org/10.1007/978-94-017-8020-9

Gupta, R. P. (2003). *Remote Sensing Geology* (2nd ed.). Verlag Berlin Heidelberg: Springer Berlin Heidelberg. https://doi.org/10.1007/978-3-662-05283-9

Hewson, R. D., Cudahy, T. J., Drake-Brockman, J., Meyers, J., & Hashemi, A. (2006). Mapping geology associated with manganese mineralisation using spectral sensing techniques at Woodie Woodie, East Pilbara. *Exploration Geophysics*, *37*(4), 389–400. https://doi.org/10.1071/EG06389

Hewson, R., & Robson, D. (2014). *Using ASTER and geophysical mapping for mineral exploration in the Wagga Wagga and Cobar areas, N.S.W. Quarterly Notes, Geological Survey of New South Wales*. Retrieved from https://www.resourcesandenergy.nsw.gov.au/__data/assets/pdf_file/0003/522165/QN140.pdf

Hewson, R., Robson, D., Carlton, A., & Gilmore, P. (2017). Geological application of ASTER remote sensing within sparsely outcropping terrain, Central New South Wales, Australia. *Cogent Geoscience*, *3*(1), 1–22. https://doi.org/10.1080/23312041.2017.1319259

Hung, L. Q., Batelaan, O., & De Smedt, F. (2005). Lineament extraction and analysis, comparison of LANDSAT ETM and ASTER imagery. Case study: Suoimuoi tropical karst catchment, Vietnam. In *SPIE* (Vol. 5983, pp. 1–12). https://doi.org/10.1117/12.627699

Kahle, A. B. (1987). Surface emittance, temperature, and thermal inertia derived from Thermal Infrared Multispectral Scanner (TIMS) data for Death Valley, California. *Geophysics*, *52*(7), 858–874. https://doi.org/10.1190/1.1442357

Kahle, A. B., Madura, D. P., & Soha, J. M. (1980). Middle infrared multispectral aircraft scanner data: analysis for geological applications. *Applied Optics*, *19*(14), 2279–2290. https://doi.org/10.1364/AO.19.002279

Kalinowski, A., & Oliver, S. (2004). *ASTER Processing Manual*. Retrieved from https://d28rz98at9flks.cloudfront.net/67957/67957.pdf

Kawashima, S. (1994). Relation between vegetation, surface temperature, and surface composition in the tokyo region during winter. *Remote Sensing of Environment*, *50*(1), 52–60. https://doi.org/10.1016/0034-4257(94)90094-9

Kirkpatrick, L. H., & Green, A. N. (2018). Antecedent geologic control on nearshore morphological development: The wave dominated, high sediment supply shoreface of southern Namibia. *Marine Geology*, *403*, 34–47. https://doi.org/10.1016/J.MARGEO.2018.05.003

Kruse, F. A., Lefkoff, A. B., Boardman, J. W., Heidebrecht, K. B., Shapiro, A. T., Barloon, P. J., & Goetz, A. F. H. (1993). The spectral image processing system (SIPS)—interactive visualization and analysis of imaging spectrometer data. *Remote Sensing of Environment*, *44*(2–3), 145–163. https://doi.org/10.1016/0034-4257(93)90013-N

Kuenzer, C., & Dech, S. W. (2013). *Thermal infrared remote sensing : sensors, methods, applications*. (C. Kuenzer & S. W. Dech, Eds.) (1st ed.). New York, London: Springer Verlag. https://doi.org/10.1007/978-94-007-6639-6

Landau, S., & Everitt, B. S. (2004). *A Handbook of Statistical Analyses using SPSS* (1st editio). London: Chapman & Hall/CRC Press LLC. Retrieved from www.crcpress.com

Lech, M., & De Caritat, P. (2007). *PROTOCOL FOR SAMPLING IN REGIONAL GEOCHEMICAL SURVEYS: LESSONS FROM PILOT PROJECTS*. Bentley. Retrieved from http://crcleme.org.au

Lillesand, T. M., Kiefer, R. W., & Chipman, J. W. (2015). *Remote sensing and image interpretation* (7th ed.). New York: John Wiley & Sons, Inc. Retrieved from https://www.wiley.com/en-us/Remote+Sensing+and+Image+Interpretation%2C+7th+Edition-p-9781118343289

Liu, Z., Ballantyne, A. P., & Cooper, L. A. (2019). Biophysical feedback of global forest fires on surface temperature. *Nature Communications*, *10*(1), 1–9. https://doi.org/10.1038/s41467-018-08237-z

Macey, P. H., Thomas, R. J., Minnaar, H. M., Gresse, P. G., Lambert, C. W., Groenewald, C. A., … Tinguely, C. (2017). Origin and evolution of the ~1.9 Ga Richtersveld Magmatic Arc, SW Africa. *Precambrian Research*, *292*, 417–451. https://doi.org/10.1016/j.precamres.2017.01.013

Mackey, T., Lawrie, K., Wilkes, P., Munday, T., Kovacs, N. de S., Chan, R., … Evans, R. (2000a). Palaeochannels near west wyalong, new south wales: A case study in delineation and modelling using aeromagnetics. *Exploration Geophysics*, *31*(2), 1–7. https://doi.org/10.1071/EG00001

Mackey, T., Lawrie, K., Wilkes, P., Munday, T., Kovacs, N. de S., Chan, R., … Evans, R. (2000b). Palaeochannels near West Wyalong, New South Wales: A case study in delineation and modelling using aeromagnetics. *Exploration Geophysics*, *31*(1–2), 1–7. https://doi.org/10.1071/EG00001

Majumdar, T. J. (2003). Regional thermal inertia mapping over the Indian subcontinent using INSAT-1D VHRR data and its possible geological applications. *International Journal of Remote Sensing*, *24*(11), 2207–2220. https://doi.org/10.1080/01431160210161724

Mathew, A., Khandelwal, S., & Kaul, N. (2018). Spatio-temporal variations of surface temperatures of Ahmedabad city and its relationship with vegetation and urbanization parameters as indicators of surface temperatures. *Remote Sensing Applications: Society and Environment*, *11*, 119–139.

https://doi.org/10.1016/J.RSASE.2018.05.003
Mitra, D. S., & Majumdar, T. J. (2010). Thermal inertia mapping over the Brahmaputra basin, India using NOAA-AVHRR data and its possible geological applications. *International Journal of Remote Sensing*, *25*(16), 3245–3260. https://doi.org/10.1080/01431160310001632701
Mokhtari, M. H., Busu, I., Mokhtari, H., Zahedi, G., Sheikhattar, L., & Movahed, M. A. (2013). Neural network and multiple linear regression for estimating surface albedo from ASTER visible and near-infrared spectral bands. *Earth Interactions*, *17*(3), 1–20. https://doi.org/10.1175/2011EI000424.1
Nasipuri, P., Mitra, D. S., & Majumdar, T. J. (2005). Generation of thermal inertia image over a part of Gujarat: A new tool for geological mapping. *International Journal of Applied Earth Observation and Geoinformation*, *7*(2), 129–139. https://doi.org/10.1016/j.jag.2005.02.002
Nuzzo, R. L. (2016). The Box Plots Alternative for Visualizing Quantitative Data. *PM and R*, *8*(3), 268–272. https://doi.org/10.1016/j.pmrj.2016.02.001
Oha, I. A., Onuoha, K. M., Nwegbu, A. N., & Abba, A. U. (2016). Interpretation of high resolution aeromagnetic data over southern benue trough, Southeastern Nigeria. *Journal of Earth System Science*, *125*(2), 369–385. https://doi.org/10.1007/s12040-016-0666-1
Papadaki, E., Mertikas, S., & Sarris, A. (2011). Identification of Lineaments With Possible Structural Origin Using Aster Images And DEM Derived Products in Westerm Crete , Greece. In *EARSeL eProceedings* (Vol. 10, pp. 9–26).
Pargal, S., Agarwal, S., Gupta, P. K., & Van Der Werff, H. M. A. (2011). Spatial-spectral endmember extraction for spaceborne hyperspectral data. In *ICIIP 2011 - Proceedings: 2011 International Conference on Image Information Processing*. https://doi.org/10.1109/ICIIP.2011.6108927
Pratt, D. A., & Ellyett, C. D. (1979). The thermal inertia approach to mapping of soil moisture and geology. *Remote Sensing of Environment*, *8*(2), 151–168. https://doi.org/10.1016/0034-4257(79)90014-2
Price, J. C. (1977). Thermal Inertia Mapping: A New View of the Earth. *Journal of Geophysical Research*, *82*(18), 2582–2590. https://doi.org/http://dx.doi.org/10.1029/JC082i018p02582; doi:10.
Ramakrishnan, D., Bharti, R., Singh, K. D., & Nithya, M. (2013). Thermal inertia mapping and its application in mineral exploration: Results from mamandur polymetal prospect, India. *Geophysical Journal International*, *195*(1), 357–368. https://doi.org/10.1093/gji/ggt237
Rani, M., Kumar, P., Pandey, P. C., Srivastava, P. K., Chaudhary, B. S., Tomar, V., & Mandal, V. P. (2018). Multi-temporal NDVI and surface temperature analysis for Urban Heat Island inbuilt surrounding of sub-humid region: A case study of two geographical regions. *Remote Sensing Applications: Society and Environment*, *10*(March), 163–172. https://doi.org/10.1016/j.rsase.2018.03.007
Reid, D. L. (1977). *GEOCHEMISTRY OF PRECAMBRIAN IGNEOUS ROCKS IN THE LOWER ORANGE RIVER REGION (PhD thesis)*. University of Cape Town. Retrieved from https://open.uct.ac.za/bitstream/handle/11427/23362/thesis_sci_Reid_1977.pdf?sequence=1
Saada, S. A. (2016). Edge detection and depth estimation of Galala El Bahariya Plateau, Eastern Desert-Egypt, from aeromagnetic data. *Geomechanics and Geophysics for Geo-Energy and Geo-Resources*, *2*(1), 25–41. https://doi.org/10.1007/s40948-015-0019-6
Song, Z., Li, R., Qiu, R., Liu, S., Tan, C., Li, Q., … Ma, M. (2018). Global land surface temperature influenced by vegetation cover and PM2.5 from 2001 to 2016. *Remote Sensing*, *10*(12), 1–18. https://doi.org/10.3390/rs10122034
Swart, R. (2008). *An earth science review of the Orange-Fish River Basin, Namibia*. Windhoek. Retrieved from www.drfn.org.na/erb/index.html
T. Cocks, R. Jenssen, A. Stewart, I. W. and T. S. (1998). The HyMap. In *October* (pp. 1–6). Zurich. Retrieved from http://www.hyvista.com/wp_11/wp-content/uploads/2011/02/EARSEL98_HyMap.pdf
Taha, H., Akbari, H., & Rosenfeld, A. (1989). *Vegetation Canopy Micro-Climate: A Field-Project in Davis, California*. California. Retrieved from https://escholarship.org/uc/item/7td0c626
Thakur, S., Chudasama, B., Porwal, A., & González-Álvarez, I. (2016). Sub-surface paleochannel detection in DeGrussa area, Western Australia, using thermal infrared remote sensing. In *Proc. of SPIE* (Vol. 9877, pp. 1–13). New Delhi: SPIE Asia-Pacific Remote Sensing. https://doi.org/10.1117/12.2223626
The Density of Common Rocks and Minerals. (n.d.). Retrieved April 18, 2019, from https://www.thoughtco.com/densities-of-common-rocks-and-minerals-1439119
Thomas, R. J., Agenbacht, A. L. D., Cornell, D. H., & Moore, J. M. (1994). The Kibaran of southern Africa: Tectonic evolution and metallogeny. *Ore Geology Reviews*, *9*(2), 131–160. https://doi.org/10.1016/0169-1368(94)90025-6

Ulusoy, İ. (2016). Temporal radiative heat flux estimation and alteration mapping of Tendürek volcano (eastern Turkey) using ASTER imagery. *Journal of Volcanology and Geothermal Research*, *327*, 40–54. https://doi.org/10.1016/j.jvolgeores.2016.06.027

Ulusoy, I., Labazuy, P., & Aydar, E. (2012). STcorr: An IDL code for image based normalization of lapse rate and illumination effects on nighttime TIR imagery. *Computers and Geosciences*, *43*, 63–72. https://doi.org/10.1016/j.cageo.2012.02.012

van der Meer, F. D., van der Werff, H. M. A., van Ruitenbeek, F. J. A., Hecker, C. A., Bakker, W. H., Noomen, M. F., … Woldai, T. (2012). Multi- and hyperspectral geologic remote sensing: A review. *International Journal of Applied Earth Observation and Geoinformation*, *14*(1), 112–128. https://doi.org/10.1016/j.jag.2011.08.002

Van Ruitenbeek, F. J. A., Bakker, W. H., Van Der Werff, H. M. A., Zegers, T. E., Oosthoek, J. H. P., Omer, Z. A., … Van Der Meer, F. D. (2014). Mapping the wavelength position of deepest absorption features to explore mineral diversity in hyperspectral images. *Planetary and Space Science*, *101*, 108–117. https://doi.org/10.1016/j.pss.2014.06.009

Visual Information Solutions, I. (2009). *ENVI User's Guide*. Retrieved from www.apache.org/

Walker, W. . (2018). *The Haib Copper Porphyry Project, Namibia*. Cape Town. Retrieved from https://www.deepsouthresources.com/wp-content/uploads/Haib_NI43-101_May-3-2016_FINAL.pdf

Watson, K. (1975). Geologic Applications of Thermal Infrared Images. In *IEEE* (Vol. 9, pp. 128–137). Denver: U.S. Geological Survey. https://doi.org/10.1109/PROC.1975.9712

WorldView-3 Satellite Sensor. (n.d.). Retrieved April 7, 2019, from https://www.satimagingcorp.com/satellite-sensors/worldview-3/

Xue, Y., & Cracknell, A. P. (1995). Advanced thermal inertia modelling. *International Journal of Remote Sensing*, *16*(3), 431–446. https://doi.org/10.1080/01431169508954411

Zadeh, M. H., & Tangestani, M. H. (2013). Comparison of ASTER thermal data sets in lithological mapping at a volcano-sedimentary basin: a case study from southeastern Iran. *International Journal of Remote Sensing*, *34*(23), 8393–8407. https://doi.org/10.1080/01431161.2013.838709

Zou, Z., Yang, Y., & Qiu, G. (2019). Quantifying the Evapotranspiration Rate and Its Cooling Effects of Urban Hedges Based on Three-Temperature Model and Infrared Remote Sensing. *Remote Sensing*, *11*(2), 1–18. https://doi.org/10.3390/rs11020202

Zuo, R., Xiong, Y., Wang, J., & Carranza, E. J. M. (2019). Deep learning and its application in geochemical mapping. *Earth-Science Reviews*, *192*, 1–14. https://doi.org/10.1016/j.earscirev.2019.02.023

APPENDICES

Appendix 1: Overlaying the lithological unit vectors of the classified geological map and the slope map to select slope angle ranges (thresholds) that can represent the unconsolidated cover. The unconsolidated cover unit of the geological map of Haib (a), the classified slope map derived from DEM (b).

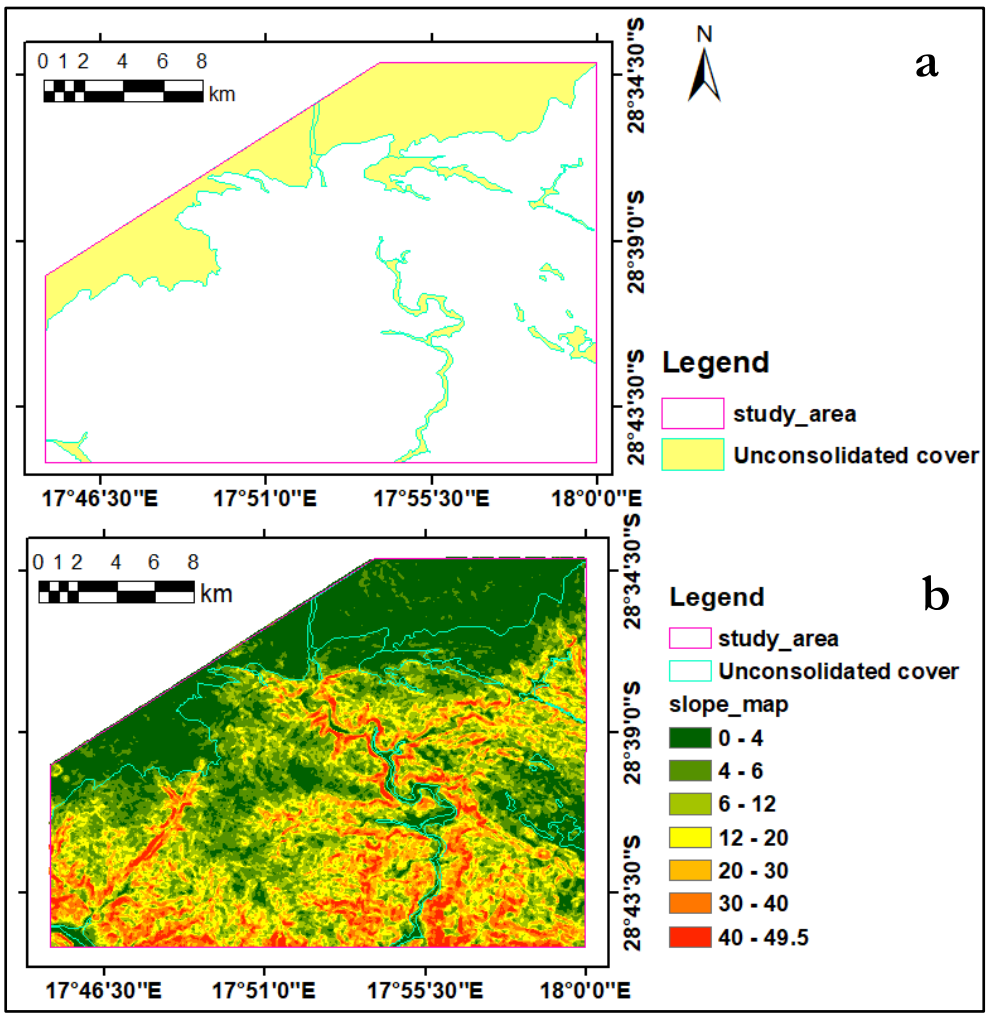

Appendix 2 Overlaying the lithological unit vectors of the classified geological map and the slope map to select slope angle ranges (thresholds) that can represent the outcrops. The outcropping unit of the geological map of Haib (a), the classified slope map derived from DEM (b).

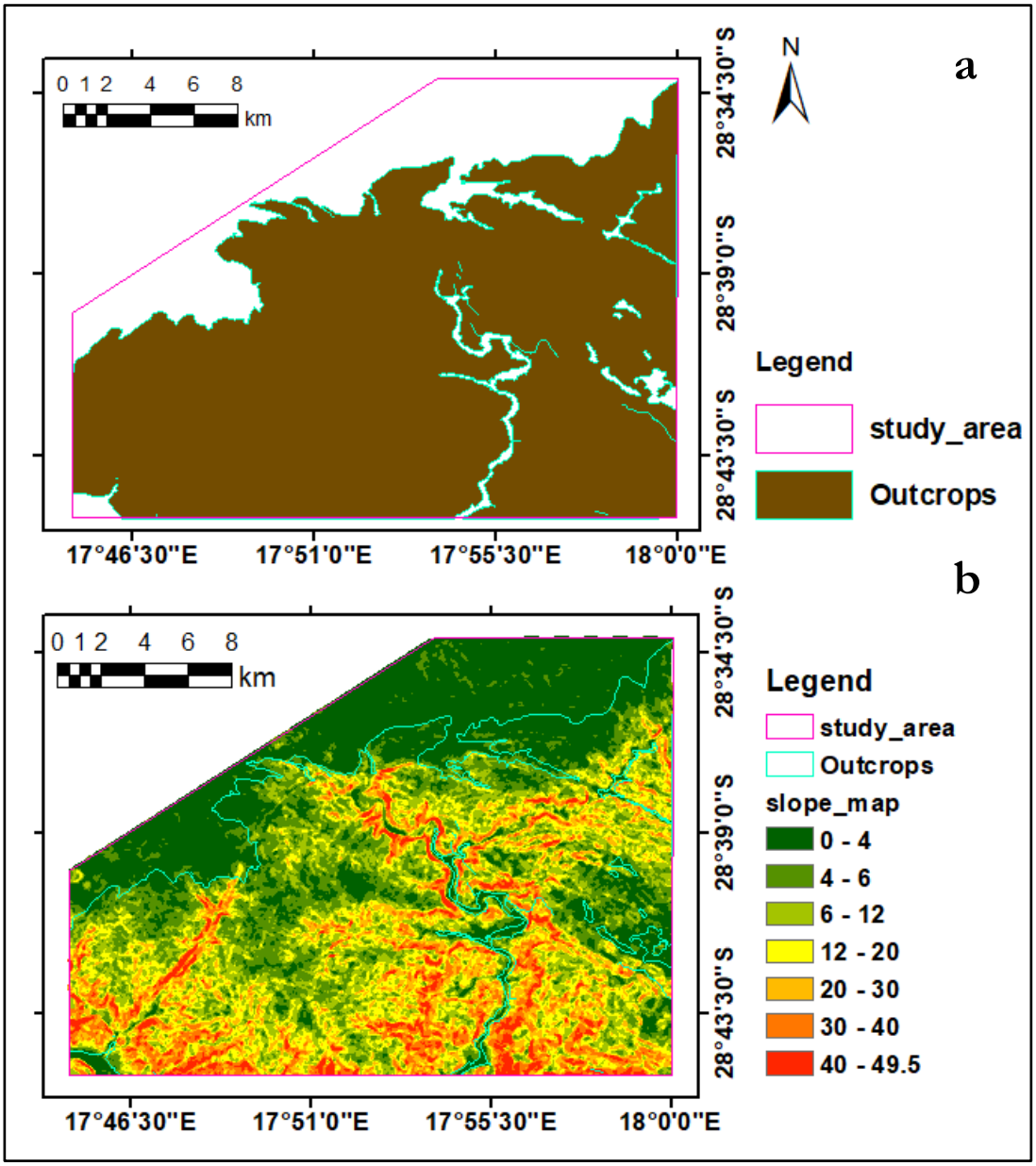

Appendix 3: Overlaying the lithological unit vectors of the classified geological map on ASTER NST product to select the ranges of values (thresholds) that can represent the unconsolidated cover and outcrops. The unconsolidated cover & outcrop units of the classified geological map of Haib (a); ASTER NST product (b); ASTER NST_range_1 (8.9 -11.6℃) (c); ASTER NST_range_2 (11.6-15.9 ℃) (d)

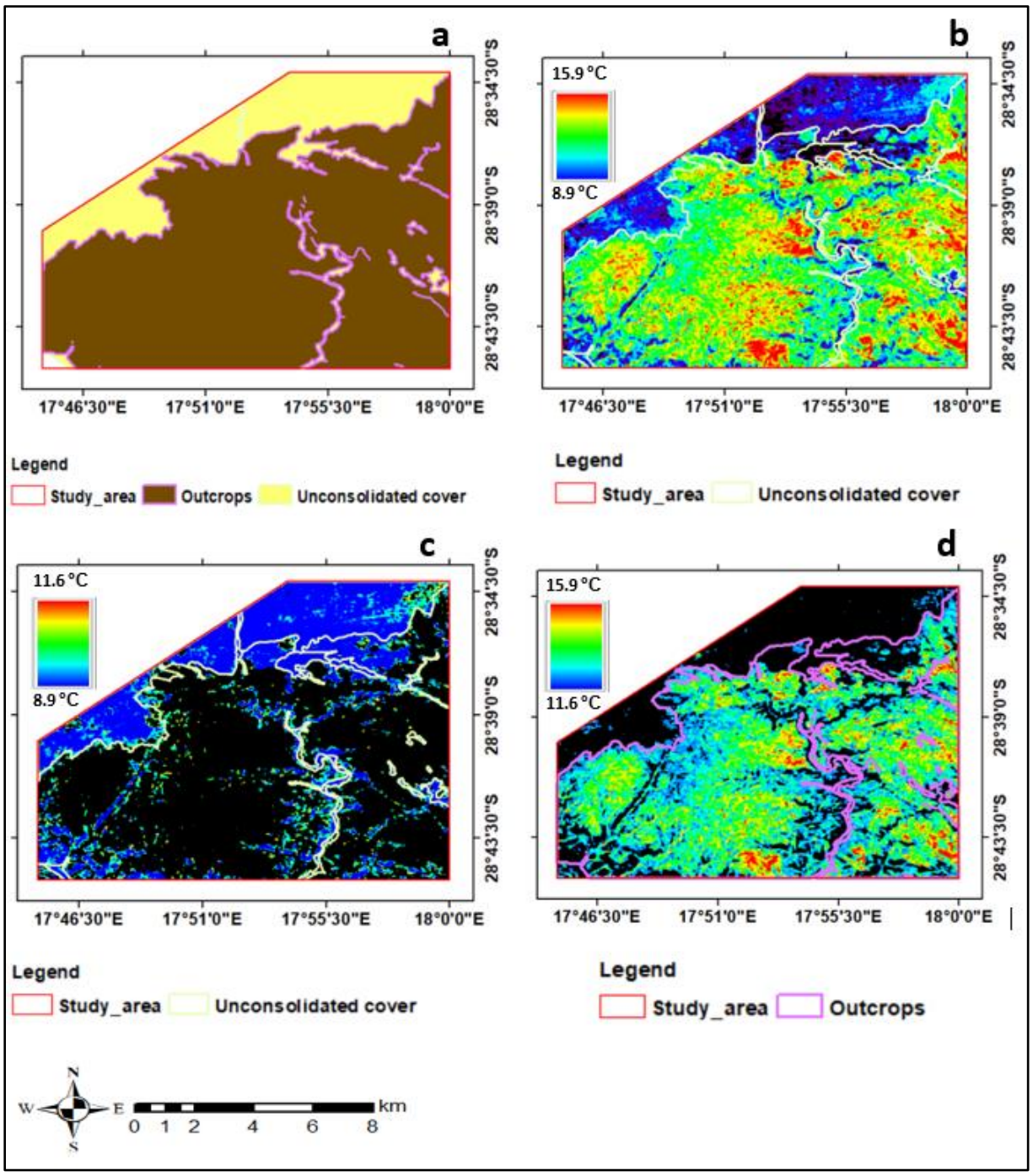

Appendix 4: Overlaying the lithological unit vectors of the classified geological map on ATI product to select the range of values (thresholds) that can represent the unconsolidated cover and outcrops. The unconsolidated & outcrop units of the classified geological map of Haib (a); ATI product (b); ATI_range_1 (0.073-0.022°C-1) (c); ATI_range_2 (0.022-0.061°C-1) (d)

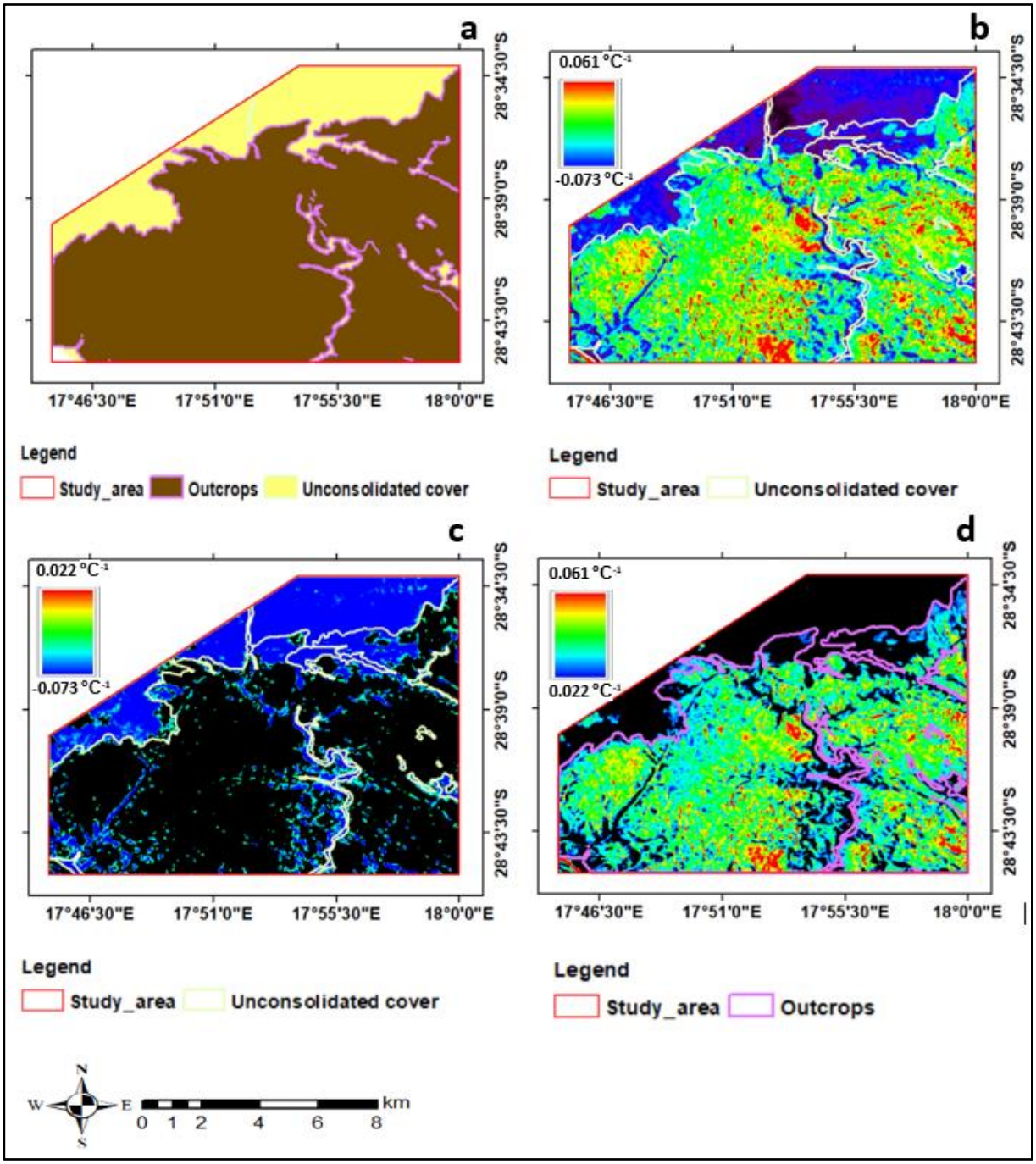

Appendix 5: The slope angle ranges (0-4^0 and 4^0-6^0) overlain with WV-3 (Panchromatic) data to evaluate the slope angle ranges how well it can be used as a representative of the unconsolidated cover and outcrops

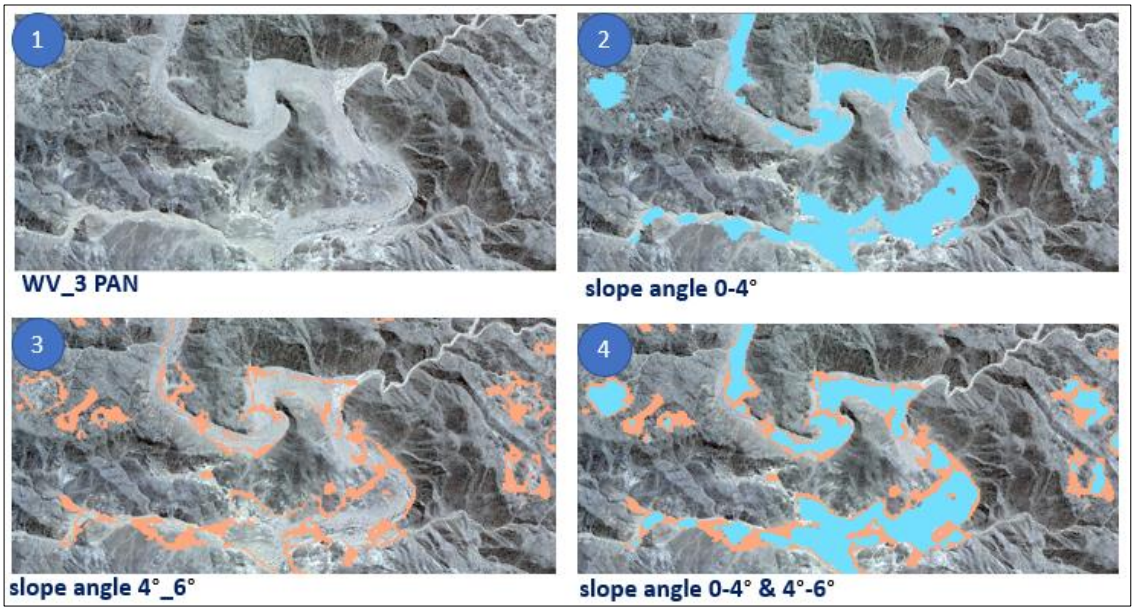

Appendix 6: Slope angle ranges **0-4° (yellow), 4°- 6° (orange) & >6°(red)** overlain with google earth to evaluate the slope angle ranges how well it can be used as a representative of the unconsolidated cover and outcrops

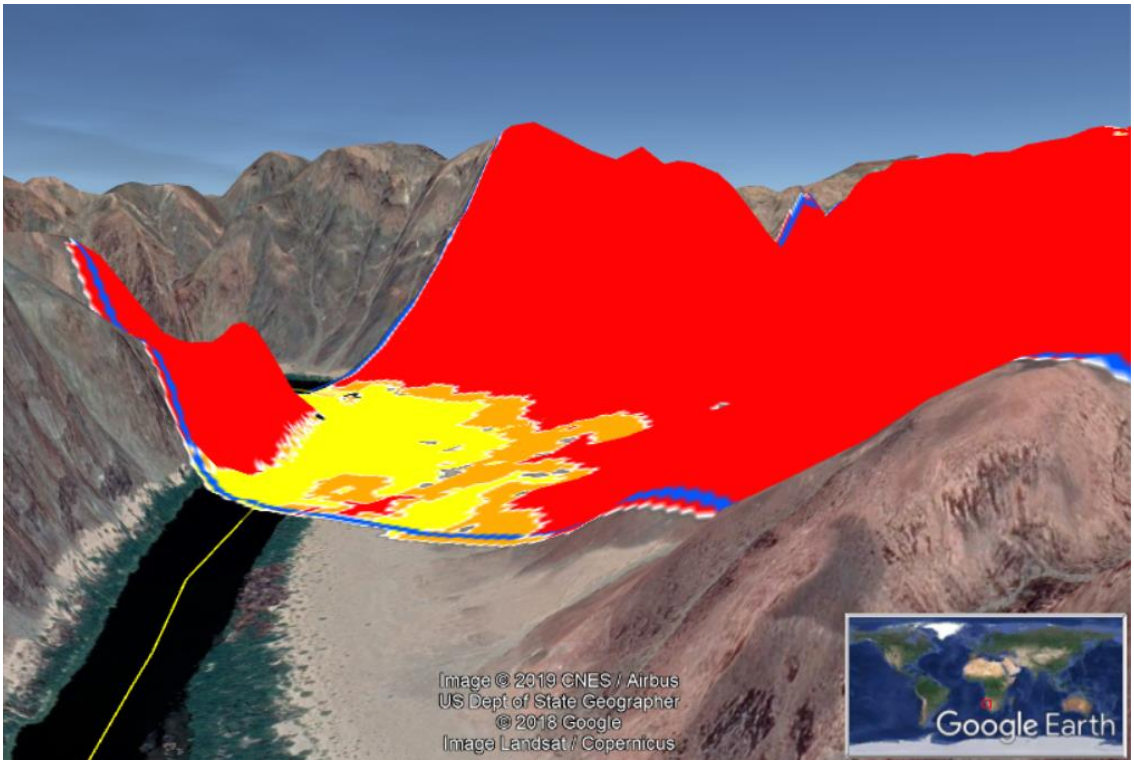

Appendix 7: Sand dunes identified from ATI product and confirmed with WV-3 (Panchromatic)

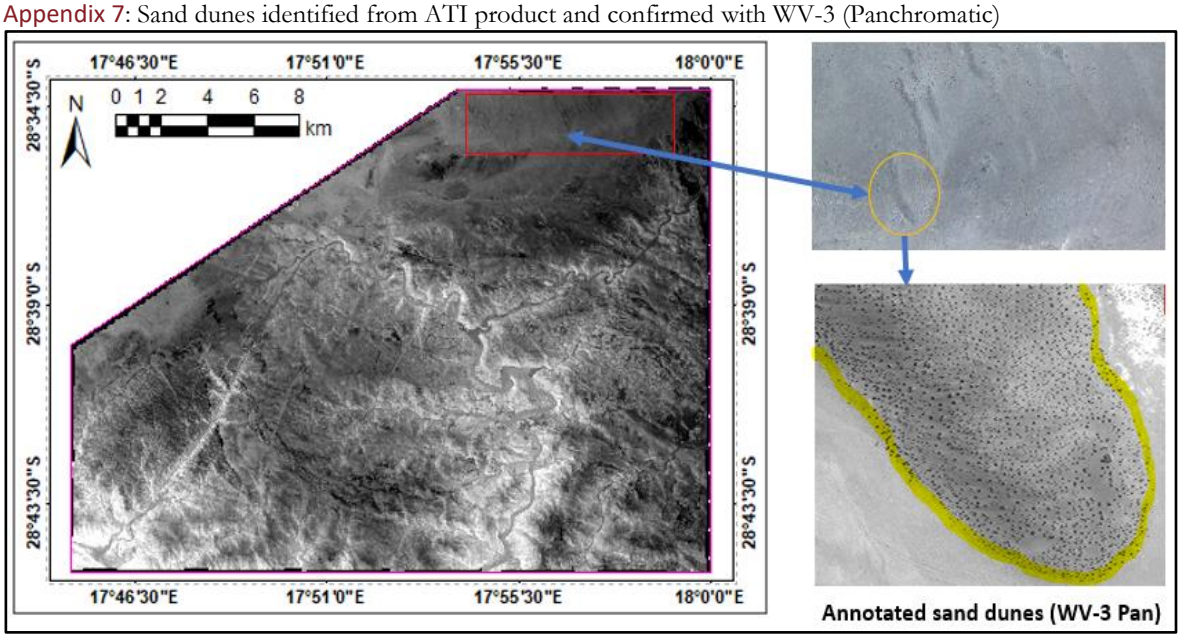

Appendix 8: Comparison of the Emissivity spectra of quartz from JHU (white) with the sample spectra (red) to confirm sand dunes

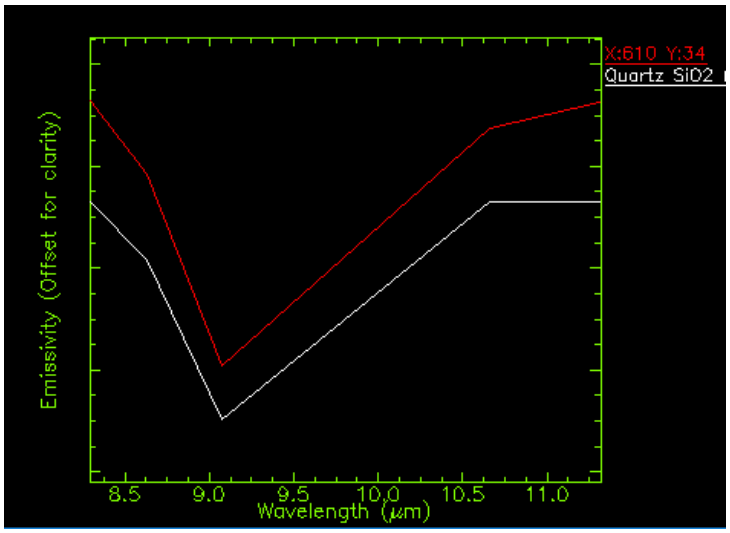

Appendix 9: The Zonal statistics result of Thorium grid from radiometrics

S.No	LITHO_UNIT	MIN	MAX	RANGE	MEAN	STD
1	Hornblendite diorite	5.221726	20.460236	15.23851	11.800893	2.562181
2	Upper feldspar porphyry.	9.438536	28.087729	18.649193	16.423004	2.79884
3	Granodiorite	3.604606	37.19416	33.589554	18.364145	3.733022
4	Alluvial sediments	3.383948	35.027542	31.643595	18.841028	4.633832
5	Porphyritic granite	11.450494	35.694702	24.244208	20.829802	3.124075
6	Amphibolite	6.649146	36.274704	29.625558	21.15547	4.305897

7	Karoo sediment	22.512527	22.512527	0	22.512527	0
8	Porphyritic adamellite	15.19525	30.238174	15.042925	22.909795	2.294646
9	Lower feldspar porphyry	7.407299	40.093437	32.686139	23.527193	3.682721
10	Undifferentiated granitoid	6.29669	54.857441	48.560751	25.282503	9.622665
11	Leucogranite	5.961768	62.669559	56.707792	35.095751	11.462446

Appendix 10: The Zonal statistics result of Potassium grid from radiometrics

S.No	LITHO_UNIT	MIN	MAX	RANGE	MEAN	STD
1	Hornblendite diorite	0.988642	3.642341	2.653699	1.824698	0.404569
2	Upper feldspar porphyry.	0.422729	6.059875	5.637146	2.811954	0.697236
3	Granodiorite	2.838444	2.838444	0	2.838444	0
4	Alluvial sediments	1.675663	4.466014	2.790352	2.895207	0.507238
5	Porphyritic granite	1.147958	7.605494	6.457536	3.248548	0.601765
6	Amphibolite	0.646553	7.590252	6.9437	3.383371	0.996919
7	Karoo sediment	-0.462013	5.984241	6.446254	3.406034	0.6855
8	Porphyritic adamellite	0.666324	6.459004	5.792681	3.491748	0.583961
9	Lower feldspar porphyry	1.523955	5.785112	4.261157	3.844653	0.529814
10	Undifferentiated granitoid	0.859227	6.511856	5.652629	3.919441	0.94302
11	Leucogranite	2.74983	4.924106	2.174276	3.983722	0.321891

Appendix 11: The Zonal statistics result of Potassium grid from radiometrics

S.No	LITHO_UNIT	MIN	MAX	RANGE	MEAN	STD
1	Hornblendite diorite	-1.82416	18.9342	20.75836	6.896086	4.143125
2	Upper feldspar porphyry.	1.364364	12.83231	11.46794	7.104434	2.118495
3	Granodiorite	-1.77565	31.39215	33.16781	10.19711	4.274058
4	Alluvial sediments	10.35168	10.35168	0	10.35168	0
5	Porphyritic granite	3.344341	22.6662	19.32185	10.39434	3.172547
6	Amphibolite	1.095857	35.72877	34.63291	11.01073	4.014782
7	Karoo sediment	5.802168	18.91683	13.11466	11.37143	2.647271
8	Porphyritic adamellite	1.321689	46.8372	45.51551	11.37774	6.040274
9	Lower feldspar porphyry	3.475699	30.45604	26.98034	13.52245	4.571172

10	Undifferentiated granitoid	3.563055	44.47243	40.90937	15.08083	5.587575
11	Leucogranite	6.601372	47.19582	40.59445	18.683	5.218944

Appendix 12: The rainfall data of the whole 2003, 2015 and 2018 years used to estimate the vegetated period

STN---	WBAN	YEARMODA	PRCP (inch)	PRCP (mm/day)
684110	99999	20030430	0.54	13.716
684110	99999	20030813	0.05	1.27
684110	99999	20030814	0.04	1.016
684110	99999	20030817	4.13	104.902
684110	99999	20030819	0.02	0.508
684110	99999	20030820	0.06	1.524
684110	99999	20030824	0.04	1.016
684110	99999	20030825	0.04	1.016
684110	99999	20031013	0.01	0.254
684110	99999	20031016	0.01	0.254
684110	99999	20031030	0.02	0.508
684110	99999	20031031	0.03	0.762
684110	99999	20180329	0.71	18.034
684110	99999	20180330	0.16	4.064
684110	99999	20180404	0.02	0.508
684110	99999	20180417	0.31	7.874
684110	99999	20180519	0.08	2.032
684110	99999	20180615	0.02	0.508
684110	99999	20180702	0.03	0.762
684110	99999	20150627	0.04	1.016
684110	99999	20150724	0.01	0.254
684110	99999	20150830	0.01	0.254

Appendix 13: Ternary map generated from radiometrics grids of K, Th & U

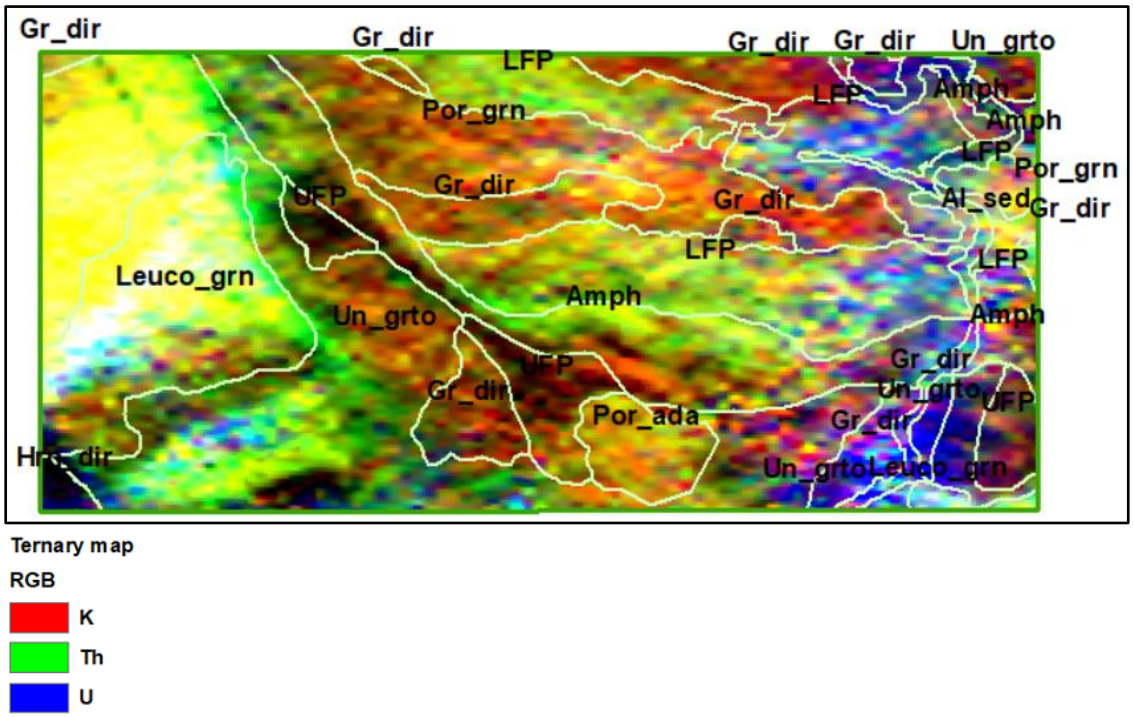

Appendix 14: Density of common rocks ("The Density of Common Rocks and Minerals," n.d.)

Rock	Density (g/cm³)
Andesite	2.5 - 2.8
Diorite	2.8 - 3.0
Granite	2.6 - 2.7
Sandstone	2.2 - 2.8
amphibolite	2.79–3.14
Hornblendite	2.66-2.75
sand	1.60-1.80
clay	1.10-1.47

Appendix 15: The calculation procedures flow chart for altitude, aspect and slope correction (after Ulusoy et al., 2012)

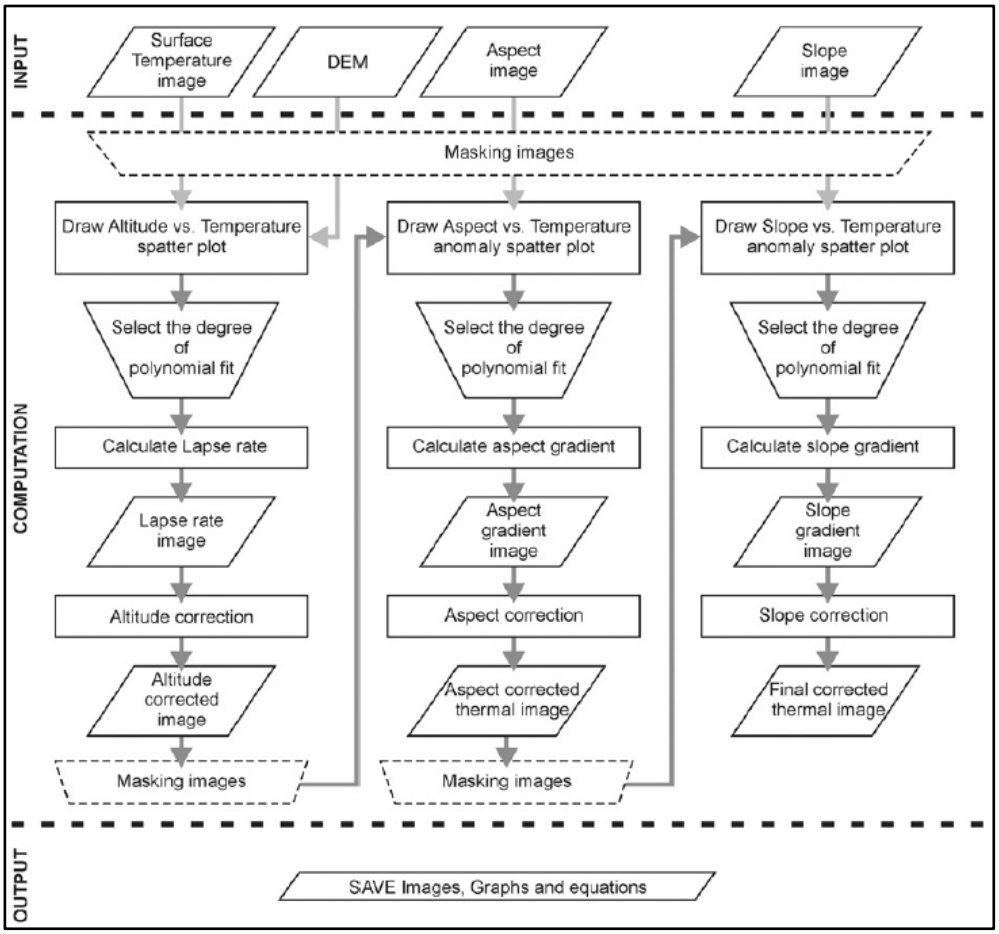

Appendix 16: Minerals identified from HyMap data and used to check the ASTER mineral products

No.	Minerals
1	Actinolite
2	Epidote
3	Muscovite
4	Chlorite
5	Alunite
6	Illite
7	Montmorillonite
8	Pyrophyllite

Appendix 17: thermally anomalous spots observed from the derived ATI products and estimated to be shallow depth buried bedrocks